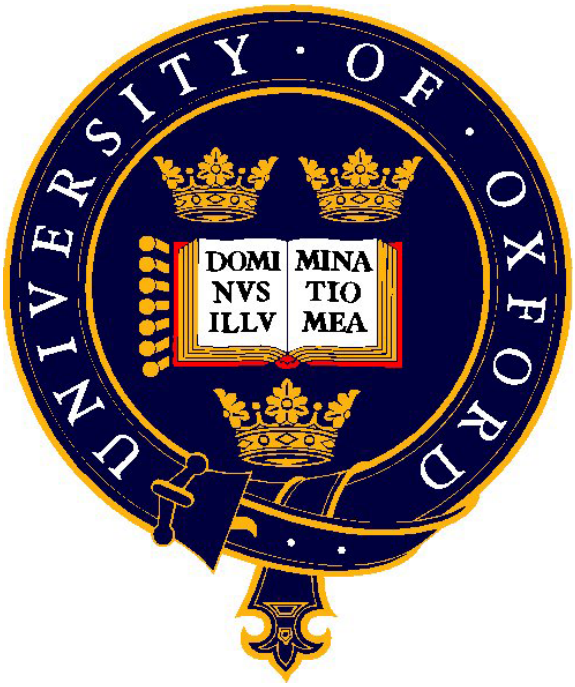

Spectroscopy of single colour centres in ultra-pure synthetic diamonds

A thesis submitted for the degree of Doctor of Philosophy
in the University of Oxford

Trinity Term 2010

Fabio Grazioso, Mansfield college, Oxford
supervised by Dr. Jason Smith and Dr. Pieter Kok, Department of Materials

Contents

Chapter 1

Introduction

1.1 Defect centres in crystals

The present work is centred around a specific *defect centre* or *colour centre*, in the diamond crystal, specifically the *nitrogen - vacancy (NV) centre*. A defect centre, sometimes also called *F-centre* from the german word Farbe (colour), is in general an anomaly in the evenly spaced crystal lattice of a solid. Such a defect can interact with electromagnetic radiation with narrow spectral lines (and wider bands), either in absorption and photoluminescence (PL) emission, giving to a transparent crystal a colour. In many respects it is possible to consider such a system as a localised quantum system, that stands out from the surrounding crystal. This means that a defect centre has both the characteristics of a single isolated quantum system together with the stability, ease of manipulation and interaction of a macroscopic solid state object. Early work on colour centres can be found e.g. in [Her57, KH66], [Hir90], and examples of more recent work is found in [Ber98, BAC+10]. In

this introduction we are going to point out the principal characteristics of the defect centres in general, and then of the NV centre in particular, which make it so promising for several applications, and motivate the work of an ever enlarging community of scientists around the world.

1.2 Accessing a quantum observable

A goal of this scientific community is to be able to detect and manipulate the *state* of a *quantum system*, being able to measure and change one or more *observables*, i.e. physical parameters of the system which behave according to the postulates of quantum mechanics, and which are possible to *observe* (measure). As said, a defect centre in a solid is an ideal subject to attempt such measurements and manipulations, and the observable of choice which has been devised for this purpose is the *electronic spin state*. Some electrons have wave functions localised on the defect, and act as in molecular orbitals, so it is possible to develop theoretical models which describe their energy levels, spin sublevels, and fine structure, and apply several experimental techniques to measure and manipulate such electronic states. The experimental techniques developed in this field are several, each with its strong and weak aspects. The electron paramagnetic resonance (EPR) is a technique developed as early as 1945 [ZAV46, Ble51, BI51] and has been applied to the NV centre in the exhaustive, but dated work by Loubser [LvW78]. In more recent years, many works on EPR studies of the NV centre in diamond and other centres have been published, among which we can cite [HMF93a, HMF93b, JSLP93, Dav94, BN95, GDT+97, WNB01, BIS+09]. As

findings of these works, we can mention the fact that the electronic ground state of the centre is paramagnetic, is a spin triplet with a separation between a singlet and a degenerate doublet spin sublevels of the order of GHz (zero field splitting), and that the spin is (partially) preserved during excitation-emission-relaxation cycles between the ground state and a specific excited state. Other characteristics are a large optical absorption cross-section, and high quantum efficiency for the photoluminescence process.

Another technique, which can be used to determine the energy of hyperfine transitions within an atom or molecule, and which has been applied to defect centres, is the *saturated spectroscopy*, also known as *hole burning* [Ben62]. Works using this technique[HHM84, RMK87, OPS96] have shown data which have contributed to correct some initial mistakes, ([dP65, LvW77, LvW78] wrongly claimed the ground and excited state to be singlets), and to confirm some other, such as the paramagnetic character of the ground state, the 2.88 GHz zero field splitting of the ground spin sublevels.

Works with a more direct spectroscopic approach, with measurement of excitation and absorption spectra in different conditions of temperature, mechanical pressure, external fields, with one or more excitation frequencies, have also been conducted. Among others we can cite [DH76, BZG+08, TGR+06, TMH+08, NKJ+09].

These works have shown a lifetime (T_1) of the excited state of $\approx 10 - 20$ ns, (depending on the spin state), a spin coherence lifetime (T_2) of ≈ 0.35 ns, and a coherence of emitted photons of ≈ 10 ns. Moreover, these works, combined with theoretical works using group theory and ab initio calculating approaches [LR96, GJB+96, ZWG07, GFK08, LD08, HDWH08]

have indicated the existence of shelving states, which are spin singlets, and participate to the excitation-relaxation process.

All these results contribute to depict the characters of the single isolated NV centre, as a quantum system which is stable under optical excitation, and has an electronic spin state which is possible to measure and change (polarise) with optical techniques.

We will discuss with more details the characteristics of the NV centre in the next chapter 2.

1.3 Addressing single centres

To be able to address a single NV centre, some details have to be considered. Spontaneously occurring NV defects in natural diamond are usually too abundant, so that they form clusters, and is very difficult to find single isolated centres. Recent improvements of the techniques to fabricate synthetic diamonds, and to produce in them the right concentration of NV centres (cfr. e.g. [BBC+09, MGG+09]), have made accessible to scientific research high purity crystals with the right concentration: not too low, so that the defects are easy to find, but not too high, so that they don't form clusters.

Once the right quality of samples is obtained, to optically address a single NV defect the second issue to face is the development of a suitable technique to find and address single centres. In a transparent crystal optical techniques can be used. A coherent light (laser) source and a single photon detector can be optically coupled to the crystal with a *confocal microscope* (cfr. e.g. [GDT+97]). With such a microscope a small area of the crystal containing a

single defect can be excited, and an highly contrasted image can be collected. The suitable spectral filtering can select only the photoluminescence (PL) emission from the defect, and let the NV centres stand clearly out from the surrounding crystal in the confocal image. If the scanning actuator is accurate and repeatable enough, after an imaging scan the microscope can be re-centred on a defect found in the image, and experiments on a single centre can de performed.

1.4 Resonant and non-resonant excitation and emission

To optically excite NV centres, we can use light with a wavelength either resonant with the transition that has to be targeted, or tuned with its *phonon assisted* excitation band in the visible region (about 600-800 nm) [DH76, JW06], with a non-resonant wavelength. With such a non-resonant excitation, the interaction between photons and electrons is mediated by *phonons*, i.e. quanta of vibrational energy of the crystal lattice. This means that a photon with a higher energy excites an electron from the ground state to a higher excited level of the spectrum, which from there decays to a lower excited state with a non-radiative process, transmitting one or more phonons to the lattice, and then decays to the ground level, emitting a photon (photoluminescence). Moreover, this decay to the ground level can happen with the emission of just a photon, or the emission of some phonons together with a less energetic photon. All the possible combinations of resonant and

non-resonant excitation and emission mechanisms are described in figure 1.1.

The probability of phononic interactions is of course strongly dependent on the temperature. At low temperature the vibrational exchange has low probability, so that in the emission spectrum the *zero phonon line* (ZPL) is narrower, down to the *lifetime limit* (indeterminacy in the emission energy connected to the indeterminacy in the emission time by the Heisenberg relation $\Delta E \Delta t \leq h$) and stands out of the phonon-assisted emission band, with an almost dark gap between the two. The line width increases with the temperature, and the phonon assisted band becomes higher and wider, up to the room-temperature situation, where the ZPL is sometimes hardly distinguishable, sunk in the phonon assisted band.

1.5 Quantum information processing

To illustrate some applications of the NV centre, we introduce the important subject of the *quantum information processing* (QIP). This is a field devised by Feynman in 1982 [Fey82], when he presented the idea to exploit the content of information in the state of a quantum system, and the peculiar way in which it is transferred and modified, according to the postulates of quantum mechanics. The original idea from Feynman was in particular to use a quantum system to perform computational simulations of the physical behaviour of other quantum systems more efficiently than any classical computer. In particular there are known calssical algorithms able to simulate a quantum system in an arbitrary state, but with an exponential computational cost, while it is believed that exist quantum algorithms able to do it

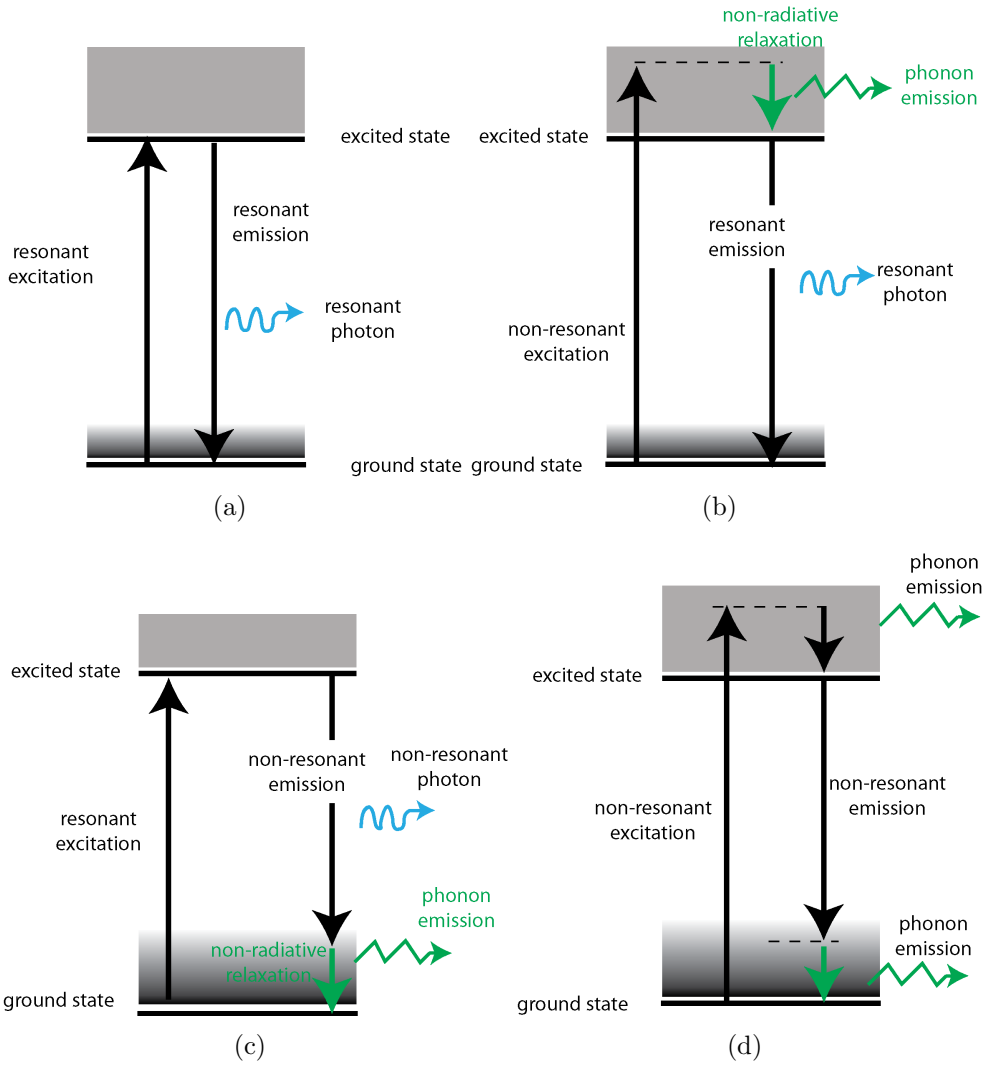

Figure 1.1: simplified description of possible excitation and relaxation mechanisms of the defect. a) resonant excitation, all-radiative emission. b) Resonant excitation with phonon assisted emission of a red-shifted photon. c) non resonant excitation to an higher level, emission of a phonon, and then emission of a resonant photon. d) non resonant excitation and non resonant emission of a red-shifted photon and two phonons

to a polynomial computational cost [NC00].

For the first years QIP has been just a theoretical subject, and contributed to motivate efforts for a deeper understanding of quantum mechanics (cfr. e.g. Deutsch [Deu85]), and this effort is still in progress, leading to deeper understanding and possibly a re-formulation of quantum mechanics in terms of information-theoretic constrains on Nature (cfr. e.g. [Fuc02]). A turning point in the development of QIP has been the work done by Shor in 1994 [Sho94], followed in 1996 by Grover [Gro96]. Those works are two example of algorithms specifically designed for a quantum computer, which exploit its superior computational power, and turned QIP from an interesting theoretical idea into an practical and useful project to realise. Since then the subject has become more and more attractive and popular among scientists, and has witnessed great progress, as can be appreciated e.g. in the book by Nielsen and Chuang [NC00].

In his work of the 1995 [DiV95], DiVincenzo devised five criteria required to realise a quantum computer, namely:

1. well defined qubits
2. qubit initialisation
3. qubit measurement
4. coherence over the time required to execute a quantum algorithm
5. a universal set of logic gates

These general criteria can be used as a reference, although new approaches

to QIP make some of the criteria outdated, and require a rethinking of such criteria [PDK10].

1.6 Application as quantum-bit

We left as last what is probably the most exciting application for the NV centre: its use as *qubit*.

As we will see in more detail in the following, the ground state of the NV centre is a spin triplet, and 1.945 eV (637 nm) higher from the ground state there is another spin triplet excited state. In a crystal without local mechanical stress and no external fields, the $m_s = \pm 1$ spin sublevels of the ground state are degenerate, and are separated from the $m_s = 0$ sublevel by 2.88 GHz. Moreover, optical excitation-emission cycles between the two spin triplets can be considered as (mainly) *spin preserving* [MHS06]. Recent experiments have reported long coherence times for the spin state, of the order of milliseconds [BNT+09].

In assessing the characteristics of NV centres as qubits, is natural to compare them with other possible physical systems which in the past have been considered as possible qubit candidates. Among the earliest candidates, on which a lot of work has been done in the past are *ion traps*, arrays of ions at low temperature, kept in place at short distance by each other by means of magnetic fields [Ste97, SBS98, PM03, PC04, HHR+05, Cou09].

Another approach to realise a qubit has been to use single *quantum dots*, either using as logical states the ground and excited states of the electrons [LWS+03], or using the electrons spin [PJT+05] [KFE+05] [HvBV+05]. Then,

is worth citing the approaches that use more abstract quantum bits, using techniques as nuclear magnetic resonance (NMR) [CLK+00] or Cooper's pairs (*charge qubit* or *superconducting qubit*) [NPT99, WRP09].

Other attempts have been made with other defects in other solid state materials, as e.g. phosphorus impurities in silicon [Kan00].

Back to the NV centre, considering the sophisticated techniques developed for electron spin resonance (ESR) [LvW78, IKU+92], and optically detected magnetic resonance (ODMR) [GvO91, HMEA06], the most promising approach is to use the spin state of the defect as a qubit, i.e. a quantum observable which complies with the DiVincenzo criteria. In particular, because of the specific spin sublevels arrangement, with the partial degeneracy of the ground triplet sublevels, the two logical states of the qubit will be the $m_s = 0$ on one hand and the $m_s = \pm 1$ on the other hand.

In figure 1.2 we show a more detailed sketch of the energy levels structure, with the spin sublevels, the 2.88 GHz resolution between the ground triplet sublevels, and the shelving state.

The first technique to optically interact with (i.e. measure and change) the electronic spin state of the NV centre involves the use of non resonant excitation. The technique relies on the following properties:

- the optical excitation-emission cycles between the ground and excited spin triplets states is mostly spin preserving; but there are small probabilities that the spin changes because of a decay to the shelving state

- because of selection rules, from the shelving state (which is a spin singlet) the electrons decay only to the $m_s = 0$ spin sublevel of the

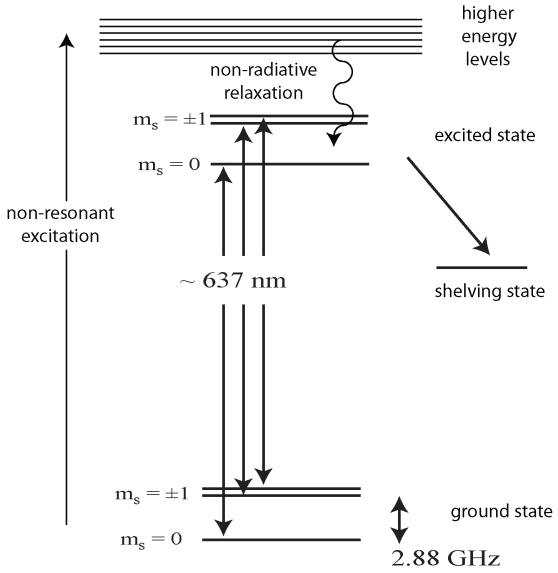

Figure 1.2: a more detailed (but still simplified) sketch of the energy levels structure, where we show the spin sublevels of the triplet states and the shelving singlet state

ground state

- the shelving state has a rather long lifetime (of the order of milliseconds)

- the probability for an electron in the excited spin triplet state to decay to the shelving state (instead of the ground state) is much higher (about 30%) if the spin is $m_s = \pm 1$ and rather low if it is in $m_s = 0$

With these properties, is possible to force the electrons in the $m_s = 0$ spin state just applying a long enough excitation: after many excitation-relaxation cycles there is more and more probability for each electron to decay to the shelving state, and through this to the $m_s = 0$ ground state. There is no need for the excitation to be resonant with the inter-triplets transition, so non-resonant excitation can be used. If we need to populate the $m_s = \pm 1$ state

instead, a 2.88 GHz microwave has to be irradiated on the crystal. Exploiting the above mentioned properties it is also possible to measure the spin state with a short non-resonant excitation: if the spin state is $m_s = \pm 1$, after few excitation-emission cycles the electrons go to the shelving state (and remain there for its long lifetime) while on the other hand if the spin state is $m_s = 0$ we have more excitation emission cycles, because of the smaller coupling constant with the shelving state. So is possible to discriminate between the $m_s = 0$ and $m_s = \pm 1$ depending on the intensity of the photoluminescence intensity.

The use of non-resonant excitation is highly desirable, so that the detection of photoluminescence photons is made with just the proper spectral filtering of the excitation photons.

If sharp monochromatic excitation is available, and it is possible to tune it so to make it resonant with the single spin excitations, it's possible to have a more precise control on the spin state.

In case resonant excitation is used, high speed optical components are needed, to time-resolve the excitation photons from the photoluminescence ones. Again, to manipulate the spin state, microwave irradiation can be used.

[editing note: find references for the optical spin readout techniques]

1.7 Measurement based entanglement

The NV centre energy levels structure is particularly suitable to realise a specific type of protocol, which has the goal to create an entangled state between two qubits using optical excitation and measurements.

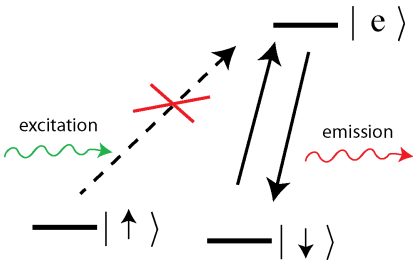

Figure 1.3: L-shaped scheme of the energy levels required by the measurement based entanglement protocol

This protocol has the remarkable ability to prepare two qubits in an entangled state, without any direct, physical interaction between them, and in particular with no specific requirement about the physical distance between the two qubits. The downside is the requirement for the the photons emitted by the two qubits to be nearly indistinguishable.

The first work on this type of protocol has been published by Barrett and Kok in 2005 [BK05], and subsequently improved [LBB+06, BD06, KLBS09].

The protocol requires for each of the two quantum systems an "L-shaped" energy spectrum (cfr. figure 1.3), i.e. two low energy states (which will implement the qubit) and an excited state, which is coupled only with one of the two "ground" states: if the system is in the *coupled* ground state, an excitation photon brings the system in the excited state, with a subsequent relaxation and photoluminescence emission, while if the system is in the non-coupled ground state, the same excitation photon leads to no PL emission.

This abstract description can be applied to the NV centre's energy levels structure: the two logical qubit states ($|\uparrow\rangle$ and $|\downarrow\rangle$) are represented by the $m_s = 0$ and $m_s = \pm 1$ ground state spin sublevels, separated by 2.88 GHz. The excitation will be resonant with the $m_s = 0$ transition to the excited

state, being ineffective if the ground state is $m_s = \pm 1$.

To implement the protocol, first we have to make the PL emission from two NV centres indistinguishable, and to do so, the Stark effect can be used. Since there is no requirement about the distance between the two NVs, electrodes can be arranged so that the applied field affects only one of the defects, so to tune it and obtain indistinguishability.

Other components needed to implement the protocol are a 50/50 beam splitter and two single photon detectors (SPDs). About the SPDs, is worth to mention that the protocol is tolerant to their inability to distinguish between the detection of one photon or two photons. The two qubits need to be optically coupled to the input ports of the beam splitter, while the SPDs will be coupled to the output ports (cfr. figure 1.4).

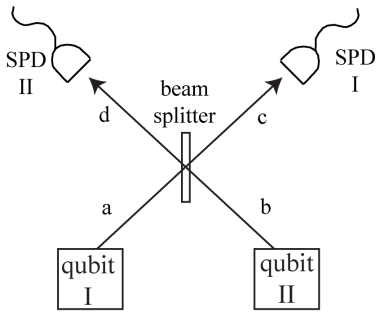

Figure 1.4: sketch of the optical coupling of the qubits and the SPDs to the four ports of the balanced beam splitter

The steps of the protocol are as follows:

1. each of the qubits are prepared in the state $\frac{1}{\sqrt{2}}(|\uparrow\rangle + |\downarrow\rangle)$

2. an excitation pulse is applied, so that $|\downarrow\rangle \rightarrow |e\rangle$ and $|\uparrow\rangle \rightarrow |\uparrow\rangle$

3. a time interval t_{wait} is waited for detections in the SPDs

4. another time interval t_{relax} is waited, for any residual relaxation

5. apply microwave pulses to perform a *spin flip*:
   $|\uparrow\rangle \rightarrow |\downarrow\rangle$ and
   $|\downarrow\rangle \rightarrow |\uparrow\rangle$

6. repeat for a second time steps 2, 3 and 4.

Now, we have to say that protocol is not deterministic, i.e. each time it is performed it can succeed or fail. But on the other hand depending on the outcomes of the photon detections in the SPDs, we can know for sure if the entangled state has been successfully created. For these reasons the protocol is said to be *non deterministic* and *heralded*.

After having presented the protocol describing it step by step, let's now see how it works, following the evolution of the system while the steps are performed. We will represent a state of the total system as a tensor product of the state of the two qubits times the state of the electromagnetic field, using for the latter the *number of photons* representation.

after initialization the state of the total system is the following superposition:

$$[|\downarrow\downarrow\rangle + |\uparrow\downarrow\rangle + |\downarrow\uparrow\rangle + |\uparrow\uparrow\rangle] \otimes |0,0\rangle$$

before the beam splitter the state of the total system is:

$$|\uparrow\uparrow\rangle \otimes |0,0\rangle_{a,b} + |\downarrow\uparrow\rangle \otimes |1,0\rangle_{a,b} + |\uparrow\downarrow\rangle \otimes |0,1\rangle_{a,b} + |\downarrow\downarrow\rangle \otimes |1,1\rangle_{a,b}$$

after the beam splitter the state of the total system is:

$$\begin{aligned} & |\uparrow\uparrow\rangle \otimes |0,0\rangle_{c,d} \;+\; |\downarrow\uparrow\rangle \otimes [|1,0\rangle_{c,d} + |0,1\rangle_{c,d}] \;+\; |\uparrow\downarrow\rangle \otimes [|1,0\rangle_{c,d} - |0,1\rangle_{c,d}] \\ = \;& |\uparrow\uparrow\rangle \otimes |0,0\rangle_{c,d} \;+\; [|\downarrow\uparrow\rangle + |\uparrow\downarrow\rangle] \otimes |1,0\rangle_{c,d} \;+\; [|\downarrow\uparrow\rangle - |\uparrow\downarrow\rangle] \otimes |0,1\rangle_{c,d} + \\ & \qquad + |\downarrow\downarrow\rangle \otimes [|2,0\rangle_{c,d} - |0,2\rangle_{c,d}] \\ = \;& |\uparrow\uparrow\rangle \otimes |0,0\rangle_{c,d} \;+\; |\psi^+\rangle \otimes |1,0\rangle_{c,d} \;+\; |\psi^-\rangle \otimes |0,1\rangle_{c,d} \;+ \\ & \qquad + |\downarrow\downarrow\rangle \otimes [|2,0\rangle_{c,d} - |0,2\rangle_{c,d}] \end{aligned}$$

where we have defined the two *entangled states* $\psi^{\pm}$ as

$$\begin{cases} |\psi^+\rangle \equiv |\downarrow\uparrow\rangle + |\uparrow\downarrow\rangle \\ |\psi^-\rangle \equiv |\downarrow\uparrow\rangle - |\uparrow\downarrow\rangle \end{cases}$$

after a detection if a detection occurs in only one SPD (e.g. SPD1) the state of the system becomes a mixture, and the density matrix is:

$$\rho^+ = \frac{1}{2}|\psi^+\rangle\langle\psi^+| + \frac{1}{2}|\downarrow\downarrow\rangle\langle\downarrow\downarrow|$$

after the spin flip the state of the total system is:

$$|\uparrow\uparrow\rangle \otimes |0,0\rangle_{c,d} \;+\; |\psi^+\rangle \otimes |1,0\rangle_{c,d}$$

after a second detection if it occurs only in the same SPD of the previous step (SPD1 in our example) we can discard the other state from the

mixture, and can conclude that the system is in the *entangled state*

$|\psi^+\rangle$.

1.8 Cluster state approach to quantum information processing

[editing note: in this subsection I want to briefly introduce cluster state approach, and connect it to meas. based entanglement. about half a page]

In this section we want to briefly give account of an approach to quantum information processing which is alternative to the *circuit model*, and is closely related to the measurement-based entanglement protocol just seen, adding more perspective to the motivations behind the scientific work on NV centres. The circuital approach represents the information processing as a flow of information passing through a sequence, or a complex circuit of *quantum logic gates*. This alternative approach, which we can call *cluster states approach* or *measurement-based approach* to QIP, makes no use of logic gates, and so it makes obsolete some of the DiVincenzo criteria we have seen above.

The key element of this approach is the *cluster state*. This is the quantum state of a set of qubits which have some amount of entanglement between them. In particular, the entanglement is always between couples of qubits so that, if we represent the qubits in a regular mesh, only first neighbours can be entangled (cfr figure 1.5). The specific pattern of the entanglement is linked to the specific algorithm to be performed.

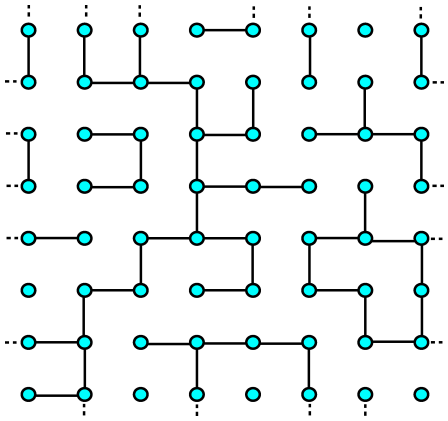

Figure 1.5: a very simple representation of a cluster state: segments represent entanglement between couples of qubits

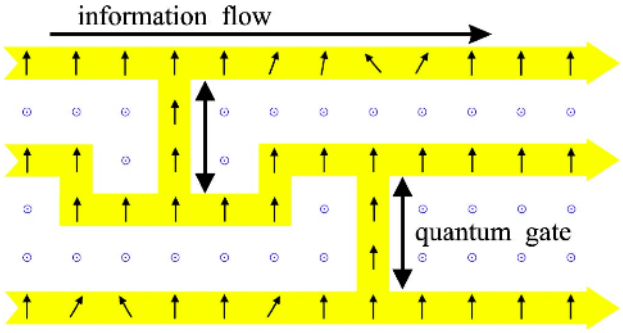

Figure 1.6: representation of the information flow in a cluster state. This figure has been copied from [RBB03]

The seminal work on this approach has been published in 2001 by Raussendorf and Briegel [RB01, BR01]. A subsequent article in 2003 [RBB03] gave more insight and proved the universality of the approach (editing note: check last statement).

In the scheme in figure 1.6 (taken from [RBB03]) the logical qubit is represented by a row, and each column represent a step in the algorithm. In this approach, the entanglement and the measurements implement the behaviour of ?two qubit gates? in the circuital approach.

The non-deterministic but heralded characteristic of the Barrett-Kok protocol is nicely matching with this approach: first the cluster state is built, and all the entanglement needed is created, taking as long time as needed (since we are not in the *runtime* of the computation, and assuming we are well within the dephasing time of the qubits.). Only once all the entanglement procedures have been carried out, the algorithm is performed. The advantage with respect to the circuital approach is that there is no need to control the interaction between the qubits during the ?run-time? of the algorithm. Actually, no interaction is needed at all, since the entanglement is created and stored in the cluster state before the algorithm starts. Only measurements (of the suitable qubits, in the suitable base) are needed to perform the algorithm.

[editing note: the last part needs some touch-up]

1.9 Application of an NV centre as a single photon source

What we have seen about the NV centre leads also to another convenient application: its use as cheap, stable and easy-to-handle *single photon source* [LO05]. In cases where the wavelength is not important, a room temperature set-up can be used, and where monochromaticity is required, low temperature and some spectral filtering can be implemented, so to exploit the narrow ZPL linewidth and the dark gap before the phonon assisted emission band. Some impressive demonstrations of this use have been performed (cfr. e.g. [KMZW00, BKB+02])

Although a single photon source is something useful in several fields, one of its most important applications is quantum cryptography, which can be considered as part of quantum information processing. Quantum cryptography, or more properly *quantum key distribution* (QKD), uses the quantum properties of a physical parameter to encode and transmit a random string that can be then used as cryptographic key to encode confidential messages (cfr. e.g. [BB84, BBB+92]). The Heisenberg indeterminacy relation and the concept of *no-cloning* is exploited to make impossible for a third party to eavesdrop the message without being detected by the legitimate communicating parties. Since a cryptographic key is exchanged instead of the actual message, the possible eavesdropping will lead to no information leak, but only to the compromission of a key, which can be just discarded.

A single photon source can be extremely important for QKD, specially if com-

pared to the use of weak coherent pulses (WCP). In QKD the WCP technique consists of approximating a real single photon source with a pulsed source, attenuating the intensity of the pulses down to the point when on average one photon (or even less) is present in each pulse. The eavesdropper can exploit the statistical discrepancy in the number of photons in each pulse, and perform the so called *photon number splitting attack* [BLMS00]. Although the risk of photon number splitting attacks can be mitigated using so called *decoy techniques* (cfr. e.g. [**?**]), this discussion makes clear the advantage of the use of a *real* single photon source in QKD.

Chapter 2

The NV colour centre in the diamond crystal

2.1 Modeling

In literature there is abundant work on the defect centres of crystals in general. [editing note: here I would like to find and cite some early work on the spectroscopy of defect centres in crystals in general]

More recently, due to the new interest mentioned in the introduction, works on the NV centre in particular have been increasingly published. Rather recent review articles have been published by Jelezko et al. in the mid '00 [JW04, JW06].

Here we try to give an organic account of the experimental results and the understood theoretical description of the centre elaborated so far by the scientific community.

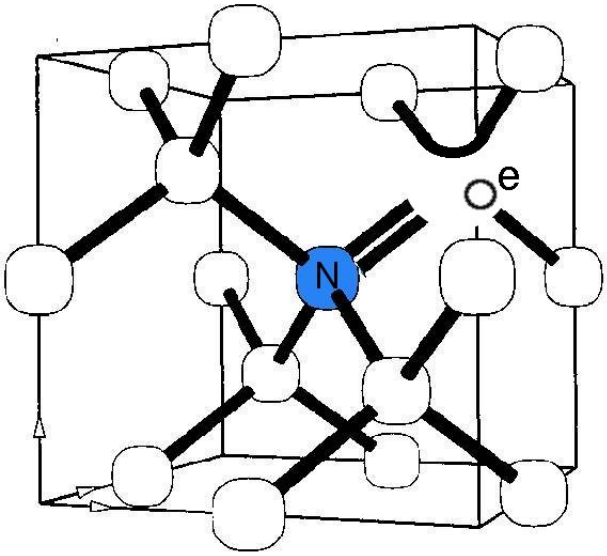

Figure 2.1: a schematic of the diamond crystal cell with an NV defect along the $[1, 1, 1]$ direction

2.1.1 Spectroscopy

Some defects, as e.g. the neutral vacancy, do not show paramagnetic resonance, and for their study mainly optical and mechanical methods are used. A lot of defect centres in solids are known, that are optically active, but in most cases the magnitude of the photoluminescence signal of a single centre is too weak to be detected, either because of a too small oscillator strength, or because of metastable states, that limit the fluorescence quantum yield. In the work by Davies et al. of 1992 [DL92] there is a study that covers the most of the defects that are related with vacancies. Among the other, are reported two absorption bands at 1.673eV and at 3.150eV and called GR1 and ND1 respectively, that are shown to be related with the neutral charged vacancy defect (V^0) and the singly negatively charged vacancy defect (V^-) respectively.

Among the first references about the NV centres we find reports on the conditions in which the characteristic spectral lines where produced in the absorption spectra of diamond. At that time (mid 60's) only natural diamonds were available, and abundant work was done to characterise spectroscopically the different types of natural diamond.

Dyer and du Preez in '65 report [DdP65] optical absorption experiments, and conclude that the main impurities in diamond are nitrogen atoms. In this work is also present a classification of diamond types, based on the absorption properties, which is as follows:

type IIb is a very pure diamond, with no nitrogen and no paramagnetic resonance

type IIa is a relatively pure diamond where some nitrogen single atom substitution defects can be found, at a concentration of about 20 ppm

type Ib is diamond with presence of single atom nitrogen substitution impurities, about 100 ppm

type Ia is diamond with coexistence of neutral and singly negatively charged vacancy defect centres, and type "A" and "B" nitrogen aggregates. The A nitrogen aggregates are relatively simple aggregates of impurities, where two nitrogen atoms substitute two carbon atoms in two adjacent lattice sites. The B nitrogen aggregate is a more complex aggregate where four nitrogen atoms lay around a vacancy [JW06].

In this early work, one of the first references to the NV centre, is reported that after damaging with radiation some type Ib diamond, known to contain

isolated nitrogen atoms, and subsequently annealing it at temperatures above 900 K, new features appear in the absorption spectrum, and among them, one with a characteristic 637 nm (1.945 eV) zero phonon line.

A more systematic work on the spectral properties of this defect has been done in the mid-late '70s (cfr [Dav74, DH76], addressing natural occurring clusters of NV defects, investigating spectral and geometrical properties (symmetry) and the connection with the linear polarization of the absorbed radiation.

typical low temperature spectrum A typical photoluminescence spectrum taken in our lab from an NV centre in an high purity CVD monocrystalline sample at 77 K is shown in figure 2.2. We can easily observe the Raman peak at about 572 nm, the NV^0 ZPL at about 575 nm, the second order Raman band between about 600 - 620 nm, the NV^- ZPL at about 637 nm, and its phonon assisted band up to about 750 nm.

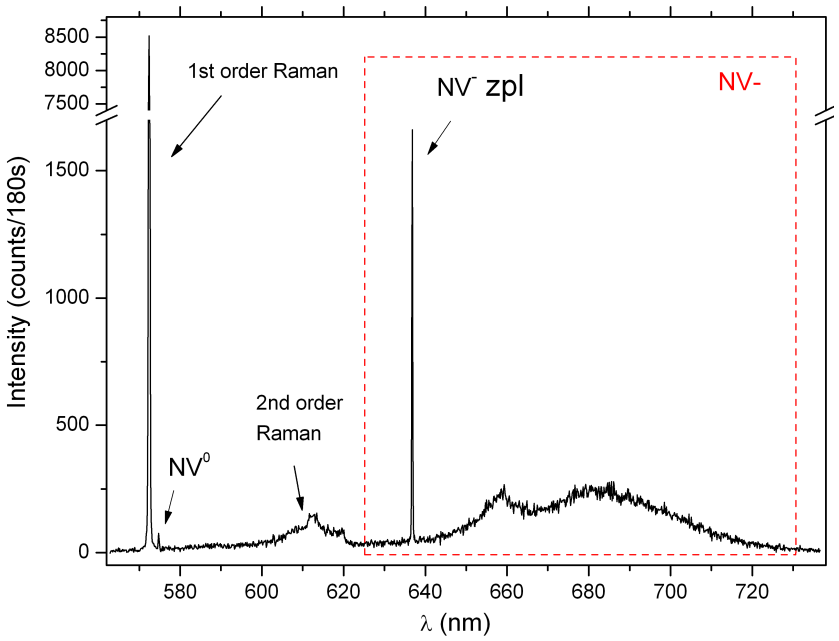

Figure 2.2: photoluminescence spectrum from an NV centre in an high purity CVD monocrystalline sample at 77 K

2.1.2 Results based on other experimental techniques

Another approach to study the diamond is *magnetic resonance*. The electron paramagnetic resonance (EPR) or electron spin resonance (ESR) technique was devised in 1944 by Zavoisky [ZAV46], and independent work has been done in the same years by Bleaney [Ble51, BI51] (who has later directed the Clarendon Laboratory in Oxford from 1957 to 1977). This technique consists in applying a static magnetic field to a material known to have unpaired electrons. These electrons can have their spin parallel or anti-parallel to this field, these two states having two different energies. The separation in energy is proportional to the applied field, and transitions between these two states can be induced by irradiation of microwaves. An EPR spectrum is obtained either tuning the magnetic field or the microwave frequency, and registering the resonance with the electronic transition.

In 1977-78 Loubser and van Wyk published an important work on EPR measurements of several defect centres (mainly Nitrogen related) in natural and synthetic of diamonds [LvW77, LvW78]. In [LvW78] the authors define names for the ESR systems in diamond, following the naming system suggested by Watkins for irradiated silicon and germanium [Wat65]: each system is designated by the initial letter of the laboratory where it was discovered, followed by a number indicating the order of discovery as nearly as possible. This, and other similar work [Wal79] suggest to correlate the *optical centre* with the ZPL at 1.945 eV (studied also in a precedent work by the same authors [LvW77]) to the ESR centre named W15, found in irradiated type Ib diamond, after annealing at 600° C.

Other work on the magnetooptical properties of the NV centre in diamond has been carried out in the groups of Manson [WWH+98, HWW+97, MWM96, ZFF+04], Glasbeek [vOMG88, OG90, GvO91], and Rand [RBSR91, RLB94, RSLR92].

Other papers report on the properties of diamond on this subject are [Dav81, vOG89, IKU+92, JSLP93, HMF93a, HMF93b, Dav94, HGA06, HMEA06, FEN+09, BIS+09, NKN+10, SRX+10]

These works lead to several conclusions on the centre: a lifetime (T_1) of the excited state of $\approx 10-20$ ns, (depending on the spin state), a spin coherence lifetime (T_2) of ≈ 0.35 ns, and a coherence of emitted photons of ≈ 10 ns. Moreover is shown that the *ground state* is a *spin triplet*, and this information leads to the statement that the centre has to have *an even number of active electrons*.

Stress A big part of the present research is devoted to the relationship between the local stress in the crystal and the effects of this stress on the spectral properties of the defect (cfr cap. 4).

Early systematic work on this subject has been conducted by Kaplyanskii in the early '60s [Kap64a, Kap64b], when he published several articles with studies on the behaviour of defect centres in cubic crystals. He worked in general on the behaviour of centres with symmetry lower than that of the hosting crystal, and reported about the *piezospectroscopic effect* which will be described later (cfr. 4).

The later work by Hughes and Runciman [HR67] proceeds along the same lines, and concentrates on centres with tetragonal and trigonal symmetry,

reporting some mathematical relationships between the stress tensor and the shift and splitting of the spectral lines.

In the following years other work on the effect of stress has found more details [AvK85]

First conclusions on the model By looking at these features of the photoluminescence spectrum and of the paramagnetic resonance, the hypothesis was made that the defect included a single vacancy and an isolated nitrogen atom. Moreover, polarization measurements gave informations about the possible symmetries of the system [CN71].

Based on all these experimental evidences, has been concluded that the NV centre consists of a substitutional nitrogen atom, with a vacancy in one of the first-neighbour lattice sites, and has a C_{3V} symmetry (cfr fig 2.1).

Since the number of active electrons has to be even, it means that an extra electron has to join the 3 electrons coming from the neighbouring carbon atoms, and the two from the nitrogen atom, so to form a once negatively charged NV^- defect centre.

It has to be noted that most of the results mentioned so far have been obtained from experimental work on *clusters* of defects, in *ensamble measurements*. At the end of '90s, several groups have managed to manipulate single defects [GDT+97, DTJ+99, DFT+99], and this has opened the possibility to acquire more informations about the centre, and on the other hand to think about the single photon source and qubit applications mentioned in the introduction.

2.2 Energy levels

[editing note: in this section I want to give details on the energy spectrum, citing works on this subject, as Lenef, Delaney, Manson, Tamarat, Santori, Kurtsiefer and Fu. At least one figure with the energy levels will be included. Maybe a second, showing the splitting]

Several works can be found in literature, which provide for a theoretical model of the NV centre. In particular, *ab-initio* calculations [LR96] [LD08] are performed collecting the physical information about the system, applying quantum mechanical and other theoretical knowledge, and calculate from there the electronic structure and the energy spectrum. The steps to develop such model are usually to start using the LCAO method, i.e. building the electronic quantum states using linear combinations of atomic orbitals. To this end, the number of free electrons to take into account is considered. As seen, since the ground state is a spin triplet the number of free electrons has to be even. The accepted physical model is with 6 free electrons, of which (cfr. figure 2.1):

- 3 come from the dangling bonds of the carbon atoms around the vacancy
- 2 come from the dangling bond of the nitrogen atom
- 1 extra electron comes from the crystal

and the extra electron makes the centre negatively charged (NV^-).

Both cited works start the calculations with sp^3 hybridised atomic orbitals (tetrahedral symmetry) of the carbon atom (from the three dangling bonds

between the carbon atoms and the vacancy) and one from the nitrogen atom. Then, linear combinations of these atomic orbitals (LCAO) are built, to form *molecular orbitals* (MO). The linear combinations are built according to group theory applied to molecular quantum mechanics (cfr. e.g. [WG59], chap. 12). From previous experimental evidences, the symmetry group of the centre is identified as the C_{3V} group. So, each molecular orbital must be also linear combination of functions belonging to the same *irreducible representation* of the C_{3V} symmetry group, which are A_1, A_2 and E (Mulliken symbols). A function built as linear combination of functions belonging to an irreducible representation has the symmetry properties of that representation i.e. they *transform according to that representation.*

If the atomic orbitals from the carbon atoms are called *a, b, c*, and the one from the nitrogen is called *d*, then the molecular orbitals are:

$$e_X = \frac{(2c-a-b)}{\sqrt{6-6S}} \tag{2.1}$$

$$e_Y = \frac{(a-b)}{\sqrt{2-2S}} \tag{2.2}$$

$$\nu = \frac{(a+b+c)}{\sqrt{3+6S}} \tag{2.3}$$

$$u = d - \lambda\nu \tag{2.4}$$

where

$$S \equiv \int (a\ b)\mathrm{d}\tau \tag{2.5}$$

$$\lambda \equiv \int (d\ \nu)\mathrm{d}\tau \tag{2.6}$$

are overlap integrals.

Orbitals 2.3 and 2.4 transform as the A_1 representation, while 2.1 and 2.2 transform as E.

multi-electron molecular orbitals So far, the MOs built are representing a single electron in the molecular potential (single-electron molecular orbitals). Multi-electron molecular orbitals can be built as Slater determinants of the single-electron ones. But then, again, linear combinations of such determinants will be needed, to comply to the symmetry properties of the centre.

Applying Hund's rules will then be applied to these results, taking ino account the properties of the orbital part of the wave functions, as well as their spin part, energy levels can be calculated.

Finally, after the building of the unperturbed molecular orbitals a *perturbative approach* is used, building the hamiltonian with terms such as spin-orbit, spin-spin and Jahn-Teller interactions as well as a term representing the strain.

Taking into account these interactions, the final outcome of the ab-initio calculations can be obtained, in terms of the energy levels, and their dependence with the stress.

naming convention As usual in molecular spectroscopy, electronic orbitals and energy levels are named after the Mulliken symbol of the irreducible representation they transform as, and we have seen that the irreducible representations of the C_{3V} symmetry group are A_1, A_2 and E. A spin multiplicity apex is then adding on the left (cfr. e.g. [HB80] page 49-50).

energy levels A scheme of the NV energy levels and sub-levels is presented in figure 2.3, taken from [MHS06].

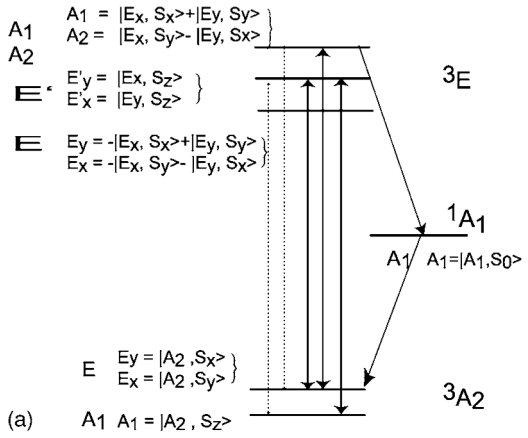

Figure 2.3: The energy levels of the NV centre. The spin triplet $^3A_2$ ground state, spin triplet orbital doublet ^3E excited state and the spin singlet $^1A_1$ excited shelving state are shown [MHS06] (editing note: possibly, change this image)

The main characteristics of the energy spectrum are:

- the A_2 ground level and the E excited level are spin triplets
- there is at least one A_1 level at an intermediate energy, which is a spin singlet and acts as *shelving state*

- the ^3E excited state is an orbital doublet, which in absence of strain is degenerate or close to degeneracy
- the ground state is split by the spin-orbit interaction in a spin singlet and a spin doublet, with a separation of about 3 GHz.
- the transition between the $^3A_1$ ground state and the ^3E excited state is (mostly) spin preserving
- the splitting of spin sublevels is dependent on the local conditions of the defect, such as strain, local fields, and possible other defects in the proximity
- the transition rates from the excited x and y spin sublevels to the shelving state are much higher that that of the z one
- the lifetime of the shelving ^1A level(s) is much longer than that of the ^3E one

2.3 Geometry of the NV centre

In figure 2.4 we report the structure of the diamond crystal lattice. Here we want to discuss about the possible orientations, and other geometric details of the NV colour centre in the diamond crystal lattice.

2.3.1 NV axis directions

First of all, if we fix a lattice site for the substitutional nitrogen, we have four possible first-neighbour sites for the vacancy position. In principle, for

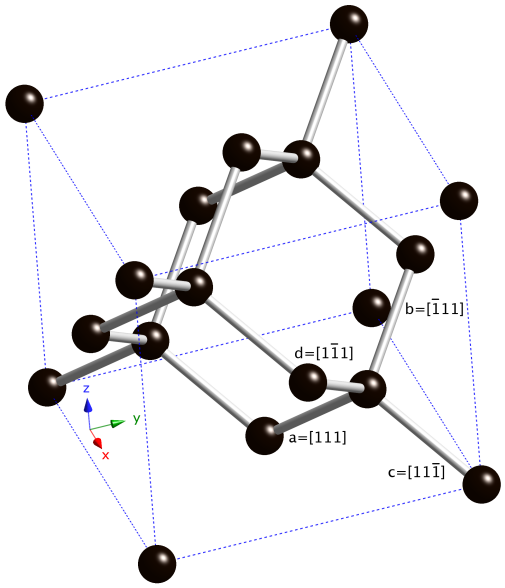

Figure 2.4: Schematic of the unitary cell of the diamond crystal lattice. The crystal reference, and the possible directions of the NV defect axis are indicated

each choice of two adjacent lattice sites we have two possible defect orientations, obtained swapping the nitrogen atom and the vacancy. But there are experimental evidences (cfr. e.g. [DH76]) which indicate that these two are indistinguishable in the spectroscopic measurements. This means that we will consider four possible geometrical directions of the NV axis in the diamond lattice.

If we use as reference the crystal lattice, we can see (cfr. figure 2.4) that the possible directions for the NV axis are along the vectors $[111], [\bar{1}11], [1\bar{1}1]$ and $[11\bar{1}]$. Here and in the following we will use a convention to name these four directions, using a lowercase letter in the following way:

Table 2.1: conventional names for the possible directions of the NV axis

label	direction
a	$[111]$
b	$[\bar{1}11]$
c	$[\bar{1}\bar{1}1] = [11\bar{1}]$
d	$[1\bar{1}1]$

2.3.2 ^3E_x and ^3E_y orbitals directions

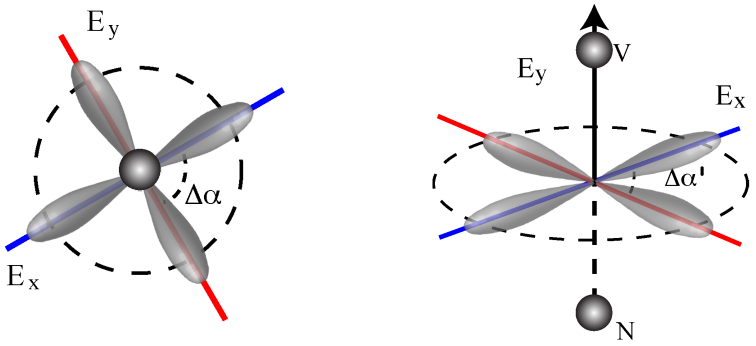

(a) view along the NV axis (b) view from an angle

Figure 2.5: Sketches of the geometrical model, with the orbitals E_x and E_y and the orbitals plane in evidence

Once we have discussed the possible positions of the NV axis with respect to the lattice reference, we have now to discuss the geometry of the *orbitals* around the NV axis. We have seen that the ^3E excited state is an orbital doublet and a spin triplet, with the two orbitals being degenerate in energy in absence of stress. According to LCAO ab initio calculations (editing note: check the references for this; is it in [LR96], or in [LD08]? or elsewhere?), the electronic orbitals for this two excited states (called ^3E_x and ^3E_y) are elongated, with the axis of the lobes laying perpendicular to the NV axis and perpendicular to each other. If the stress is absent, the NV defect has

cylindrical symmetry, so the directions of the two orbitals are undetermined, within the plane perpendicular to the NV axis. In the following we will call this plane *the orbitals plane*. If some mechanical stress is locally present in the lattice, this will deform the centre, which will loose the cylindrical symmetry: *the stress tensor will determine a specific direction for the* ${}^3E_x$ *and* ${}^3E_y$ *in the orbitals plane*. In figure 2.5 a sketch of the NV centre alone is shown, with the NV axis, the ${}^3E_x$ and ${}^3E_y$ orbitals, and the orbitals plane. In figure 2.5(a) we represent the NV defect as it appears looking along the $[1, 1, 1]$ direction, i.e. along the NV axis. The two orbital axes (in red and blue) are perpendicular to each other ($\Delta\alpha = 90°$) while the orbital plane is perpendicular to the observation direction. Here and in the following we represent the orbitals plane with a round edge, to convey the idea of the cylindrical symmetry. Drawing the plane as a circle also represents graphically the assumption that the two orbitals have the same behaviour as electromagnetic dipoles, and in particular they emit the same PL intensity.

When the NV is observed from a direction different from $[1, 1, 1]$ (cfr figure 2.5(b)) a projection of the orbitals axes on the *observation plane* can be seen, and the angle $\Delta\alpha'$ apparent between the orbitals, i.e. the angle between the *projections*, can of course in general be different from 90°. Moreover, the circle that represents the orbitals plane in a perpendicular projection, will appear as an ellipse if it is observed from other directions, as it appears in figure 2.5(b). In what follows, we will call the projection of the orbitals circle on the observation plane the *orbitals ellipse*.

2.3.3 The crystal lattice and the sample's edges

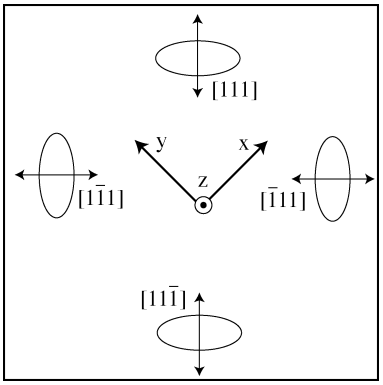

Figure 2.6: The orientation of the crystal lattice with respect to the edges of the sample, where the edges are along [110] and [$\bar{1}$10]. The four possible orientations of the NV centre, and the relative projections of the orbitals planes (ellipses) are shown, while in the centre is reported the crystal reference.

Now we want to refer what we have described so far about the NV centre geometry to a reference solid with the observation equipment (what we will call *the observation reference*). The relationship between the crystal's lattice reference and the observation reference will depend on how the sample is cut with respect to the lattice, and of course on how the sample is mounted with respect to the observation equipment. The samples usually come as a flat squares, with approximate dimensions of about $1 \times 5 \times 5$ mm, and are mounted so to be observed perpendicularly to the flat square facet.

One possible way of cutting a sample is represented graphically in figure 2.6, where we have also represented the orbitals ellipses: the sample's edges can be along [100] and [010], or along [110] and [$\bar{1}$10].

2.4 Relations between spectroscopic parameters and stress

The *piezo-spectroscopy* is the study of the effects obtained on the *spectral characteristics* of the photoluminescence emissions of a system, when *mechanical stress* is applied on it. To describe the piezo-spectroscopic effect on the ZPL emission of the NV^- defect centre we can consider as relevant spectroscopic parameters the *splitting* of the two resolved peaks and the overall *shift* of the doublet with respect to the unperturbed ZPL. In early '60s Kaplianskii has reported studies on piezo-spectroscopy of noncubic or *anisotropic* defect centres in cubic crystals [Kap64a, Kap64b]. In these works the reversible shifting and splitting of spectral lines due to the application of uniaxial stress is reported. Some theoretical models are developed, to explain these effects. One possible theoretical approach is the one using group theory. Mechanical deformation can change the symmetry of the defect, and so its *group of symmetry* can be turned into a smaller subgroup. Then, using group-theoretical arguments it's possible to show that the passage from a bigger to a smaller group of symmetry can lead to the removal of some degeneracies in the energy spectrum of the electronic states [WG59, **?**].

On the other hand, a *perturbative approach* can be used. If we define the

stress tensor $\underline{\underline{\sigma}}$ as:

$$\underline{\underline{\sigma}} \equiv \begin{pmatrix} \sigma_{xx} & \sigma_{xy} & \sigma_{xz} \\ \sigma_{yx} & \sigma_{yy} & \sigma_{yz} \\ \sigma_{zx} & \sigma_{zy} & \sigma_{zz} \end{pmatrix} \tag{2.7}$$

we can define a perturbation operator expressed in terms of the stress tensor components [HR67] as:

$$\begin{aligned} \hat{\mathcal{V}} &= \hat{\mathcal{A}}_1 \left(\sigma_{xx} + \sigma_{yy} + \sigma_{zz} +\right) + \hat{\mathcal{A}}'_1 \left(\sigma_{yz} + \sigma_{zx} + \sigma_{xy}\right) + \\ &+ \hat{\mathcal{E}}_X \left(2\sigma_{zz} + \sigma_{xx} + \sigma_{yy} +\right) + \sqrt{3}\hat{\mathcal{E}}_Y \left(\sigma_{xx} - \sigma_{yy}\right) + \\ &+ \hat{\mathcal{E}}'_X \left(2\sigma_{xy} + \sigma_{yz} + \sigma_{zx} +\right) + \sqrt{3}\hat{\mathcal{E}}'_Y \left(\sigma_{yz} - \sigma_{zz}\right). \end{aligned} \tag{2.8}$$

where the operators $\hat{\mathcal{A}}_1, \hat{\mathcal{A}}'_1, \hat{\mathcal{E}}_X, \hat{\mathcal{E}}_Y \hat{\mathcal{E}}'_X, \hat{\mathcal{E}}'_Y$ are symmetry operators referred to the NV frame of reference (X, Y, Z).

2.4.1 Restriction of the perturbed hamiltonian to the $\{E_x, E_y\}$*eigenspace*

The restriction of the perturbed hamiltonian operator of the system to the eigenspace spanned by the two eigenfunctions relative to the two orbitals E_x

and E_y can be represented by the *secular matrix* [HR67, Kap64a]:

$$\begin{pmatrix} \alpha+\beta & \gamma \\ \gamma & \alpha-\beta \end{pmatrix}. \tag{2.9}$$

If we diagonaise this matrix we obtain:

$$\begin{pmatrix} \alpha+\sqrt{\beta^2+\gamma^2} & 0 \\ 0 & \alpha-\sqrt{\beta^2+\gamma^2} \end{pmatrix} \tag{2.10}$$

If we consider the eigenvalues $\alpha+\sqrt{\beta^2+\gamma^2}$ and $\alpha-\sqrt{\beta^2+\gamma^2}$, we can see how they contain the information about the spectroscopic shift and splitting: α is the overall energy shift with respect to the degenerate eigenvalue of the unrestricted and unperturbed hamiltonian, while $2\sqrt{\beta^2+\alpha^2}$ is the splitting between the two non degenerate eigenvalues.

We also note that the eigenvalue $\alpha+\beta$ (higher energy, lower wavelength) is relative to the E_x eigenstate, and $\alpha+\beta$ (lower energy, higher wavelength) is relative to E_y .

2.4.2 Piezo-spectroscopic equations

The relationship between the α, β and γ parameters, and the components of the stress tensor are [HR67]:

$$\begin{cases} \alpha = A_1 (\sigma_{xx} + \sigma_{yy} + \sigma_{zz}) + 2A_2 (\sigma_{yz} + \sigma_{zx} + \sigma_{xy}) \\ \beta = B (2\sigma_{zz} - \sigma_{xx} - \sigma_{yy}) + C (2\sigma_{xy} - \sigma_{yz} - \sigma_{zx}) \\ \gamma = \sqrt{3}B (\sigma_{xx} - \sigma_{yy}) + \sqrt{3}C (\sigma_{yz} - \sigma_{zx}) . \end{cases} \tag{2.11}$$

This important system of equations expresses the relationship between the spectroscopic parameters and the stress is the key to represent the *piezo-spectroscopy*, which is indeed the stdy of the effect of mechanical deformations on the spectroscopic behaviour of a system.

Is important to stress that the coefficients depend on the orientation of the NV in the crystal, equations 2.11 being valid for the [111] axis direction.

If we apply the appropriate coordinate transformations to the equations we can calculate the other three systems of equations valid for the other three possible orientations of the NV axis:

NV axis along $[\bar{1}11]$

$$\begin{cases} \alpha = A_1 (\sigma_{xx} + \sigma_{yy} + \sigma_{zz}) + 2A_2 (\sigma_{yz} - \sigma_{xz} - \sigma_{xy}) \\ \beta = B (-\sigma_{xx} - \sigma_{yy} + 2\sigma_{zz}) + C (-\sigma_{yz} + \sigma_{xz} - 2\sigma_{xy}) \\ \gamma = \sqrt{3}B (-\sigma_{xx} + \sigma_{yy}) + \sqrt{3}C (-\sigma_{yz} - \sigma_{xz}) \end{cases} \tag{2.12}$$

NV axis along $[11\bar{1}]$

$$\begin{cases} \alpha = A_1 (\sigma_{xx} + \sigma_{yy} + \sigma_{zz}) + 2A_2 (-\sigma_{yz} - \sigma_{xz} + \sigma_{xy}) \\ \beta = B (-\sigma_{xx} - \sigma_{yy} + 2\sigma_{zz}) + C (\sigma_{yz} + \sigma_{xz} + 2\sigma_{xy}) \\ \gamma = \sqrt{3}B (\sigma_{xx} - \sigma_{yy}) + \sqrt{3}C (-\sigma_{yz} + \sigma_{xz}) \end{cases} \tag{2.13}$$

NV axis along $[1\bar{1}1]$

$$\begin{cases} \alpha = A_1 (\sigma_{xx} + \sigma_{yy} + \sigma_{zz}) + 2A_2 (-\sigma_{zy} + \sigma_{xz} - \sigma_{yx}) \\ \beta = B (-\sigma_{xx} - \sigma_{yy} + 2\sigma_{zz}) + C (\sigma_{yz} - \sigma_{xz} - 2\sigma_{xy}) \\ \gamma = \sqrt{3}B (-\sigma_{xx} + \sigma_{yy}) + \sqrt{3}C (\sigma_{yz} + \sigma_{xz}) . \end{cases} \tag{2.14}$$

2.4.3 Mohr's circle

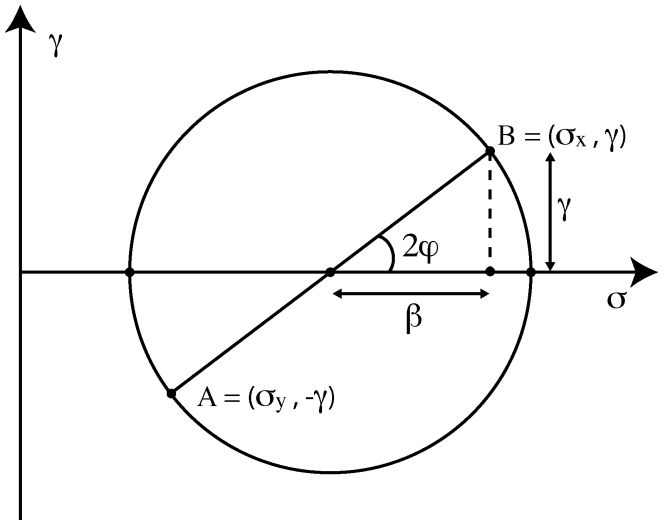

Figure 2.7: sketch of the Mohr's circle

Mohr's circle is a tool to represent graphically the mechanical stress applied to a solid. Here we will describe the simpler case of plane stress. Let's consider a cartesian plane, where on the horizontal axis we represent the

tensile-compressive stress, and on the vertical axis the shear stress

On the other hand, we know that in the 2×2 symmetric matrix representing a plane stress, the diagonal components represent the *normal* (i.e. tensile-compressive) stresses , and the off diagonal component represent the *shear* stress. If σ_x and σ_y are the two components of the normal stress, and γ is the shear stress, we will represent this stress with the two points $A = (\sigma_y, -\gamma)$ and $B = (\sigma_x, +\gamma)$ on the plane (cfr. figure 2.7). In this way any plane stress can be represented, with two symmetrical points on the circle. Diagonalise the stress tensor can be seen as a transformation of the reference such that the shear stress vanishes and the stress becomes normal: we have rotated the reference by an angle φ, so to make it overlap with the principal axes of the system. In the Mohr's circle representation this corresponds of a rotation of the two points A and B by an angle 2φ, so to bring them on the horizontal axis (no shear stress).

Now, with an *intuitive argument*, we can identify the 2×2 matrix representing the (restriction of) the hamiltonian 2.9 with the restriction to the orbital's plane of the stress tensor (plane stress). We can indeed imagine that if the stress is along the orbitals, no shear stress is felt by the orbitals' system, and the stress tensor is represented by a diagonal matrix (off-diagonal elements = shear stress). On the other hand we know that if we diagonalise the (restriction of) the hamiltonian of a system, we obtain a diagonal matrix with the eigenvalues as diagonal elements. But to diagonalise the hamiltonian means to change the generic reference into the reference of the eigenvectors, i.e. the orbitals. So, for both matrices, the diagonalisation corresponds to a rotation that brings the reference on the orbitals axes directions. Of course

this is just an intuitive argument, but it is possible to formalise it, but this formalisation goes beyond the scope of this thesis.

If we assume this identity, then, looking at the diagonalised form 2.10 of the (restriction of) the hamiltonian we can do the following identifications:

$$\alpha \equiv \text{energy shift} \leftrightarrow \text{abscissa of the centre of Mohr}'\text{s circle}$$

$$2\sqrt{\beta^2+\gamma^2} \equiv \text{energy splitting} \leftrightarrow \text{diameter of Mohr}'\text{s circle}$$

$$\varphi \equiv \left\{ \begin{array}{l} \text{angle by which rotate the stress tensor} \\ \text{in order to diagonalise it} \end{array} \right\} \leftrightarrow \text{half of the angle in Mohr}'\text{s circle}$$

This said, if we define $s \equiv 2\sqrt{\beta^2+\gamma^2}$ for the splitting, from Mohr's circle representation we can derive the following relations between the parameters α, β, γ, on one side, and the the energy shift d, energy splitting s and angle ϕ on the other side:

$$\left\{ \begin{array}{l} \alpha = d \\ \beta = s\cos 2\phi \\ \gamma = s\sin 2\phi \end{array} \right. \tag{2.15}$$

This equation connects the experimental spectrographic parameters with the parameters appearing in the left-hand side of equations 2.11.

2.5 Polarization spectroscopy

In the previous section 2.3 on the geometry of the centre, we have seen that the excited triplet state ^3E has two degenerate orbital states ^3E_x and ^3E_x, with lobes perpendicular to the NV axis and to each other (cfr. figure 2.5). We have also mentioned that in a simplified model we can consider the elongated lobes of these two orbitals acting as electric dipoles, so that when they emit a PL photon, this is linearly polarised, with *the electric field along the direction of the orbital's axis.*

Moreover, in section 2.4 we have also seen that the mechanical stress present in the NV area of the crystal can remove the degeneracy of the two orbitals, and produce a splitting in the spectral line of the PL emission. This leads to the possibility to study the polarization characteristics of the PL spectra of an NV in an highly stressed region, and in particular the different behaviour of the two spit peaks each belonging to one of the two orbitals. Combined measurements of the spectra and of the polarization of the PL emission can give important informations on the geometry of the NV centres and on the local stress tensor present in the crystal.

Chapter 3

Experimental techniques

In this chapter we describe the design of the scanning confocal microscope (SCM) built during the DPhil project, and specifically devised for the requirements of the project. The assessment of its performance is first done analysing some images so to measure the field of view and the resolution, and then performing a monitored, long exposure acquisition, so to measure the mechanical and optical stability over time. In section 3.1.1 we give a description of the setup, in section 3.2.2 we report the resolution and field of view measurements, in section 3.2.1 we report the stability measurements. Finally, we devote a section to the details of the alignment procedures.

3.1 The scanning confocal microscope

Confocal microscopy is a technique devised by Minsky in 1956, and later patented in 1961 [Min61]. The key concept of confocal microscopy is to focus a point-like illumination source on a small area of the sample, and

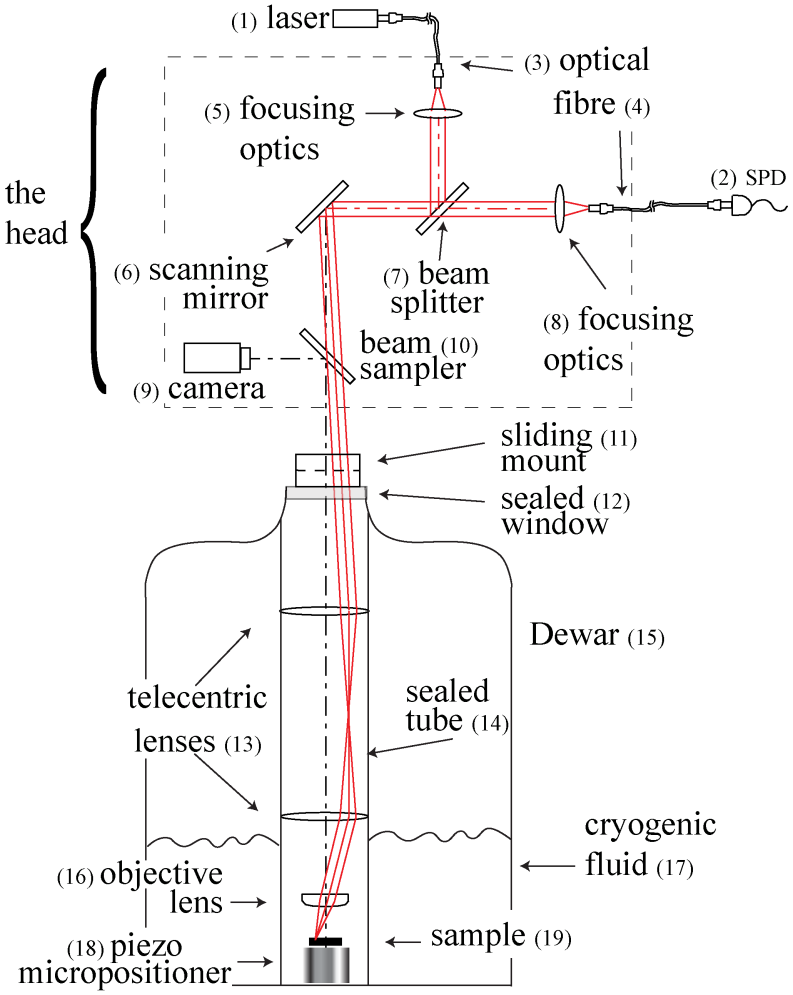

Figure 3.1: a schematic of the experimental set-up. The confocal microscope is partially enclosed in the low-temperature Dewar (15), while the head, formed by the excitation (5) and collection optics (8), the beam splitter (7), the scanning mirror (6) and the camera (9), are at room temperature. A laser source (1) and a single photon detector (2) are optically coupled to the microscope via fibre optics.

then use a small optical aperture (pinhole) to reject all the light scattered from the other areas of the sample, and collect only light from the small region directly illuminated by the the excitation beam. The In 1978 Cremer devised a scanning confocal microscope using a laser beam as illumination source [CC78], giving a much better approximation to a point-like source, than a pinhole in front of a conventional lamp as in the initial 1956 design. The benefits of a confocal design are high contrast and high spatial resolution, since the scattered light from other areas of the sample, which in conventional microscopy is responsible for the background optical noise, is rejected. This spatial selectivity of the collection gives to the system also the ability to detect the position of the image not only in the plane x,y transverse to the optical axis, but also along the optical axis z itself, creating highly defined 3D optical images. The drawback of this design is that for a fixed position of the microscope only the small illuminated area, of the order of the microns, is imaged. To image a wider area, a scanning technique is required: several adjacent positions in the sample will be imaged, with an even sequence, and for each position the collected intensity will be recorded. Subsequently these optical values will be interpreted as *picture elements* (pixels), and an extended image will be reconstructed joining together all of them.

Many scientific works have successfully applied the confocal microscope design, to several fields, as e.g. [GHS92, GDT+97, DFT+99, MSLK05, BN09].

3.1.1 Opto-mechanical design

In figure 3.1 a schematic of the optical setup is shown. In the present section the reference to the parts shown in this figure will be done with a number in parentheses (#). For the requirements of the present project, and namely low temperature, high spatial resolution, efficient light collection from emitters deep in a sample, mechanical stability over long acquisition times, of the order of magnitude of the hours, a specific optical design was required. A so called *cold lens* system, with the sample and the objective both at low temperature has recently been devised [HSK+08], which provides for most of the requirements. Similarly to this cited work, our setup has been designed around the idea of having the sample, together with its holding and positioning mechanics, and the objective lens, all rather far from the other components, by means of a telecentric optical system (13). This choice has several benefits which give the microscope an higher stability and an higher collection efficiency: the telecentric system makes possible to have the sample and the objective optics together deep in the cryostat so that they can reach a stable low temperature, while the rest of the apparatus is at room temperature. Moreover, in this way there is no need for a window between the sample and the objective, so that a rigid mechanical connection between them is possible and optical loss is minimised. Finally, the absence of a window allows to use a standard high numerical aperture objective lens, with short working distance.

A feature which is specific to our design, and constitutes an improvement with respect to the cited works, is the fact that our design does not rely on

piezoelectric actuators to scan the sample. Although slip-stick piezoelectric actuators, capable to work at low temperatures and under vacuum, can allow for several millimetres of travel, their movement is not reproducible and linear enough to be used to move the sample for the imaging scan. So, in the sample scanning approach, the field of view is limited to the maximum extension of piezoelectric rods, which is typically in the range of few microns at room temperature, and a micron or less at low temperatures. To overcome these limits, we use a beam scanning approach: the scanning movement changing the angle of the beam with a beam steering mirror (6). In this context, the telecentric optics allow not to compromise on the width of the field of view, so that the acceptance cone for the scanning beam is the same as if the objective was close to the beam splitter.

The rest of the components follow the standard beam-scanning confocal microscopy design. The excitation source and the photo-detection device are coupled to the microscope via optical fibre, and apart from providing for freedom in the positioning, the collection fibre aperture acts as pinhole to reject the light coming away from the focal area, implementing the central idea of confocal microscopy.

the *head* of the microscope Excitation and collection optical paths reach the splitting component of the setup (7) , which can be interchanged between a beam splitter and a dichroic filter. The beam splitter has the benefit to be transparent to a wide spectral range, so to allow for white light microscopy. On the other hand the dichroic filter doesn't affect the polarization state of light, allowing experiments where the polarization of the excitation photons

is changed. After this coupling element the excitation and collection paths coincide for all the rest of the optics. The next element is a steering mirror (6) which provides for the beam-scanning ability.

The high quality of this component provides for the high spatial resolution and the accurate repeatability of the scanning movement. After several attempts with other devices, the suitable accuracy has been found with the FSM-300 from *Newport Corp.* Before the window of the cryostat there is a beam sampler (10) to send a fraction of the collection beam to an inspection camera (9), and a mechanical junction (11) which allows for a sliding movement normal to the optical axis (alignment). We have the focussing and positioning mechanics for the excitation and collection optics, the beam splitter, the beam steering mirror, the beam sampler and the camera, all mounted on a single metal plate, which guarantees the necessary rigidity between these components, and we will call this part, as a whole, *the head* of the microscope.

The remainder of the components are sealed in vacuum in a tube (14) , to avoid condensation at low temperature. After the window (12) , we have the telecentric lenses in a 4f configuration (13) in f, and then the objective optics (16) . A standard x60 microscope objective (from *Microthek GmbH*) has proven to be resilient enough to the cooling cycles, so to discourage the expense for optics specifically designed for low temperature operation. The sample holder is mounted on a three stages piezoelectric positioner (18) , which provides for the focussing movement along the optical axis (focussing) as well as the transverse movement. The need for wide range of movement at low temperature, to focus the sample and to be able to address as much

of it as possible, has led to the ANPx101 and ANPz101 models from *Attocube Systems AG*. This type of piezoelectric actuators has been originally devised by Pohl in 1987 [Poh87], and it has been successfully used in several applications (cfr. e.g. [Gök94, MSLK05]).

After the splitting device, the collection arm of the microscope is coupled to a single photon detector (SPD) via single mode optical fibre. We use the SPCM-AQR-FC14 single photon counting module from Perkin Elmer Inc..

The single photon counts from the SPD are collected in a computer which also controls the scanning mirror, so that for each step of the scan the position and the counts are recorded. The controlling software developed by our group (using LabView programming environment from National Instruments Inc.) is then able to record the intensity of each pixel, and save it along with their position, and the exposure times (for diagnostic purposes). The same software is able to reconstruct the whole confocal image, and with a point-and-click interface, allows to reposition the focus of the microscope on a desired position of the imaged field of view.

3.1.2 Driving software

During my DPhil project I have participated in the writing and testing of the driving software for the microscope. The main idea was to have in the same piece of software all the tools needed to perform the measurements involved in the project. First of all, the software takes care of the scanning movement of the beam, calculating and applying the right voltages to the FSM-300 steering mirror, via the digital acquisition board. Collecting the counts from

the SPD, and synchronising them with the scanning movement, for each position in the sample the right intensity information is stored in a structured data-file. The software itself is then able to read these data and plot a reconstructed microscopic image of the field of view, using a colour code to represent the intensity. To have the positioning and the imaging functionality in the same piece of software is crucial to allow the *point-and-click* capability: once a poin-tlike feature, with the right dimension, shape and contrast with respect to the background, appears in a confocal image, using the graphical interface is possible to point a cursor on it, and issue to the steering mirror the command to align the microscope to that feature. A nudging command, in each x,y direction, can be given to the steering mirror, to fine adjust the position of the focal point. Finally, we have included a collection mode, called *live mode*, that allows to visualise the number of collected photons in a given time interval, in a continuous way, while the alignment stays on a given position or is fine adjusted (nudge). This allows to operate on the several manual actuators, and optimise optical parameters such as the relative positions of the excitation and collection beam, the alignment of the beam splitters, the focusing optics, etc.

3.1.3 Low temperature

The low temperature is achieved submerging the sample and the objective lens in cryogenic fluid, either liquid nitrogen (LN_2) or liquid helium (LHe). To submerge these components we have devised a sealed cylindrical container (cfr. (14) in figure 3.1), with an optical access window on its top (cfr. (12)

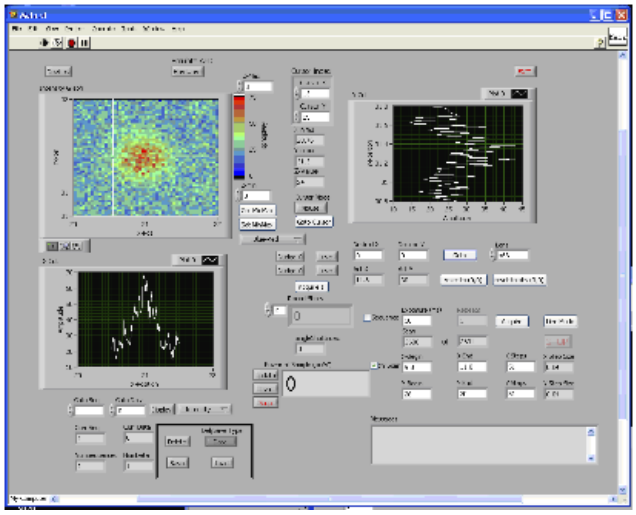

Figure 3.2: a screenshot of the graphical user interface for the LabiView driving and imaging software (figure to be changed with a better one)

in figure 3.1). In this tube vacuum is created, up to 10^{-5} *m bar* pressure, and then filled with helium gas up to 50m bar, to allow for heat exchange. To facilitate the sample mounting operations, is possible to remove this tube from the cryogenic Dewar. On the other hand, the sample holding mechanics, together with the objective and telecentric lenses, are compactly mounted with their mounting plates on stainless steel rods (Thorlabs cage system), and all these part tightly fit in the sealing tube. When room temperature measurements have to be performed, the tube can be mounted directly on the optical bench, in a vertical position, and then sustain the load of the rest of the components (the head). In room temperature measurements, although is possible to use the bare mounting rods structure, the use of the tube is advisable, to avoid air turbulence and mechanically stabilise the optics. When low temperature measurements are required, after the sample mounting session, the tube is sealed and connected to the vacuum pump,

and subsequently filled with the exchange gas. Once the desired internal environment is obtained, the tube is carefully slid in the dewar, with a step-by-step slow procedure, to avoid thermal chocks. A thermalising delay of 10 minutes after each sliding movements of about 5 cm has proven to be slow enough. An holding clamp has to be secured to the tube for each thermalising delays, in order to sustain it. A sealing o-ring flange is provided on the top of the Dewar, but it has failed to sustain the tube in few occasions, so it is not advisable to risk damages to the equipment and let the weight of the tube only sustained by the friction of the o-ring.

3.2 Characterisation of the microscope

3.2.1 Stability measurements

To asses the mechanical stability of the microscope, the following measurement has been devised and performed. After finding a single NV centre in a single crystal bulk diamond sample, the photoluminescence photon counts have been recorded over long periods of time, sampling the intensity with 1 minute intervals, and over an integration time of 10 seconds (cfr. figure 3.3). Since the emission of an NV centre in a bulk monocrystalline sample is known to be stable and not subject to blinking or bleaching, the fluctuations in the collected intensity can be attributed to the equipment itself. For maximum alignment sensitivity, we have reduced the excitation power in order to avoid photoluminescence saturation, with the collected intensity below 5 $\frac{\text{K counts}}{\text{second}}$. Moreover, the measurement has been done with the sample at LN_2 temper-

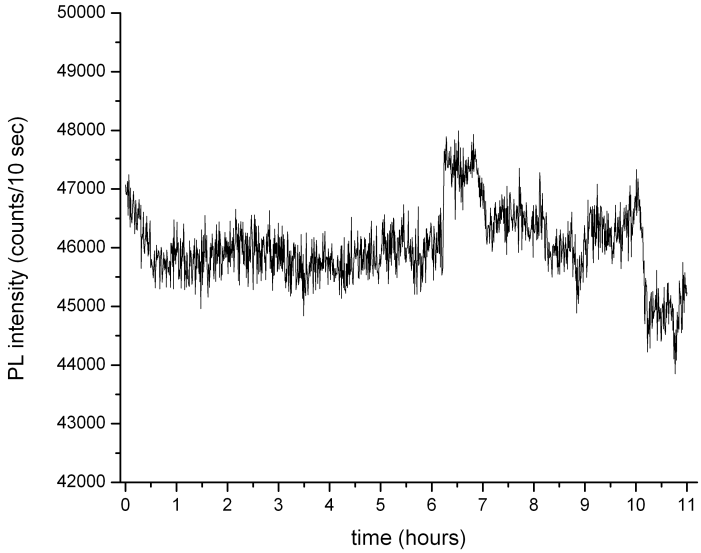

(a)

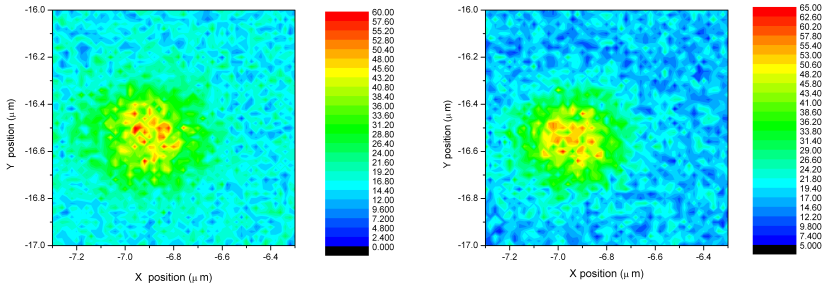

(b)

(c)

Figure 3.3: stability measurements data (a) PL emission photon counts vs time. (b)(c) high resolution confocal images of the NV centre, taken at the beginning and at the end of the acquisition, to measure the spatial stability.

ature. During the measurement the excitation power has been monitored, and has been stable within 5%. The lab temperature has been monitored as well, and has shown to be a crucial parameter. In initial attempts the signal was completely lost when the temperature drifted of few Celsius degrees, in correspondence of the building's central heating night interruption. With the help of an independent heater the lab's temperature has been stabilised within a 5% fluctuation range, and the subsequent intensity measurements have closely followed theese temperature drifts.

To asses the spatial stability, an high resolution image of the NV centre has been recorded before and after the measurement. Comparing the two confocal images we can estimate a spatial drift of about 50 nm in the x, y transverse plane. To assess the drift in z direction, first of all we can notice that the focussing of the NV centre. A quantitative estimate of this parameter is linked to the estimate of the *depth of field* of the microscope, which is discussed in the next section.

In figure 3.3 the intensity plot and the two high resolution images are shown.

3.2.2 Resolution

In figure 3.4 a microscope image of a 100×100 μm region in an high purity diamond sample is shown, where the colours of the contour plot express the number of photon counts per second. High resolution 1×1 μm images of two features, one from the centre and one from the edge of the field of view are shown in figure 3.5. These images report about the good performance of the microscope over a wide spatial range. To proof that a single colour

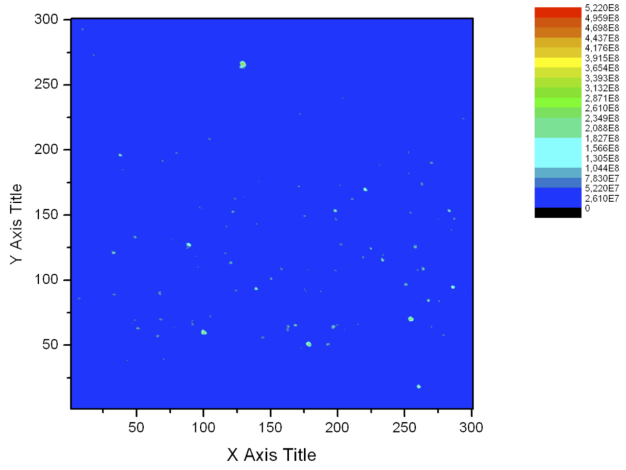

Figure 3.4: wide microscope image

centre, and not a cluster is addressed, a Hambury Brown and Twiss coincidence experiment has been performed, showing the single photon emitter behaviour. Once this test is passed, a single NV centre can be considered as a point-like light source, and so the high resolution images can be seen as the convolution of the point-like feature and the illumination spot, and therefore used to measure the resolution of the microscope. After the Rayleigh criterion the resolution limit has been calculated to be $d_{min} = 381$ nm for an objective optics with $NA = 0.85$, while the measured diameter of the Airy disc is $d = 340$ nm, showing a diffraction limited resolution performance.

3.3 Hambury-Brown and Twiss measurement

[editing note: here a plot of an HBT measurement is needed]

Once some localised features are found in a confocal image of the crystal (cfr. figure A.2), we need to check if this centre in the crystal is a single emitter or a cluster of several emitters. To do so, an anti-bunching measurement of

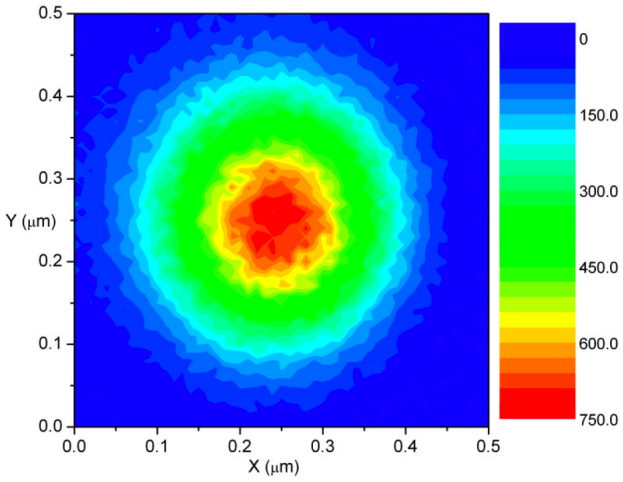

Figure 3.5: high resolution microscope image

the single photons emitted by the feature is performed.

The principle of this measurement is that a single emitter has a dead time between two consecutive photon emissions, and so the minimal interval between to detections is finite.

Some time-correlated acquisition electronics (time correlation single photon counter (TCSPC)) is used to plot an histogram of the time intervals between to consecutive detections in two single photon detectors (SPDs), each collecting photons from the two exits of a beam splitter (cfr figure 3.7). In figure 3.8 we show a plot of two HBT measurements, performed below (solid black circles) and above (white squares) saturation. The two datasets have been analysed and the best fitting curves are shown in red. The fitting functions are [...] (cfr. e.g. [KMZW00]). The experimental data behaviour follows this theoretical model with good agreement, and in particular is clear the change in the shape of the plot when the saturated regime is approached.

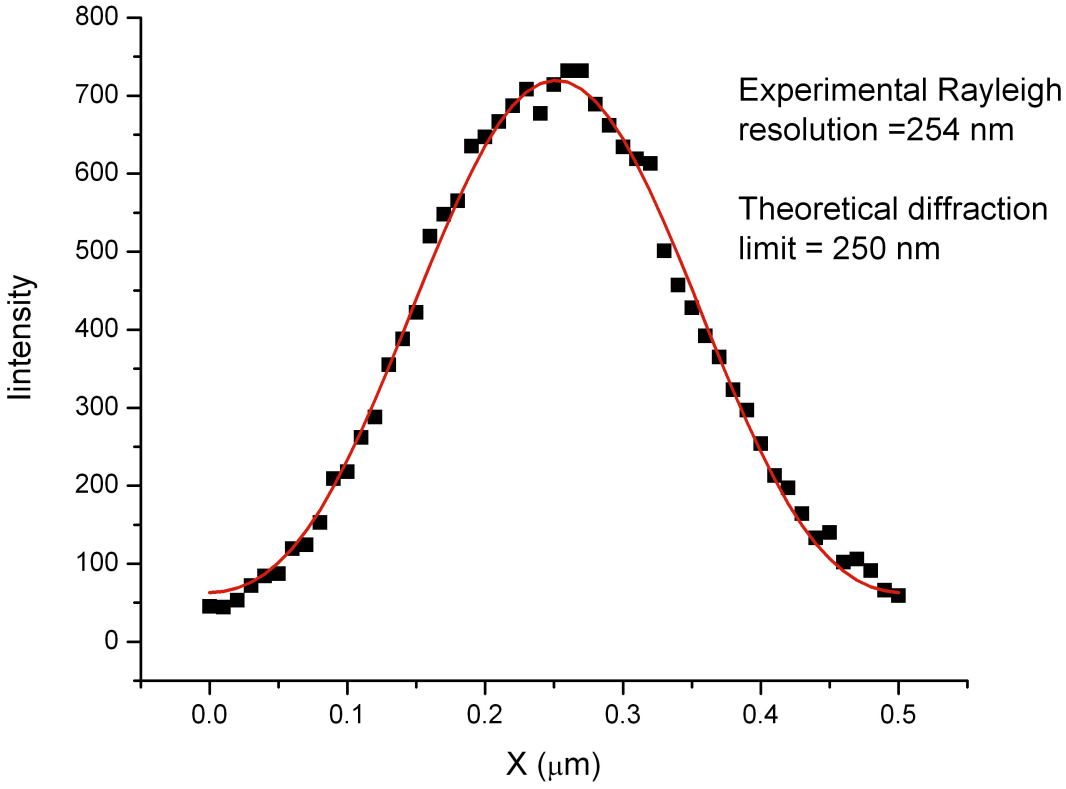

(a) didascalia prima figura

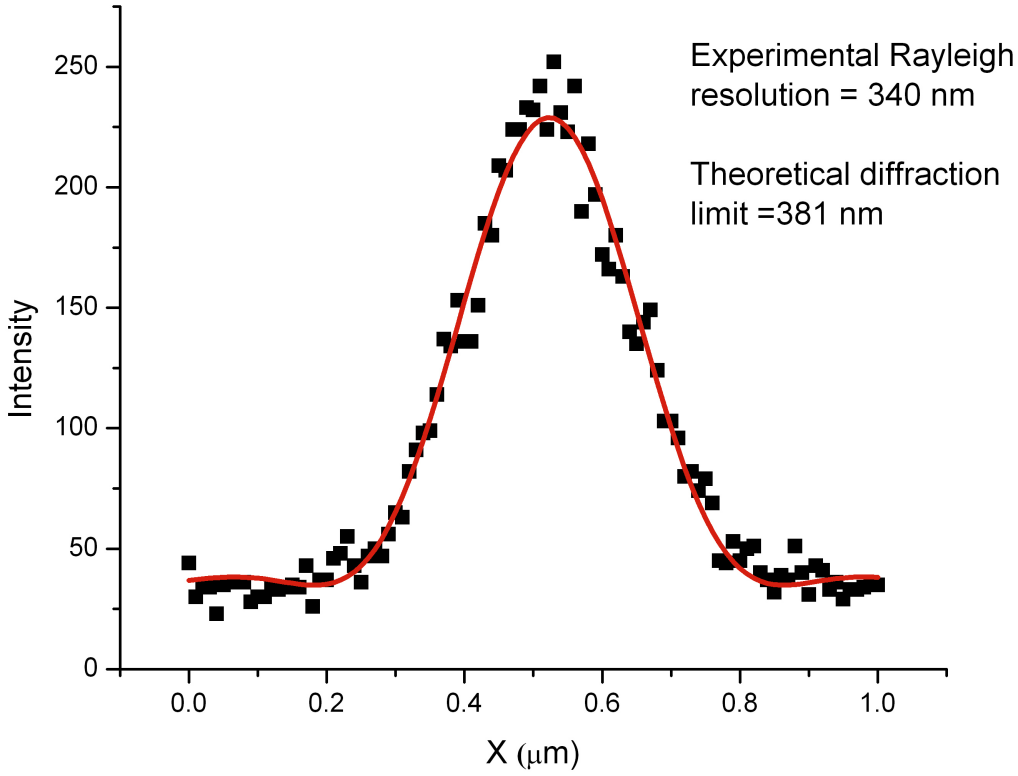

(b) didascalia seconda figura

Figure 3.6: Titolo delle figure

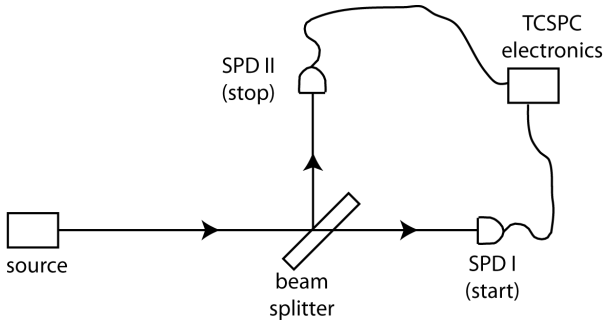

Figure 3.7: sketch of the HBT measurement

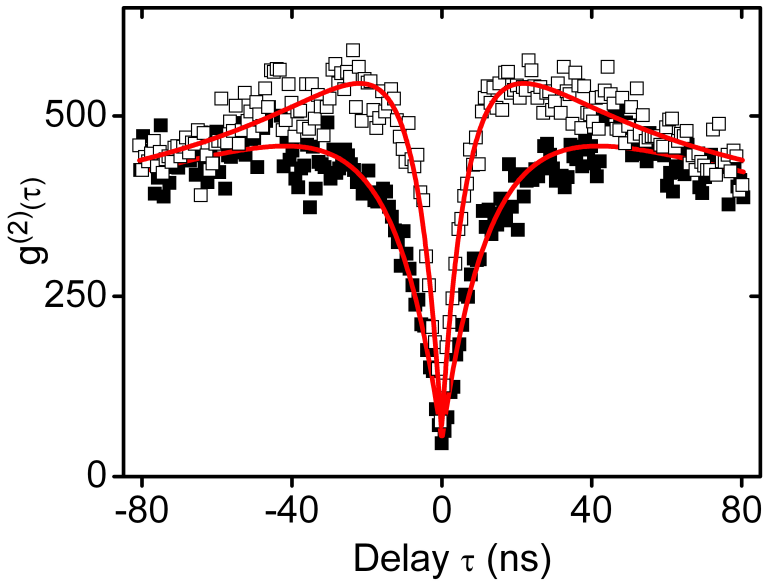

Figure 3.8: two plots of HBT measurement. Solid black circles indicate a measurement performed below saturation, while white squares one performed in saturated regime.

3.4 Alignment of the microscope

In this section we report some details about the procedures and the guidelines aimed at the alignment of the microscope and the optimisation of its imaging capabilities.

As mentioned in section 3.1, the confocal microscopy idea is based on the concept that the light scattered from outside the excited spot is blocked by a pinhole and doesn't contribute to the formation of the image, considerably improving the contrast of the image. Let's set the elements of the microscope, so to describe its alignment procedures. First, we have the excitation beam, which comes out of the focussing optics (marked (5) in figure 3.1), and is focussed on what we will call *the excitation spot* in the sample. Then we consider a *virtual beam*, which we will call*the collection beam*, and which would go from the focussing optics (marked (8) in figure 3.1), and would be focussed in the sample, in what we will call *the collection spot*. The virtual collection beam doesn't have to be confused with the actual real beam which brings the light emitted from the sample, up to the collection optics. On the other hand, the ideal *confocality* condition is obtained when this real beam of light emitted from the sample coincides with the virtual collection beam. We can also say that the condition of *confocality* is obtained when the excitation and collection spots coincide. Moreover, since the goal is to address a single defect centre, we want these two spots to coincide with the position of the defect in the sample. In other words, all the alignment adjustments have the final goal to let three things to coincide: the excitation spot, the collection spot, and the NV position.

3.4.1 Steps of the Alignment procedure

Let's imagine we have just mounted a sample on its holder on the top of the piezo micropositioner, and let's follow a step-by-tep description of the procedure that follow, in order to prepare the microscope for the acquisition of a good confocal image.

beam collimation and centering Before mounting the sample in the microscope, the first procedure is to act on the excitation focussing optics ((5) in 3.1), so to have the beam coming out *collimated*, i.e. with the same diameter along all its length. Moreover, we want the beam to be aligned with the optical axis of the microscope, and central with respect to the mechanical structures (mounting rods). To do so we will act on the beam splitter (7), the beam sampler (10), and the excitation focussing optics (5), while it is preferable to keep the scanning mirror (6) in its central position, so that the scanning movement will have the highest allowance on all 4 sides of its movement when an image will be collected. The best way to work, in this phase, is to remove what we have called *the head* of the microscope (cfr. section 3.1.1), and mount it on the optical bench.

first rough alignment After the sample is mounted on its holder, we act on the z movement of the piezoelectric micropositioner ((17) in fig. 3.1) so to have it at half of the travel extension. In this way we will have as much travel as possible in both directions for the sample's focussing. Then, we want to fix the position of the microscope objective (marked (15) in fig. 3.1) so that the front lens is at about 0.5 mm from the sample's surface. The highest care has

to be taken in doing this, because of the risk of crashing the objective in the sample, and damage the delicate and expensive piezoelectric rod. Once the mechanical mounting is set, we want to fine-adjust this focussing distance, and to do so we will use the z movement of the piezo actuator, and look at the image in the camera (cfr. (9) in fig. 3.1). Shining the excitation laser through the optics, we act on the piezo, and look for the round laser spot to be reflected from the sample's surface and be seen in the camera. Again, to avoid the risk of damage for the piezo, the best is to start from far away, and get near, and not the other way around. This comment might seem trivial, but when we look at the initial camera image we usually just see some diffused scattered excitation light, so we might see a defocussed spot of a beam focussed ways deep in the sample, an wrongly think it is too far instead. Another possible mistake, in the case a rather thin sample is used, is to mistake the reflection from the bottom surface for the one from the top surface. After some attempts, the right experience in estimating the right distance to mount the objective will be achieved. In figure 3.9 here is an example of reflected image of a green excitation beam on the surface of a sample.

head alignment Once we have the reflection of the excitation beam in the camera, we have to optimise the alignment of the head with respect to the rest of the microscope. To do so, we refer to the camera image of the beam spot reflected from the sample's surface, and adjust the sliding mount ((11) in figure 3.1). A combined action on the sliding mount and on the focussing optics will be needed, in order to optimise the shape of

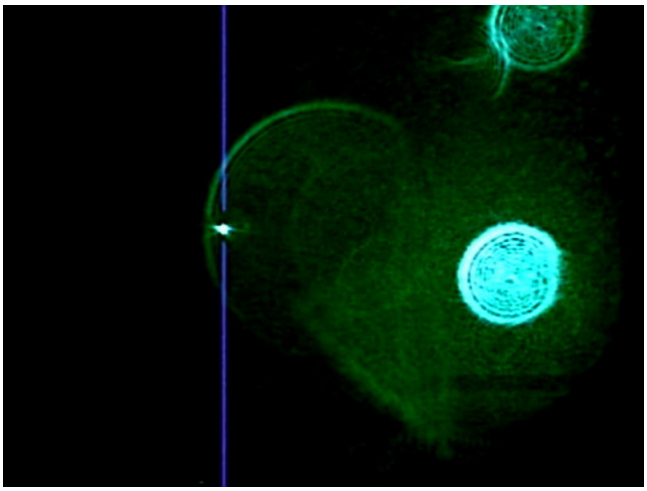

Figure 3.9: an example image of the green spot reflected on the sample's surface, as seen through the camera

the spot, and have it in the central area of the field of view. Since we want to maximise the collection performance of the microscope, rather than its excitation performance, we will connect a laser source to the collection optics (8), rather than the excitation optics (5), and use the spot formed by its beam. Moreover, we will use a red laser as close as possible to the 637 nm wavelength of the NV^- ZPL, so to avoid different behaviour of the collection optics due to chromaticity. The goal is to have the spot as round as possible, and with an uniform distribution of its luminosity. In figure 3.10 we show an example of an image of the spot as seen in the camera.

rough confocality Now we need to align the relative positions of excitation and collection foci to reach the condition of *confocality* (overlapping of the excitation and collection focal points). To have an initial rough starting confocality, it is advisable to use two laser sources, one through the excitation optics and one through the collection optics, as done for the head's alignment,

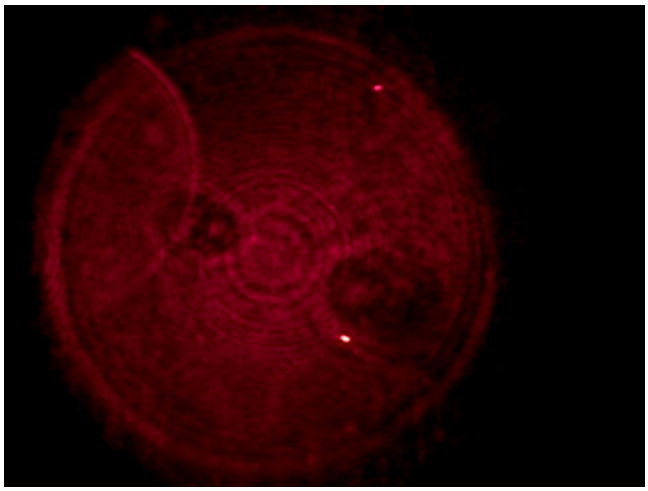

Figure 3.10: an example image of the red spot reflected on the sample's surface, as seen through the camera

and again with the second laser color possibly red so to be close to the 637 nm wavelength of the NV^- ZPL, and avoid different chromatic behaviour in the collection optics. We will shine the red laser through the collection optical fibre, and will have a real collection beam, with a real collection (red) spot, visible in the camera image, exactly as the virtual one mentioned at the beginning of this section. We will focus the beams a bit deep in the sample, so to have biggish spots images on the camera, and then with the mechanical actuators on the collection and excitation optics we will adjust the x,y positions of the spots, as well as their relative focussing, in order to have them to coincide in the camera image. Once we have this initial confocality, we connect the collection fibre to the SPD, and look at the counts. If we are in a particularly pure sample, it is possible that we have very low counts even if we have a good confocality, since no reflection or photoluminescence signal is collected. In this case, a possibility is to move the sample's focussing and have the spot focussed on the surface of the sample, and have an imaging

scan. In this way we will image the possible contamination impurities on the sample, and have some photoluminescence image. Another option is to spend more effort on the previous step, and with the rough alignment try to image some NVs deep in the sample, performing several imaging scans in several areas, to look for a richer NVs density. Which of two approaches is the best depends mainly on the sample. A sample with a clean surface will show very few features in the surface image; on the other hand, if we have a sample with low NV concentration a scan to look for NVs with a non-perfectly aligned microscope might be a waste of time. In any case, if for an intermediate step the alignment to a feature on the surface can be useful, it has to be said that for the final confocality optimisation, an NV centre (or another point-like emitter) is needed to reach the full capabilities of the microscope.

optimise the confocality Once we have the microscope collecting some signal from a single NV centre, we can optimising the confocality, using the SPD counts as a reference. The first and easier positioners to act upon are the excitation x-y tilt positioners. Although acting on the x,y tilt instead of the x,y displacement introduces some misalignment, they are preferable because of their movement's better resolution and stability. As mentioned in section 3.1.1, since the collection optics are horizontal, they have less actuators, and in particular lack of tilt adjustment. This means that during this fine adjustments of the alignment procedure is easier to consider the position of the collection spot as fixed, and move the other positions relative to this. Specially if in this phase we are using an NV centre to align the microscope,

each few iterations of the x and y optimisation, we have to nudge the steering mirror: we remember that here we are trying to let *three* objects to overlap: the excitation spot, the collection spot, and the NV we want to image.

gaussian beams: optimise along z axis Once, after few iterations between x and y have been done, and the highest signal on the SPD has been achieved, the optimisation in the z axis has to be taken care of. To discuss this, we have to take into account the whole beams, and not only the spots. The beams can be modelled as gaussian beams, i.e. approximatively with an hourglass shape, the focus of each beam (what we have called the spot) being the thinnest part of the hourglass shape. This said, when we try to let the two waists coincide with each other, and with the NV centre, we have as feedback parameter the number of photon counts collected into the SPD, but the geometrical situation, as described in figure **??**, can lead to mistakes. In some situations a movement along z can lead to an increase of the counts, but to this could correspond a farther relative position, since the NV could enter in the tail of one of the cones. This could be the case if e.g. the two beams are parallel but separated side by side, with the NV in between, near the foci, with a small overlap of each beam with the NV. A relative movement along z of one of the two beams will let more of this beam to overlap the NV, and this will increase the counts; but the actual confocality has been worsened. These considerations are meant for the optimisation of the *relative* focussing, the one obtained acting on the z position of one of the two focussing optics (5) and (7). The optimisation along z can be obtained also moving the sample's z position (with the piezo micropositioner), so that the

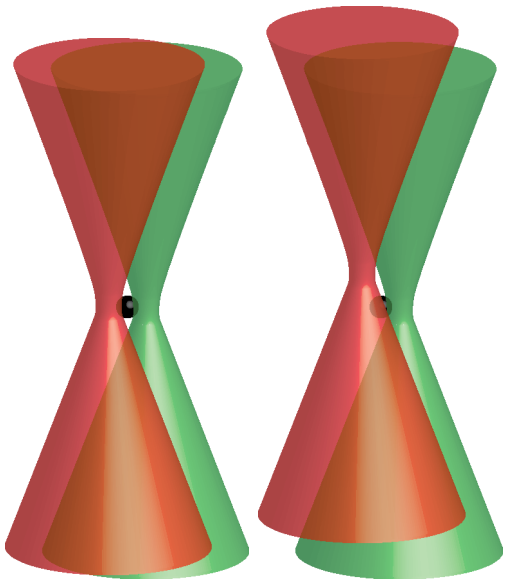

(a) (b)

Figure 3.11: a sketch of the hourglass shape of the excitation and the collection beams, and the relative position of an NV centre (black sphere). Dimensions not in scale. (a) the NV in between excitation and collection focal points, and the two beams are symmetrical, side by side. (b) a movement along z of the excitation beam can lead to an higher count of photons, although this corresponds to a poorer confocality

relative position of the two beams remains the same.

final comments Of course what we have described are only some of the several details to take into account, in order to have the microscope to perform at the best of its capabilities. More than else, the patient iteration of the procedures described is an advisable strategy. Since the value of the SPD counts depend on several factors, this parameter can't be used as an absolute reference to estimate how good is the confocality and overall alignment obtained. A better reference is to consider how sensitive is the collected signal to the adjustment of the x,y position of the excitation beam. In a situation

close to the optimal alignment, a very gentle touch to the knob can let the signal drop by 80%.

These comments conclude this section on the alignment of the microscope.

3.4.2 Optimization

[editing note: in this section I want to report details about the choice of the fibre cores, the injection and collection optics, the beam sampler versus the dichroic mirror, etc. A table should summarise these results]

As we have seen, for the microscope to perform at its best, the confocality condition is crucial. We have seen how the shape of the excitation and collection beams interact with each other when we work for the best alignment. In order to shape the beams, the choice of the right focussing optics (5) and (8) has to be carefully considered. Moreover, the coupling to the objective lens (16) has to be considered. The parameters to choose are the numerical apertures of the focussing lenses (5) and (8). [editing note: to be completed]

Chapter 4

PL spectroscopy of NV centres in highly strained diamond

In this chapter we give a general account of the experimental work conducted on the NV centre during the DPhil project. The first part of the project has been devoted to the building and characterisation of the experimental setup, and in particular the low-temperature scanning confocal microscope described in the previous chapter. As soon as the microscope has been assembled, and while still characterising it, we have started to image high-purity diamond samples and collect spectra from them.

The sample used for our experiments are for the most part high purity, monolithic, carbon vapour deposited (CVD) diamond crystals provided by Element 6 ltd. We have also used some poly-crystalline samples, and some synthetic samples realised with High-Temperature High-Pressure techniques. Several samples have been tested, to find the suitable characteristics, such as NV density, local stress, surface polish etc to address single colour centres.

Some measurements about the NV^-/NV^0 intensity ratio have been performed in an high purity CVD monolithic sample marked as E6-01. For most of the polarization and stress measurements, we have used a sample marked as "E742607-18", which is a flat piece of diamond, about $5 \times 5 \times 1\ mm$ thick, with standard polish on both sides.

4.1 Cross polarised imaging

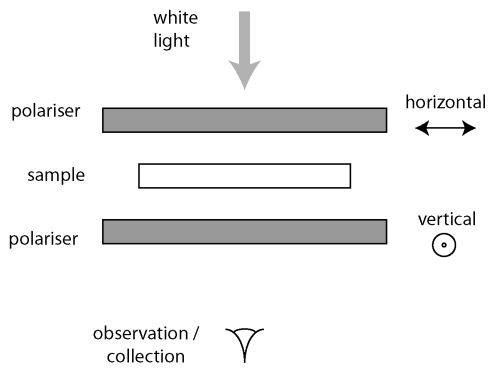

Figure 4.1: schematics of the cross polarised imaging technique: the two polariser are arranged so that their polarisation directions are at 90°, with the sample in between.

The *cross polarisation* imaging technique allows to detect the mechanical stress in isotropic transparent media. In general an isotropic medium by definition has no preferential direction in it's internal structure, so that the polarisation vector of a linearly polarised beam of light is not affected. If a mechanical stress deforms the structure, the medium becomes birefringent, and modifies the polarisation vector's direction of the linearly polarised beam. So, the technique consists in arranging two polarisers at two sides of the

sample, with their directions at 90° (cfr. figure 4.1): if there is no stress, the crossed polarisers block all the light, but the birefringence due to localised strain changes the polarisation vector's direction after the first polariser. So, in the collected image, *bright areas indicate the presence of strain*, and the brightness is a rough indication of the intensity of the strain.

In figure 4.2 we have a cross polarized image of sample E742607-18. In this image we can see an important feature which made this sample ideal for the stress-related measurements: a natural occurring high stress area near the middle of the bottom edge, evidenced in the image with a red oval.

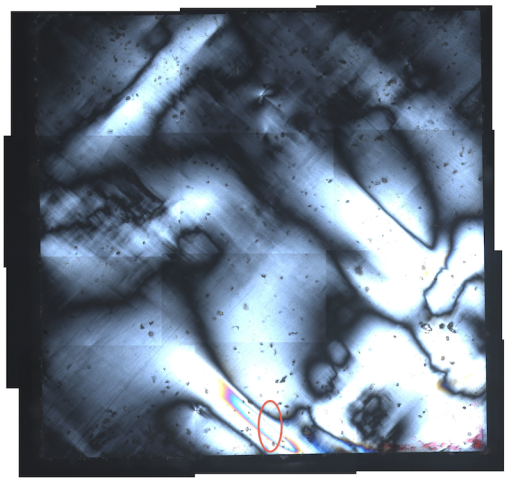

Figure 4.2: Cross polarized white light image of the E742607-18 monolithic high purity CVD sample. Region with high strain highlighted near the bottom edge

In figure 4.3 we show a cross polarised image of a natural diamond sample.

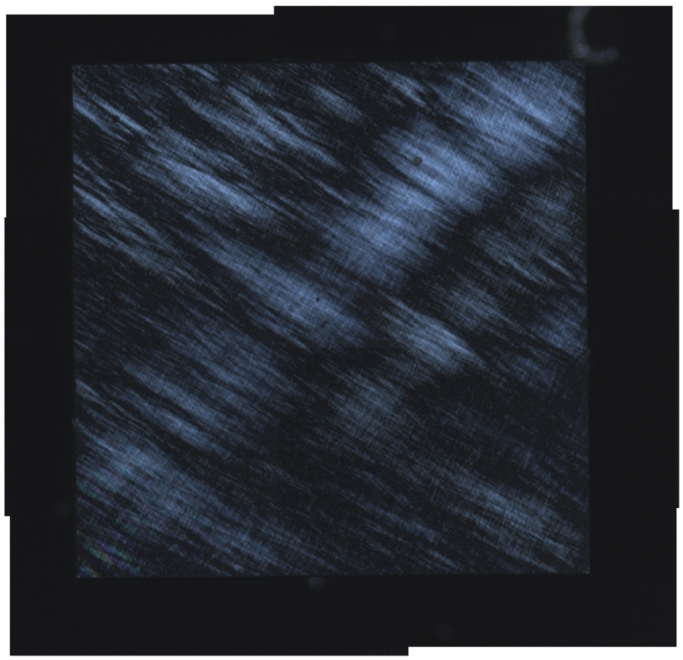

Figure 4.3: cross polarised image of a natural diamond sample, to compare with synthetic sample E742607-18

4.2 Confocal imaging: the search for single NVs

Long time has been spent to find the suitable depth, and sometimes the sample in use had a concentration of NVs so low that only after many imaging scans we have been able to find NV centres.

In figure [...] [editing note: here I want to show a webcam image with the spot, to show the right depth, and produce some calculations and sketches about the depth.]

One of the early problems encountered has been the presence of contamination on the surface of the samples, which was sopping us from collecting images. We have devised a procedure to clean the sample's surface consisting in a preliminary rinse with organic solvent (mainly to remove the vacuum grease used to mount the sample), and then one or more sessions of boiling in an acid mixture of half nitric acid and half hydrochloric acid at about 120 - 150 °C. Care has to be taken for this procedure: a very small beaker has to be used, to minimise the amount of acid and the risks related to it, and also minimising the risk to loose the sample in a too big container. Another problem is that after about 15 - 20 minutes of boiling, the acid starts to produce explosions. With the small amounts used, the explosions are really week, and it's just as the boiling phenomenon concentrates in separate, more concentrate bubbling intervened by periods of stillness. The risk in this phase is that the sample is thrown out of the beaker, so a lead is advisable. A glass microscope cover slip is ideal to cover small 5cc beakers.

In image 4.4 we report a confocal image of the PL emission from a monolithic

CVD high purity sample marked as E742607-18. The excitation is a green laser source (532 nm), and the temperature 77 K. In image 4.5 a close up at higher resolution.

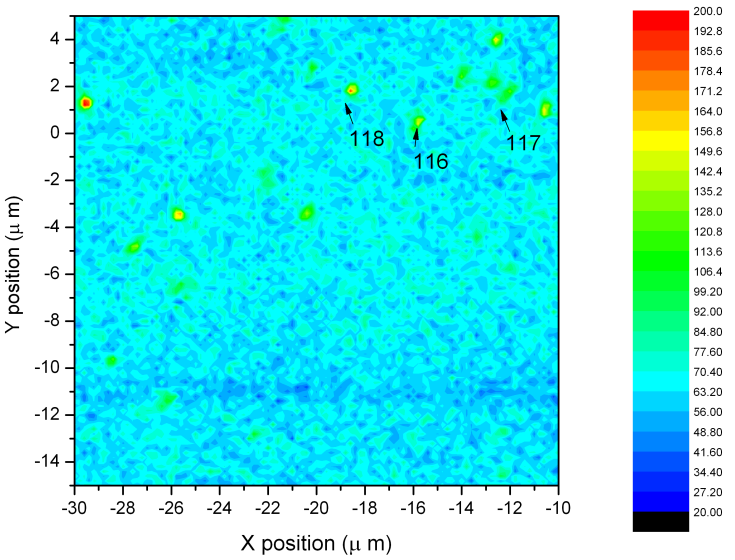

Figure 4.4: confocal image from sample E742607-18

.

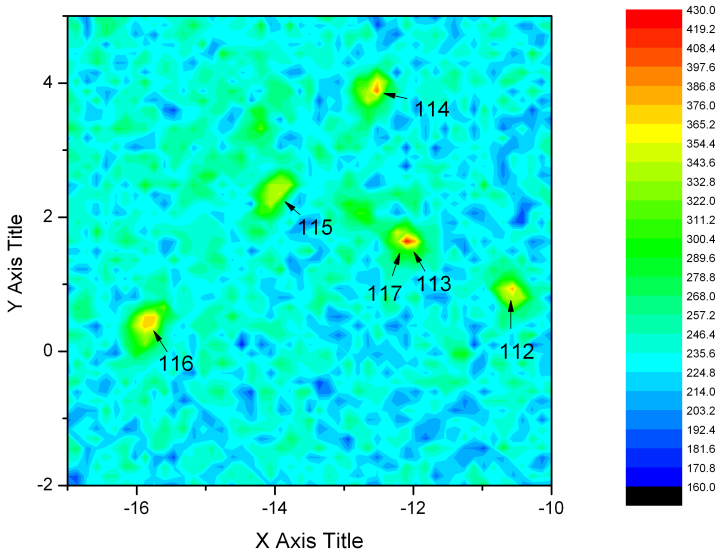

Figure 4.5: confocal image of a close up of region

.

4.3 NV^-/NV^0 ratio

Once the imaging capabilities of the microscope have been stabilised, we have been able to look for single NV centres. Pointing the microscope at a single NV centre we have done several spectroscopic measurements of their PL emission. The spectrograph we have used is [...] with a resolution of 300 μeV = 80 GHz.

The nice stability features of the microscope allow to collect many spectra from the same emitter, and change parameters as the type and power of illumination, the method of collection etc. Moreover, extra long integration periods can be used, to obtain low noise spectra.

Several spectra have been collected from single NV centres, from different samples and at different temperatures (LHe, LN_2, and room temperature).

A systematic measurement of the ratio of the intensities of the two ZPL relative to the two charge states of the NV centre, namely the NV^0 ZPL, at about 575 nm, and the NV^- ZPL, at about 637 nm has been performed on several high purity samples. HBT measurements have been performed, to check if the defects where single emitters.

The ratio has been measured in two different samples, namely sample E601 and sample E742607-18. Both these samples are high purity monocrystalline samples of CVD diamond from Element 6. Several NVs have been observed, and the ratio value has been averaged. For sample E601 the ratio average is 21.9. For this sample the number of NVs analysed is limited, since a damage to the sample has prevented us to collect more measurements. For sample E742607-18 the ratio average is 6.7.

Here we report some examples of spectra from single NVs from both samples. In figure 4.6 we show an example of spectrum with high NV^-/NV^0 ratio, from sample E601 at 77K. In figure 4.7 there is another example of spectrum with high NV^-/NV^0 ratio, from the same sample E601, at the lower temperature of 4K. In figure 4.8 we show a spectrum from sample E742607-18, from a single NV, at the low temperature of 77K.

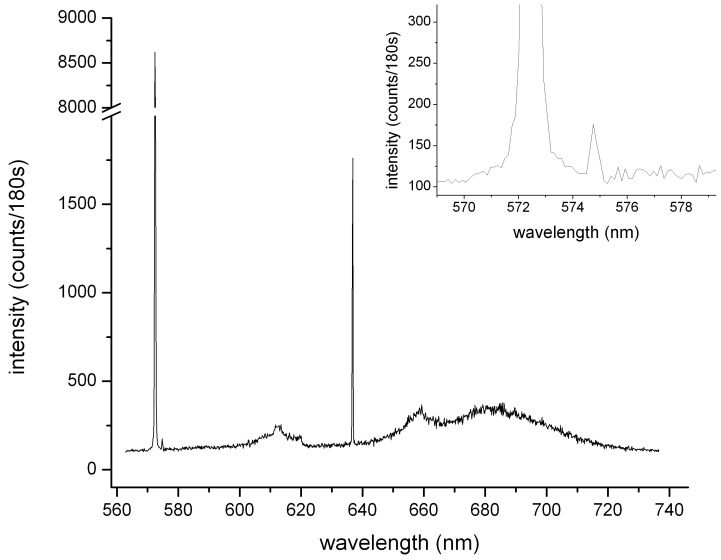

Figure 4.6: Spectrum from E601 sample, at 77K. In the inset a zoom of the same spectrum in the NV^0 ZPL range.

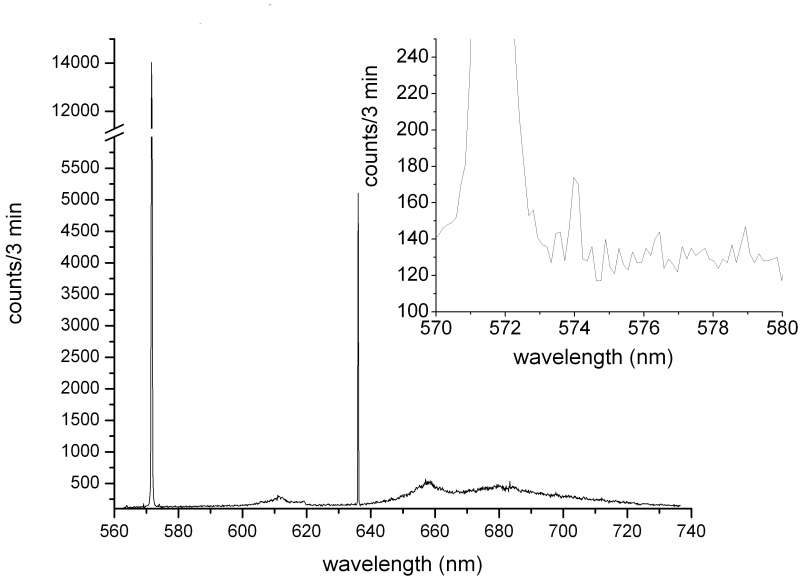

Figure 4.7: Spectrum from E601 sample, at 4K. In the inset a zoom of the same spectrum in the NV^0 ZPL range.

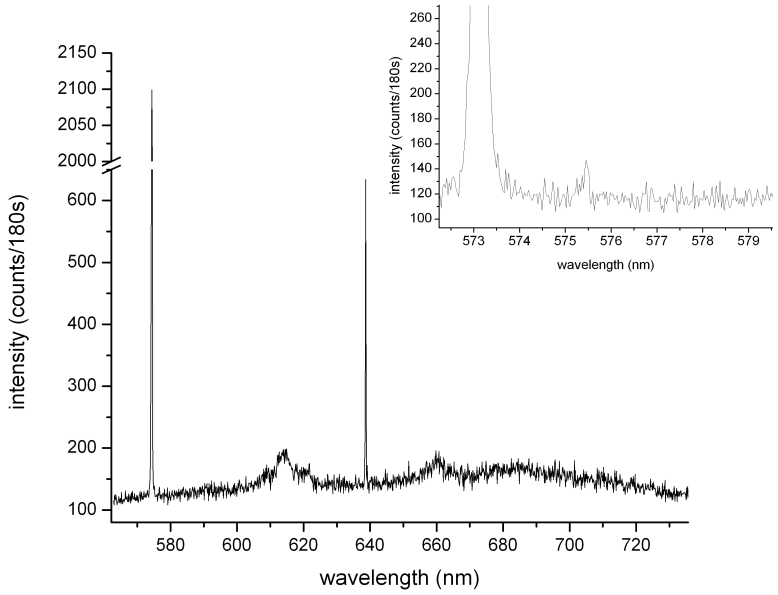

Figure 4.8: spectrum from sample E742607-18, from a single NV, at low temperature (77K). In the inset an high resolution spectrum of the NV^0 ZPL

4.4 Saturation measurements

The PL emission behaviour of an NV centre can be well predicted using a 3 levels model [KMZW00]. One of the features of this behaviour is a saturation phenomenon: the intensity of the PL emission follows linearly the excitation power up to a point where it starts to deviate from linearity.

In figure 4.9 there is a plot of the PL intensity from several single NVs in an high purity monocrystalline sample, against the excitation power. The background intensity from the surrounding crystal has been measured as well, and subtracted from the plotted data. The value of the excitation power is only proportional to the actual pover reaching the sample (it has been measured from the secondary port of the beam splitter ((7) in fig **??**)). In this figure the deviation from the linear behaviour is clearly visible, but it only starts. In figure 4.10 the excitation power reported is the total excitation power collected just before the sealed window marked (12) in figure 3.1. The fraction of this power reaching the sample can be estimated as [...]. From this estimate we can conclude that the saturation starts for an excitation power of [...] mW.

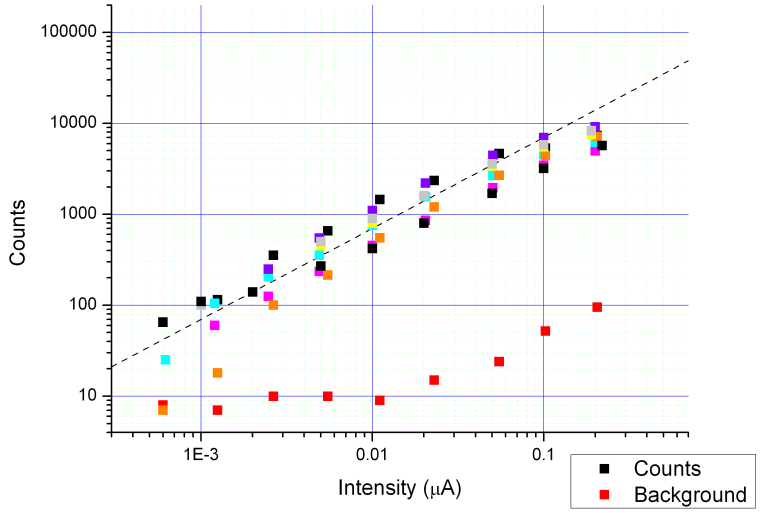

Figure 4.9: saturation curve for a group of single NVs from a monocristallyne high purity sample. In this early measurement the power reported is only proportional to the actual power reaching the sample.

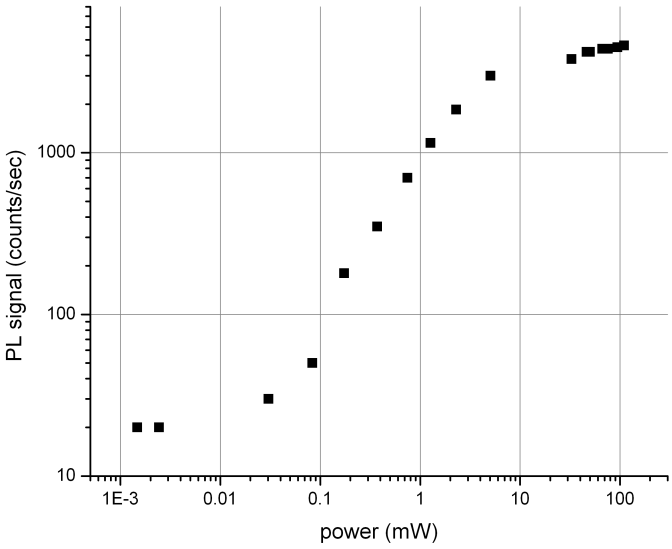

Figure 4.10: saturation curve for a single of NVs from a mono-crystalline high purity sample. The excitation power is the total power measured before the sealed window (cfr (12) in fig. 3.1). The actual excitation power reaching the NV centre is [...]

4.5 Temperature dependency

[editing note: here I want to report on the study made in the flowing cryostat to investigate the effect of temperature on the overall PL intensity. a couple of pages with a figure (int. vs temp. plot)]

4.6 Spectroscopy in polarization

As we have seen in the introduction, an interesting spectroscopic technique is that to use a polarizer in front of the collection optics, so to filter only a specific polarization direction before sending the radiation to the spectrograph. In this way it is possible to study the different polarization characters of different components of a spectrum.

This analysis is specially relevant for the the case when, in highly strained regions, the ZPL peak of the NV^- PL emission at 637 nm is split in two peaks, since we have seen from the modelling (cfr section 2.3) that the two excited orbital sublevels emit perpendicularly polarised photons.

To perform such measurements, we have chosen the high strained area in sample E742607-18 (cfr. section 4.1). Since at room temperature the ZPLis broadened, and sunk in the phonon assisted emission band, we have conducted these measurements at low temperature, using liquid nitrogen as cryogenic fluid (77K). As for other single-centre measurements, the first step has been to record confocal images, so to find a suitable area in the sample, with a promising group of centres. Once found an area with enough point-like features, we have checked that the candidate centres were single centres,

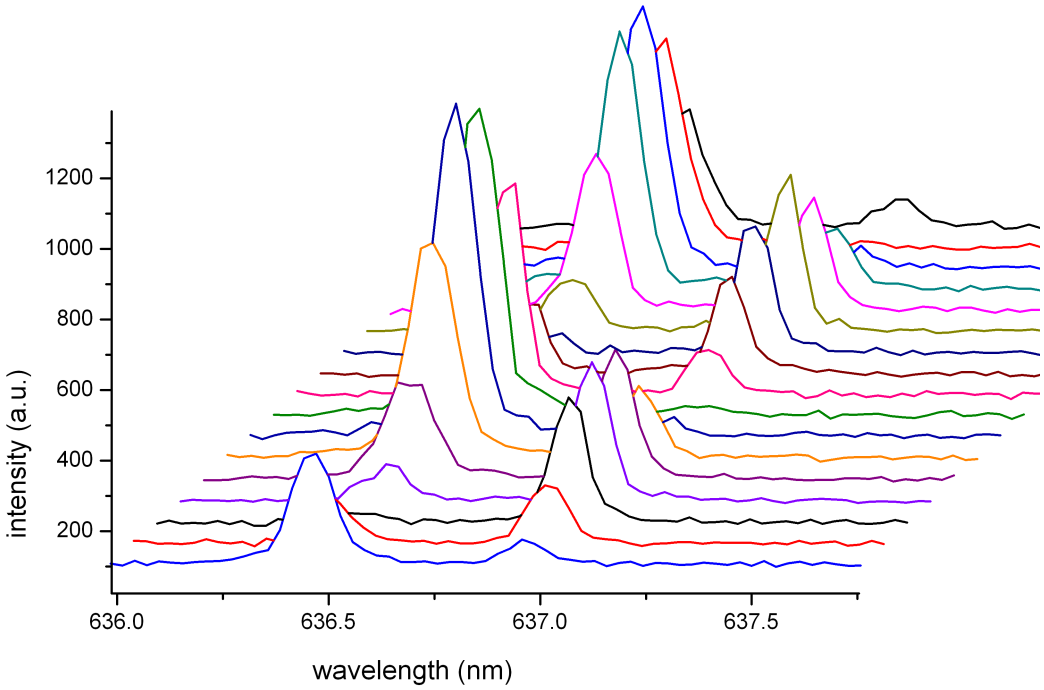

Figure 4.11: spectra of the PL emission for all the positions of the polariser

either with Hambury-Brown and Twiss measurements (cfr. section 3.3) or estimating the intensity of the photoluminescence emission. Once the right single NV centre has been found, the collected photoluminescence can be sent to the spectrograph: for each NV we have recorded an high resolution spectrum of the NV^- zero phonon line split peaks, with no polariser in front of the collection optics, and then a set of several high resolution spectra each for a different position of the polarizer in front of the collection optics. In figure 4.11 we report a plot of several low-temperature, high-resolution spectra from the same NV, with different directions of the polariser.

4.6.1 Choice of the fitting function

To estimate the intensity of each peak in the spectral plots we need to perform a best fit regression of the experimental data against an analytic function.

Te function of choice depends on the nature of the physical process that give rise to the photons emission, and the choice is restricted to the following:

- a gaussian function is used if the major source of broadening is an inhomogeneous mechanism
- a lorentian function is used if the major source of broadening is an homogeneous mechanism
- sinc function is used if the major limiting factor for the resolution is the resolution of the spectrograph

To decide which fitting function to use, we have performed several attempts, fitting several peaks with all the three candidate functions, and looking for the fits that in comparison with others was giving the smallest χ^2.

After a statistical evaluation, the best fitting function for the peaks in the spectra has been individuated as the gaussian function. This indicates that an inhomogeneous broadening is the most important mechanism that contribute to the linewidth.

[editing note: here I could add some quantitative data, possibly with a table with χ^2 values.

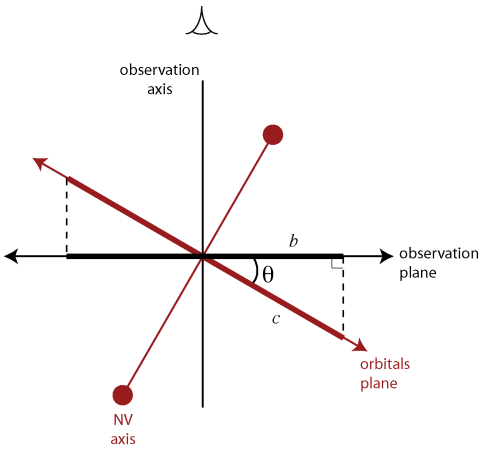

(a) orbitals plane, observation plane and NV axis

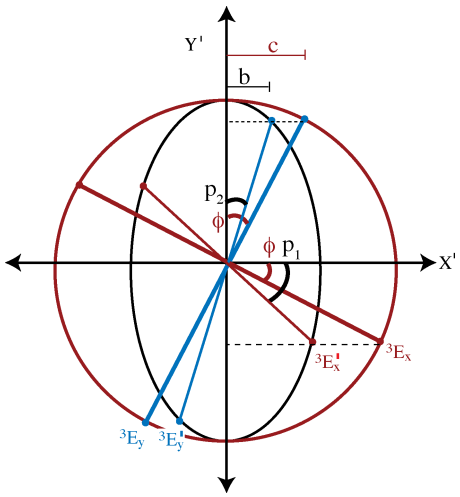

(b) orbitals plane and the orbitals ellipse

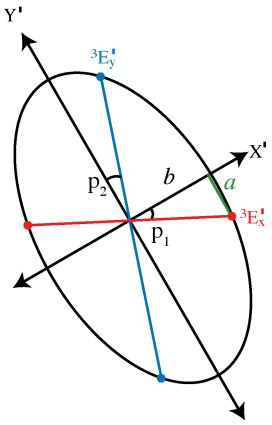

(c) the orbitals ellipse

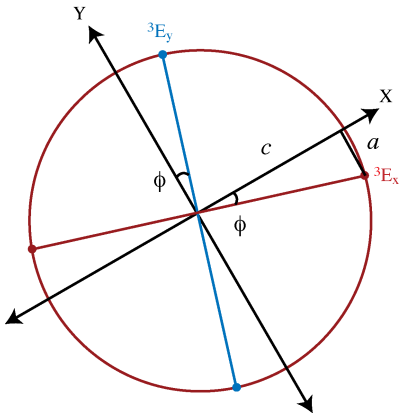

(d) the orbitals plane and the orbitals

Figure 4.12: (a) a sketch of the orbitals plane and the observation plane projected on the (X', Z') plane, i.e observed along Y'. The angle θ between them, and the projection of an orbital on the observation plane are also reported. (b) a sketch of the orbitals plane, as seen along the NV axis, and the orbitals ellipse, i.e. the projection of the orbitals plane on the observation plane. $\vec{E}_x$ and $\vec{E}_y$ are the orbitals axes (lying in the orbitals plane) while $\vec{E'}_x$ and $\vec{E'}_y$ are their projections on the observation plane. Since the transformation that brings the orbitals plane to coincide with the observation plane is a rotation around the Y' axis, the components along Y' of $\vec{E}_x$ and $\vec{E'}_x$ are equal, as well as the components of $\vec{E}_y$ and $\vec{E'}_y$, as indicated by the dotted lines. The axis Y' is the axis in common between the orbitals plane and the observation plane. (c) The orbitals ellipse alone, i.e. the projection of the orbitals plane on the observation plane. (d) The orbitals plane as seen along the NV axis.

4.6.2 Intensity modulation and polarization direction

A specific type of measurement we have done with the polarization spectroscopy has been the estimate of the direction of the ${}^3E_x$ and ${}^3E_y$ orbitals of single centres. Here we describe the steps and the details of the measurement. At the core of this measurement is the measure of the PL intensity emitted by each of the two orbitals separately, and the variation of this intensity with respect to the position of a polariser put in front of the collection optics. Within this (sinusoidal) variation, we have estimated the position of the polariser for which the collected intensity was maximal. In this way, we can indirectly measure the direction of the orbitals. To do this, we first perform a fit of each of the high resolution spectra, to estimate the intensity of the emission from each orbital (area under the peak). Then, we plot the intensities against the angle of the polariser (each high resolution spectrum has been collected through the polariser in a different position), and we fit these intensities modulations with a sine function.

In figure 4.13 we can see a modulation plot, with the sinusoidal fit, for both peaks.

In figure 4.14 we can see a similar plot in polar representation, which is more effective in representing the geometrical directions.

From the maxima of the polarizer's modulation of the collected intensity we have the angular position of the projections of the orbitals axes on the collection plane (taking into account that the orbitals act as electric dipoles, and the linear polarised light they emit is parallel to their axis). To calculate the actual positions of the orbitals in the orbitals plane, we have to take into

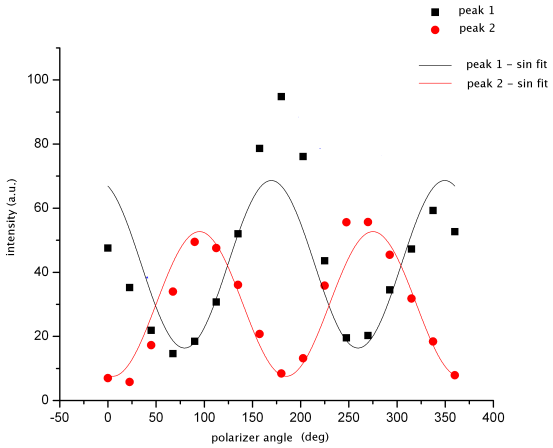

Figure 4.13: modulation plot of intensities vs angular position of the polariser

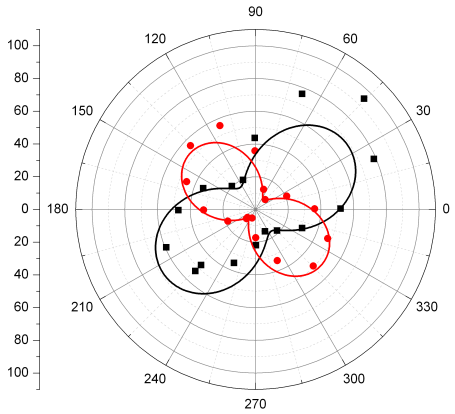

Figure 4.14: modulation plot in polar representation

account the geometry of the NV, and the position of the crystal lattice with respect to the microscope.

In figure 4.12(c) we have a sketch of the orbitals projected on the observation plane, and what we have called *the orbitals ellipse*, i.e. the projection, on the observation plane, of the circle that represents the orbitals plane. This figure represents the direction of the orbitals, as they are seen along the observation direction.

In appendix B.1 we report details of the trigonometric calculations to recover the directions of the orbitals in the orbitals plane.

4.6.3 Projections of the orbitals and the minimal angle

To compare the experimental measurements with the theoretical model we have developed a first test. We have estimated, either with numerical Monte Carlo methods and with direct trigonometric calculations, the minimal possible angle that the model would allow between the two projections of the orbitals axes on the observation plane. This minimal angle is 60.

All the experimental data collected comply with this theoretical prediction. The fact that the experimental data are compatible with this theoretical detail have encouraged us to perform more measurements and to further analyse the data.

4.6.4 Total emission and NV orientation

Another measurement we have devised, using the polarisation spectroscopy, is the estimate of the NV axis direction. As we have seen in section 2.3.3,

when we observe the NV in the crystal, we have four possible orientations of the axis. But only two orientations of the orbitals ellipse correspond to these four orientations of the NV axis, as can be seen in figure 2.6. So, our measurement will not be able to completely determine the NV axis direction, but only restrict it to two possibilities.

The total intensity has been calculated analytically, starting fro the fitting sinusoidal functions of the two modulation datasets from the two single peaks of PL emission the two orbitals. Is possible to demonstrate that the total collected intensity is maximal when the polariser is aligned to a direction not far from the major axis of the orbitals ellipse; here we only give a qualitative and intuitive argument.

Since the intensity collected from an orbital is maximal when the orbital axis is parallel to the observation plane (think about the electric field) and since the orbitals plane and the observation plane intersect in the orbitals ellipse major axis, is intuitive to understand that for each orbital, the closer it is to the ellipse major axis, the higher is the intensity collected from it. Is important to stress that this is based on the hypothesis that the intensity *emitted* by each orbital is the same. Then, this give also an intuitive reason why if we sum the two collected intensities, and consider its sinusoidal modulation, the maxima fall near to the major axis of the orbitals ellipse. We will call tis angular direction the *total intensity polarisation direction*.

So, the NV axis direction estimate consists in plotting the total intensity, and find the maxima of its sinusoidal fit.

Then, looking at the outcome from several NVs is possible to discriminate between the two possible orientations of the crystal lattice within the sample

(i.e. how the sample is cut with respect to the lattice). Once the crystal's orientation is known, the two possible directions of the ellipses major axes will be known as well, and since they are perpendicular, it's easy to assign each NV to one of the two possible groups of axis directions.

4.7 Polycrystalline samples

In this section we report about two polycrystalline samples. We show confocal images and spectra.

4.7.1 Sample E948439-02

In figure 4.15 we show a confocal image where the bounduary between two grains with different crystal orientations is clearly visible.

In image 4.16 another confocal image, and in figure 4.17 a close-up from the same area, where an NV is highlighted. In figure 4.18 we report a spectrum from the NV highlighted, with in the inset an high resolution spectrum of the NV^- ZPL. We have observed the same multiple splitting of the ZPL present in this spectrum in most of the single NVs from this sample, specially if close to a grain boundary.

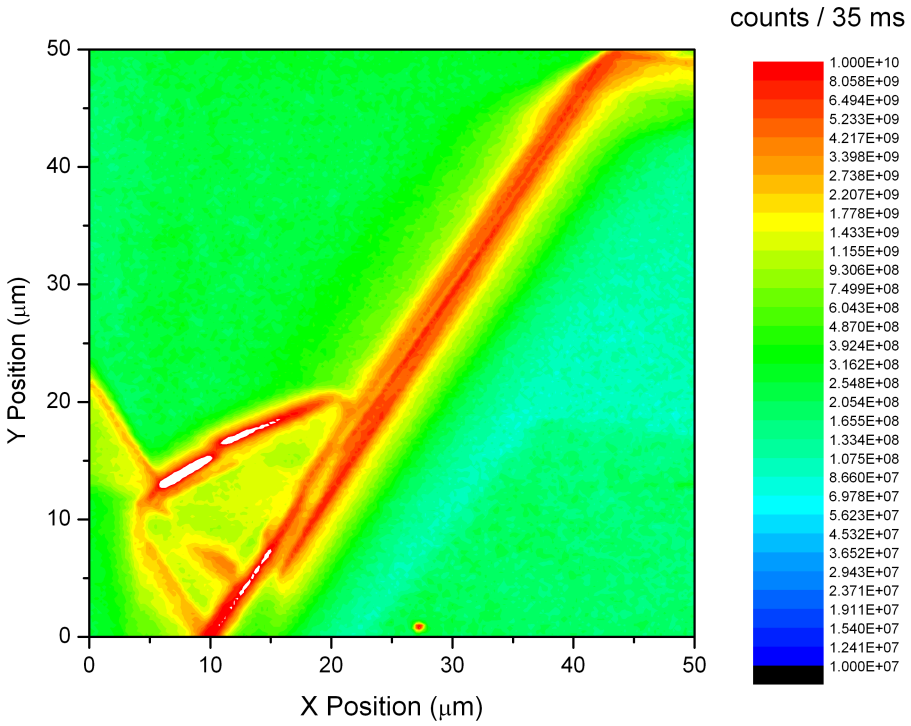

Figure 4.15: confocal image from sample E948439-02

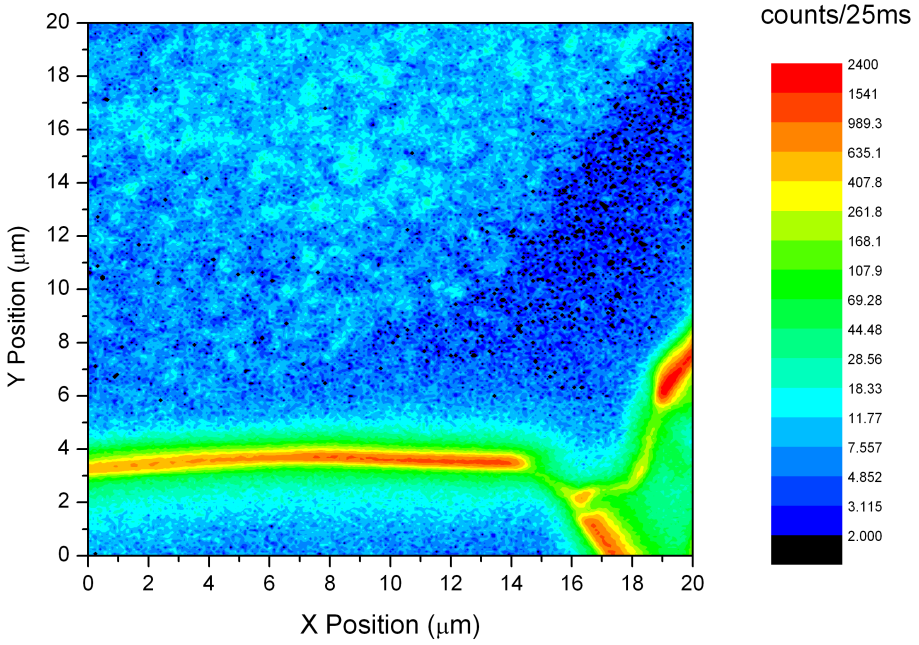

Figure 4.16: confocal image from sample E948439-02

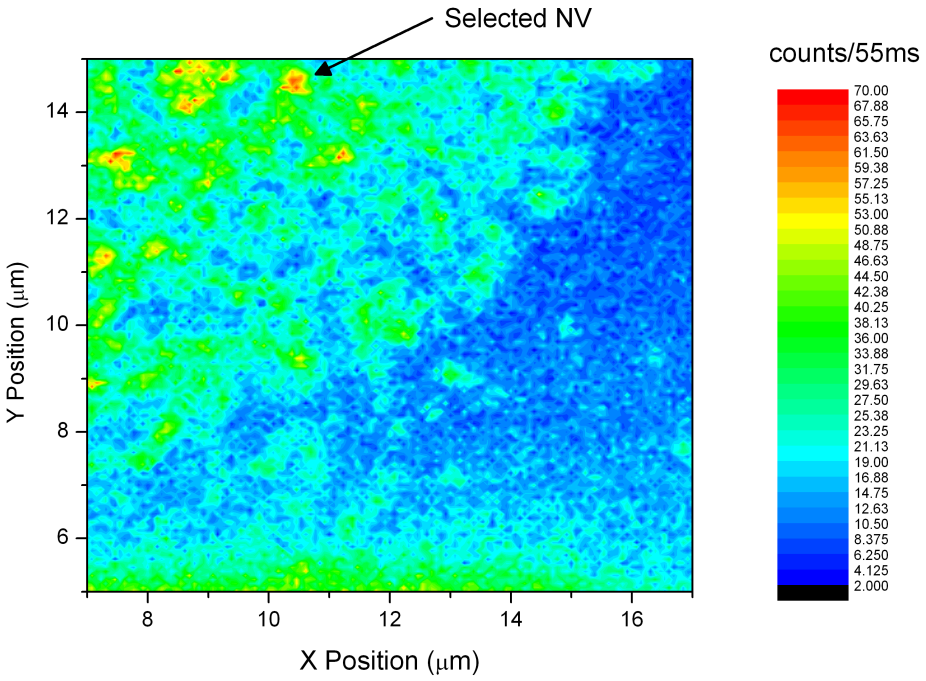

Figure 4.17: confocal image from sample E948439-02

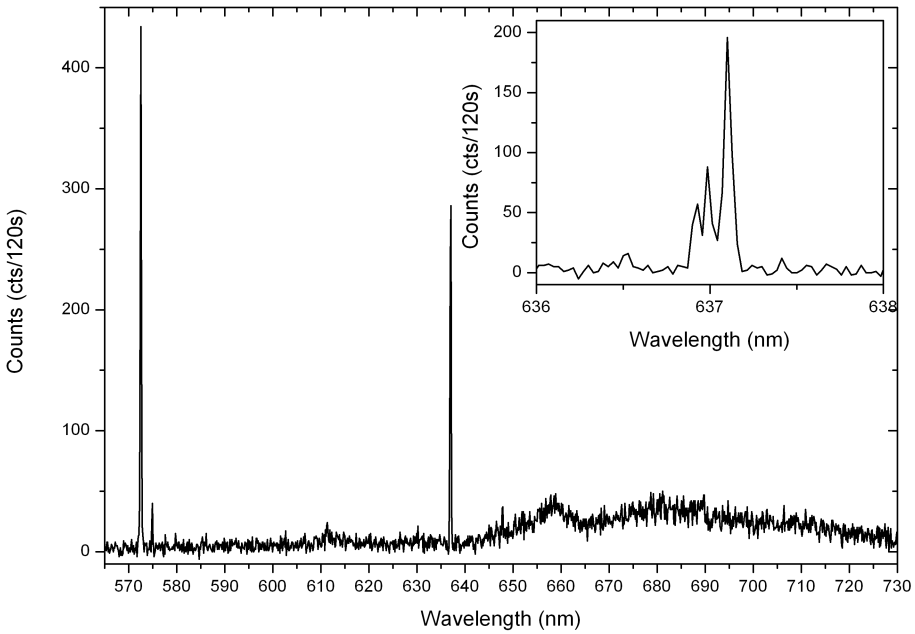

Figure 4.18: spectra from the NV highlighted in the previous confocal image (4.17). In the inset an high resolution spectrum of the NV^- ZPL

4.7.2 Sample poly01

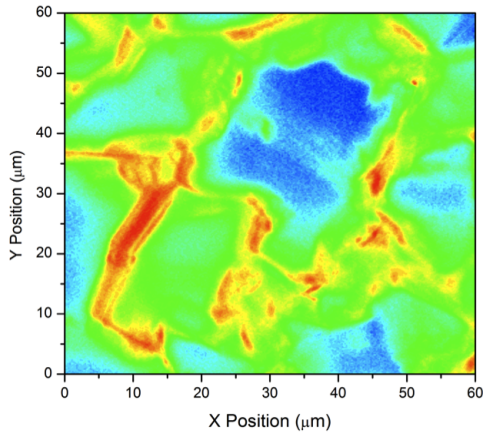

Figure 4.19: confocal image from sample poly01

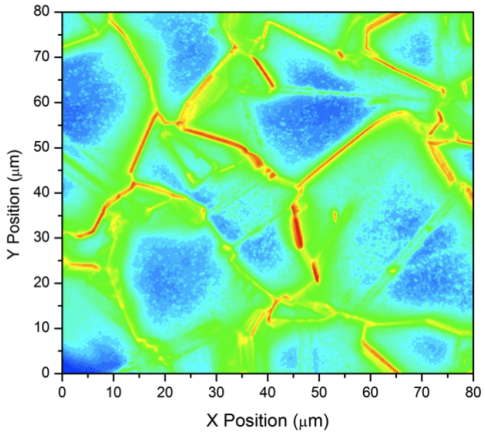

Figure 4.20: confocal image from sample poly01

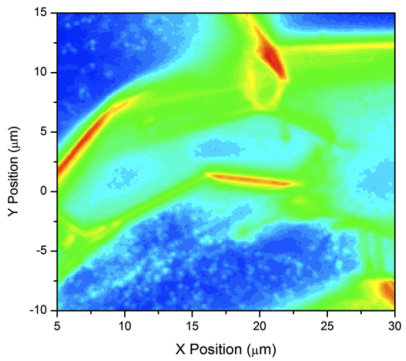

Figure 4.21: confocal image from sample poly01

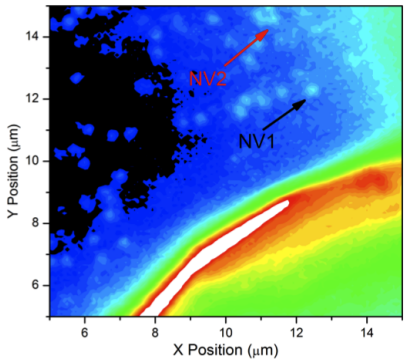

Figure 4.22: confocal image from sample poly01

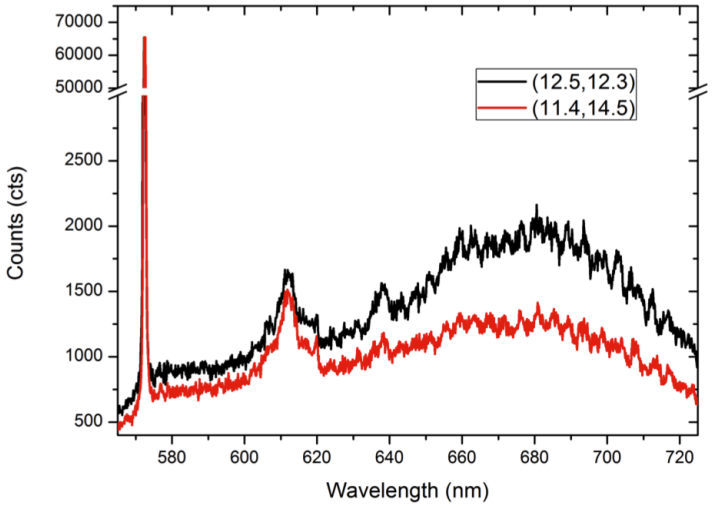

Figure 4.23: spectra from sample poly1

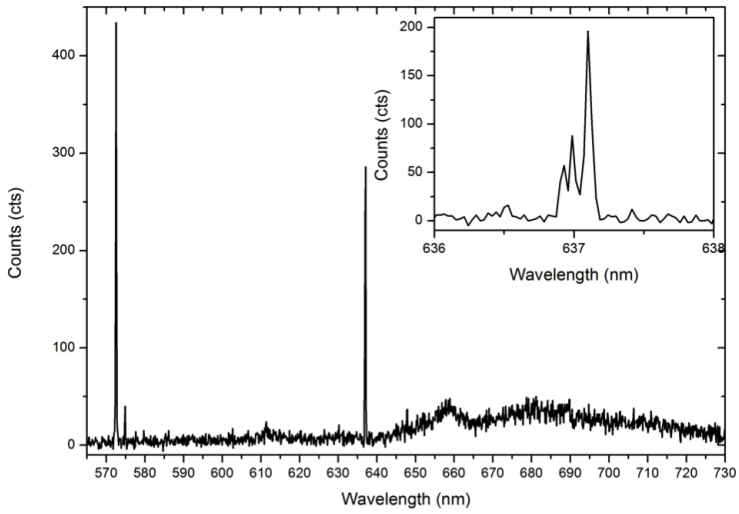

Figure 4.24: spectra from sample E948439-02

[...]

4.8 Oxons

[editing note: section describing the anomalous features we called oxons. 2 or 3 pages, with a confocal image and a spectrum]

Chapter 5

Calculating the stress tensor

In this chapter we illustrate a measurement technique we devised to measure the local stress tensor in highly strained regions of high purity diamond samples, using polarization spectroscopy of single NV centres. This technique uses the polarisation spectroscopy measurements described in section 4.6 of the previous chapter. We also use the conclusions about the total intensity polarisation direction reached in section 4.6.4.

[...]

5.1 Calculation strategy

5.1.1 Inverting the system of equations

We base our calculations for the stress tensor on piezospectroscopic equation 2.11 which we copy here for convenience of the reader:

$$\begin{cases} \alpha = A_1 (\sigma_{xx} + \sigma_{yy} + \sigma_{zz}) + 2A_2 (\sigma_{yz} + \sigma_{zx} + \sigma_{xy}) \\ \beta = B (2\sigma_{zz} - \sigma_{xx} - \sigma_{yy}) + C (2\sigma_{xy} - \sigma_{yz} - \sigma_{zx}) \quad \text{(copy of eq. 2.11)} \\ \gamma = \sqrt{3}B (\sigma_{xx} - \sigma_{yy}) + \sqrt{3}C (\sigma_{yz} - \sigma_{zx}) . \end{cases}$$

As said in section 2.4, this system of equations relates the stress tensor components to the parameters α, β and γ, which contain the information about the spectral effects of the stress (shift and splitting of the ZPL) as well as the geometrical information about the position of the orbitals (angle between the orbital and the principal axis). We want to invert this system and calculate the stress tensor components, knowing the spectral information of α, β and γ. If we invert 2.11 we obtain a system of 3 equations in the 6 unknowns which represent the 6 non coincident components of the 3×3 symmetric stress tensor.

We choose a group of at least 4 NVs close to each other, so to allow the hypothesis that the stress is the same for all of them. Then we choose all the possible groups of 3 NVs out of this group of 4. For each group we write all the possible systems of 9 equations. In choosing the possible systems of equations means choose for each NV the direction of the axis. Here, for each NV we can choose between the two possible directions allowed by the informations that we have from the "total intensity maxima" (cfr section 4.6.4). With these restrictions, not all the possible groups of 3 NVs can lead to an over-determined system of equations, so a case by case analysis is needed.

The method succeeds if for a choice of the directions we have compatible

solutions for all the sub-groups of 3 NVs out of the group of close NVs. This outcome solves the two mentioned "problems", i.e. proves that the stress is uniform for the NVs, and determines their directions.

Here we prepare all the possible matrices of coefficients, for all the possible combinations of directions of the NVs.

3×6 matrices

In this section we write the coefficient matrices for the 4 systems of equations obtained inverting the 4 piezo-spectroscopic equations 2.11 - 2.14, and labelled using the convention set in table 2.1 of section 2.3.1:

$\mathbf{a} = [111]$

$$\begin{pmatrix} A_1 & A_1 & A_1 & 2A_2 & 2A_2 & 2A_2 \\ -B & -B & 2B & -C & -C & 2C \\ \sqrt{3}B & -\sqrt{3}B & 0 & \sqrt{3}C & -\sqrt{3}C & 0 \end{pmatrix} \tag{5.1}$$

$\mathbf{b} = [\bar{1}11]$

$$\begin{pmatrix} A_1 & A_1 & A_1 & 2A_2 & -2A_2 & -2A_2 \\ -B & -B & 2B & -C & C & -2C \\ -\sqrt{3}B & \sqrt{3}B & 0 & -\sqrt{3}C & -\sqrt{3}C & 0 \end{pmatrix} \tag{5.2}$$

$\mathbf{c} = \ [\bar{1}\bar{1}1] = [11\bar{1}]$

$$\begin{pmatrix} A_1 & A_1 & A_1 & -2A_2 & -2A_2 & 2A_2 \\ -B & -B & 2B & C & C & 2C \\ \sqrt{3}B & -\sqrt{3}B & 0 & -\sqrt{3}C & \sqrt{3}C & 0 \end{pmatrix} \tag{5.3}$$

$\mathbf{d} = \ [1\bar{1}1]$

$$\begin{pmatrix} A_1 & A_1 & A_1 & -2A_2 & 2A_2 & -2A_2 \\ -B & -B & 2B & C & -C & -2C \\ -\sqrt{3}B & \sqrt{3}B & 0 & \sqrt{3}C & \sqrt{3}C & 0 \end{pmatrix} \tag{5.4}$$

9×6 **matrices**

As said in section 5.2 we choose at least 3 groups of 3 equations to build systems of 9 equations. Choosing among 4 different systems of 3 equations, we can build $\frac{4!}{3!(4-3)!} = 4$ systems of 9 equations.

we have the following possibilities: $\{a, b, c\}\{a, b, d\}\{a, c, d\}\{b, c, d\}$.

Here we write the explicit matrices of coefficients for each choice:

$\{a, b, c\}$

$$\begin{pmatrix} A_1 & A_1 & A_1 & 2A_2 & 2A_2 & 2A_2 \\ -B & -B & 2B & -C & -C & 2C \\ \sqrt{3}B & -\sqrt{3}B & 0 & \sqrt{3}C & -\sqrt{3}C & 0 \\ A_1 & A_1 & A_1 & 2A_2 & -2A_2 & -2A_2 \\ -B & -B & 2B & -C & C & -2C \\ -\sqrt{3}B & \sqrt{3}B & 0 & -\sqrt{3}C & -\sqrt{3}C & 0 \\ A_1 & A_1 & A_1 & -2A_2 & -2A_2 & 2A_2 \\ -B & -B & 2B & C & C & 2C \\ \sqrt{3}B & -\sqrt{3}B & 0 & -\sqrt{3}C & \sqrt{3}C & 0 \end{pmatrix} \tag{5.5}$$

$\{a, b, d\}$

$$\begin{pmatrix} A_1 & A_1 & A_1 & 2A_2 & 2A_2 & 2A_2 \\ -B & -B & 2B & -C & -C & 2C \\ \sqrt{3}B & -\sqrt{3}B & 0 & \sqrt{3}C & -\sqrt{3}C & 0 \\ A_1 & A_1 & A_1 & 2A_2 & -2A_2 & -2A_2 \\ -B & -B & 2B & -C & C & -2C \\ -\sqrt{3}B & \sqrt{3}B & 0 & -\sqrt{3}C & -\sqrt{3}C & 0 \\ A_1 & A_1 & A_1 & -2A_2 & 2A_2 & -2A_2 \\ -B & -B & 2B & C & -C & -2C \\ -\sqrt{3}B & \sqrt{3}B & 0 & \sqrt{3}C & \sqrt{3}C & 0 \end{pmatrix} \tag{5.6}$$

$\{a, c, d\}$

$$\begin{pmatrix} A_1 & A_1 & A_1 & 2A_2 & 2A_2 & 2A_2 \\ -B & -B & 2B & -C & -C & 2C \\ \sqrt{3}B & -\sqrt{3}B & 0 & \sqrt{3}C & -\sqrt{3}C & 0 \\ A_1 & A_1 & A_1 & -2A_2 & -2A_2 & 2A_2 \\ -B & -B & 2B & C & C & 2C \\ \sqrt{3}B & -\sqrt{3}B & 0 & -\sqrt{3}C & \sqrt{3}C & 0 \\ A_1 & A_1 & A_1 & -2A_2 & 2A_2 & -2A_2 \\ -B & -B & 2B & C & -C & -2C \\ -\sqrt{3}B & \sqrt{3}B & 0 & \sqrt{3}C & \sqrt{3}C & 0 \end{pmatrix} \tag{5.7}$$

$\{b, c, d\}$

$$\begin{pmatrix} A_1 & A_1 & A_1 & 2A_2 & -2A_2 & -2A_2 \\ -B & -B & 2B & -C & C & -2C \\ -\sqrt{3}B & \sqrt{3}B & 0 & -\sqrt{3}C & -\sqrt{3}C & 0 \\ A_1 & A_1 & A_1 & -2A_2 & -2A_2 & 2A_2 \\ -B & -B & 2B & C & C & 2C \\ \sqrt{3}B & -\sqrt{3}B & 0 & -\sqrt{3}C & \sqrt{3}C & 0 \\ A_1 & A_1 & A_1 & -2A_2 & 2A_2 & -2A_2 \\ -B & -B & 2B & C & -C & -2C \\ -\sqrt{3}B & \sqrt{3}B & 0 & \sqrt{3}C & \sqrt{3}C & 0 \end{pmatrix}. \tag{5.8}$$

5.1.2 Solution for an over-determined system of linear equations

Here we give some details on the criteria to choose the best approximation to a solution for an over-determined system of linear equations, using the Moore-Penrose pseudo-inverse matrix approach [Pen55, PT56]. [...]

From the plots in figure **??** we can infer the following orientations for the NVs:

NV	direction	axis vector
106b, 111	$\leftrightarrow$	$[\bar{1}11]$ or $[1\bar{1}1]$
105b, 107b, 108 109, 110	$\updownarrow$	$[111]$ or $[11\bar{1}]$

Once we have this information, we can extract from the experimental data the angle p_2 for each NV. We remember that the angle p_2 is defined as the angle between the principal axis Y' and the closest of the two orbitals axes projected on the observation plane (cfr figure 4.12(b)). We then apply the trigonometrical calculations described in section **??** (cfr equation **??**), so to have for each NV the angle ϕ. In table **??** we report the numerical values for the NVs in region 3.

Table 5.1: experimental data referred to the sample edges

NV	p_2 (deg)	ϕ (deg)
[...]		

Now, using the relations found in section 2.4.3 (cfr equation 2.15), we obtain the values of β and γ from the values of ϕ and the splitting:

NV	ϕ (deg)	splitting (nm)	β	γ
[...]				

5.2 Calculaitons

Here we face the task of solving equations (2.11) and the others in other directions.

As we have seen in section 2.3, we have 4 different possible orientations of the NV with respect to the crystal lattice reference, and for each of these there are three equations that express the relationship between α, β andγ, and the components of the 3D stress tensor σ_{ij}. Since the stress tensor is symmetric, the unknown components are only 6. So, to be able to solve a system of linear equations, we need at least 6 linearly independent equations. So, a first approach to calculate the 3D stress tensor would be to to look for two NVs close to each other (so that the hypothesis that the stress is the same for both is a sensible one), and with different orientations of the axes, and then write the three equations for each of them, so to obtain a solvable system of equations. It turns out that if we choose two systems of 3 equations, relative to two different directions, no matter which two directions we choose, among the corresponding 6 equations only 5 of them are linearly independent. This means that to be able to solve a system and find the 6 unknown components of the stress tensor we need at least 3 NVs close to each other and with 3 different directions, and solve an over-determined system of 9 equations in 6 unknowns.

5.3 Results

In this section we describe the application of the method described in the theoretical section 5.1 on the experimental data, and its results.

5.3.1 Calculations of intermediate parameters

[editing note: in this section I want to report some data tables with the calculated values for some relevant angles and parameters as α, β andγ

5.3.2 Numerical values for α β and γ

Table 5.2: experimental data referred to the sample edges

NV	α	β	γ
[...]			

5.3.3 Results for the stress tensor components

In this section we report the calculated values for the stress tensor, using the data relative to set # 4 of NVs, which appear in the confocal image in figure A.3 in appendix A.1.

We can calculate the stress tensor components choosing a group of at least 3 NVs, and specifying the direction for each of them. For each NV the direction is chosen between the two allowed by the observed projection direction (cfr figure A.9 in section A.2).

Moreover, we can use a quantitative method to assess how similar or different are two of these results, obtained with different NVs, or with different choices

of the directions. If we consider the 6 different stress tensor components as the components of a 6-dimensional vector, we can calculate the euclidean distance between two results

$$\sqrt{(\sigma^a_{xx} - \sigma^b_{xx})^2 + (\sigma^a_{yy} - \sigma^b_{yy})^2 + (\sigma^a_{zz} - \sigma^b_{zz})^2 + (\sigma^a_{yz} - \sigma^b_{yz})^2 + (\sigma^a_{xz} - \sigma^b_{xz})^2 + (\sigma^a_{xy} - \sigma^b_{xy})^2}. \tag{5.9}$$

So, for each row of the following tables we have two groups of NVs (3 or more) with the direction of each specified by a lowercase letter (as in the usual convention shown in table 2.1 of section 2.3), and the two corresponding sets of numerical values for the stress tensor components. In each row, for each couple of NV groups and stress results, we have also the euclidean distance 5.9.

Table 5.3: set #4 - NVs # 105b, 106b, 107b, 108, 109, 110, 111 - stress tensor components (expressed in Pa) - groups of 3 NVs, with directions (cfr. table 2.1), ordered as $\sigma_{xx}, \sigma_{yy}, \sigma_{zz}, \sigma_{yz}, \sigma_{xz}, \sigma_{xy}$

groups of NVs, with stress tensor components	euclidean distance
105b - c, 107b - a, 106b - d 105b - c, 107b - a, 111 - d -0.511,0.369,0.683,-0.007,0.007,0.143 -0.472,0.358,0.747,0.002,-0.007,0.123	row 1 0.0806
105b - c, 108 - a, 106b - d 105b - c, 108 - a, 111 - d -0.516,0.409,0.665,-0.006,0.020,0.151 -0.476,0.398,0.730,0.003,0.007,0.131	row 2 0.0806
105b - c, 107b - a, 106b - d 105b - c, 108 - a, 106b - d -0.511,0.369,0.683,-0.007,0.007,0.143 -0.516,0.409,0.665,-0.006,0.020,0.151	row 3 0.0465
105b - c, 107b - a, 106b - d 105b - c, 109 - a, 111 - d -0.511,0.369,0.683,-0.007,0.007,0.143 -0.586,0.370,0.725,-0.029,0.031,0.157	row 4 0.0926
105b - c, 108 - a, 106b - d 105b - c, 110 - a, 111 - d -0.516,0.409,0.665,-0.006,0.020,0.151 -0.422,0.321,0.675,0.003,-0.068,0.058	row 5 0.1821
105b - a, 107b - c, 106b - b 105b - c, 107b - a, 106b - d -0.511,0.369,0.683,0.007,-0.007,0.143 -0.511,0.369,0.683,-0.007,0.007,0.143	row 9 0.0200
105b - a, 107b - c, 111 - b 105b - c, 107b - a, 111 - d -0.472,0.358,0.747,-0.002,0.007,0.123 -0.472,0.358,0.747,0.002,-0.007,0.123	row 10 0.0135

5.3.4 Comments and conclusions on the results

In table 5.3 we have several groups, with similar results for the stress tensor. In row 1 we swap between NV106b and NV111, the only two NVs of the set with a projected ellipse perpendicular to the sample's edge, i.e. with possible orientations b ($[\bar{1}11]$) and d ($[1\bar{1}1]$). In row 2 we change one of the NVs with possible orientations a ($[111]$) and d ($[11\bar{1}]$). In the following rows we have chosen few other possible groups of 3 NVs, to show the range of variation of the numerical values of the stress tensor components, and of the euclidean distances.

In this table we can also notice the limits of our method: if we compare row 1 and row 7 we see that the same distance is obtained using for NV106b and NV111 two different orientations. In the same way, in row 8 we obtain a relatively small distance comparing two results from the same group where we have chosen the two possible directions for NV105b and NV107b. Finally, in row 9 we have a rather small distance using the same direction for NV105b and NV107b. These last results mean that the distance is not enough to tell which of the possible orientations is the "right one". One last observation is that, as appears in row 10, if we apply an inversion along the z axis, and swap all the directions for the NVs, we obtain the same numerical values for te stress tensor components, with the exception of the sign inversions for $\sigma_{yz}$and σ_{xz}

testing the results To test the results, is possible to use the values obtained for the stress tensor components, and use them in equation 2.11 to re-calculate the values of α, β and γ for a given NV.

In table 5.4 are reported these results, and compared with the experimental values of α, β and γ (expressed in eV).

Table 5.4: comparison of values for α, β and γ

NV	experimental	re-calculated
NV 105b		
α	1.802E-12	1.91276E-12
β	2.268E-12	2.08028E-12
γ	-1.919E-12	-1.51925E-12
NV 107b		
α	1.804E-12	1.83958E-12
β	2.242E-12	2.09634E-12
γ	-1.293E-12	-1.47069E-12
NV 111		
α	6.815E-14	-7.81913E-14
β	9.391E-13	1.27248E-12
γ	1.259E-12	1.48106E-12

Conclusions From there results, and in particular if we look at table 5.3, we can conclude that the method illustrated so far doesn't allow to draw a conclusion about the real direction of each NV among the two allowed by the polarization direction data from section **??**.

On the other hand, the method is rather successful in yielding rather narrow ranges for the values of the stress tensor components.

Appendix A

Complete data sets

A.1 Confocal images

In this section we report the confocal images of the regions in sample E742607-18 where the NVs for the stress tensor measurement discussed in chapter 5.

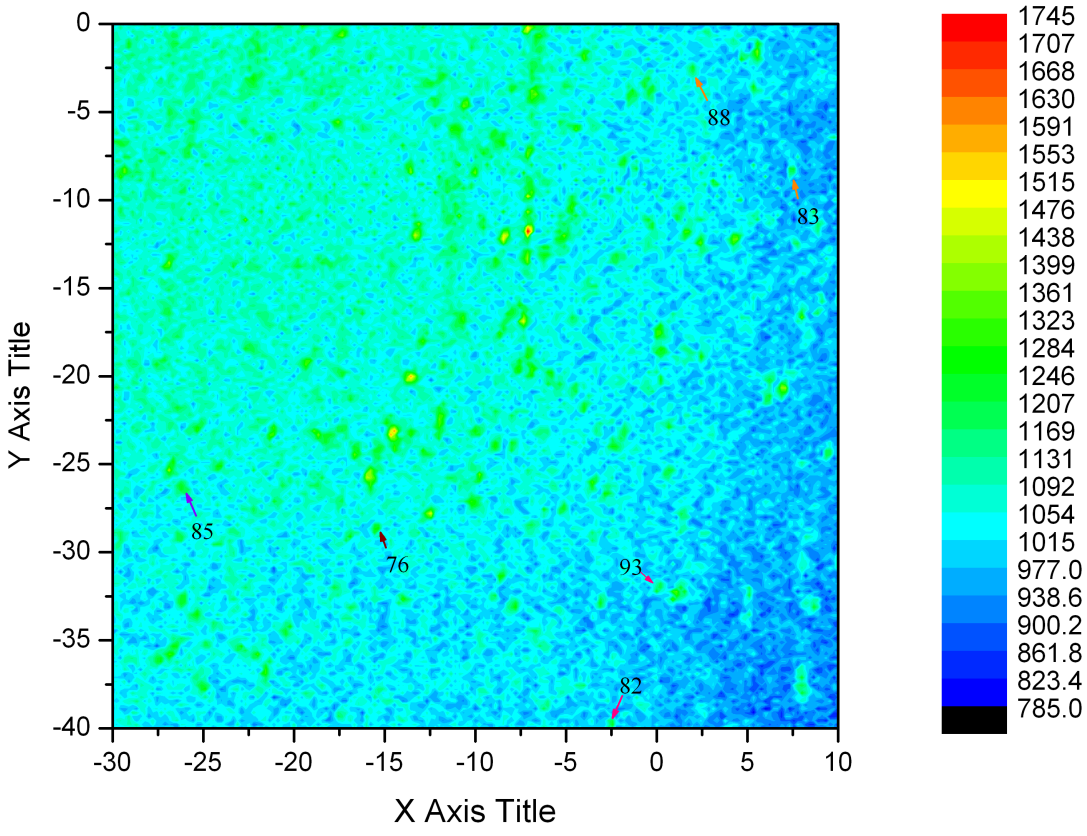

Figure A.1: confocal image for region 1

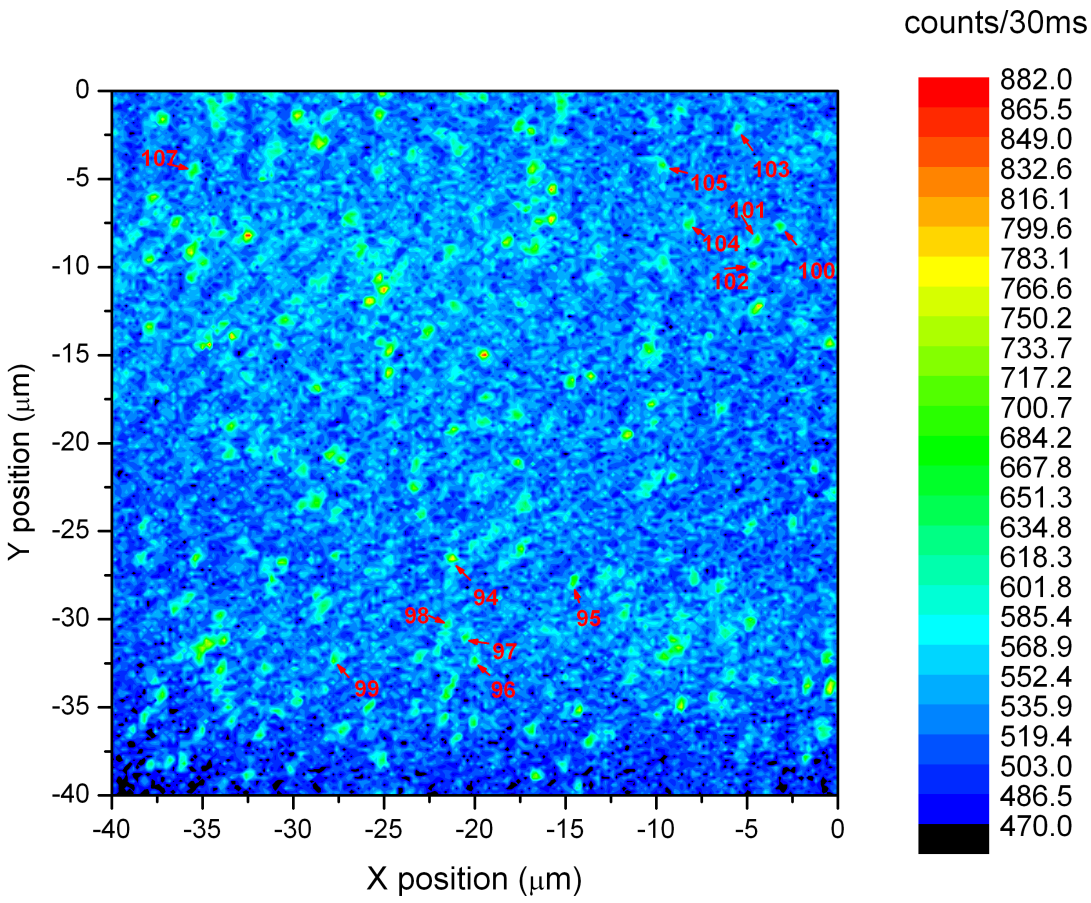

Figure A.2: confocal image for region 2, where NV 95, 96, 98, 99, 100, 101, 103, 104 and 107

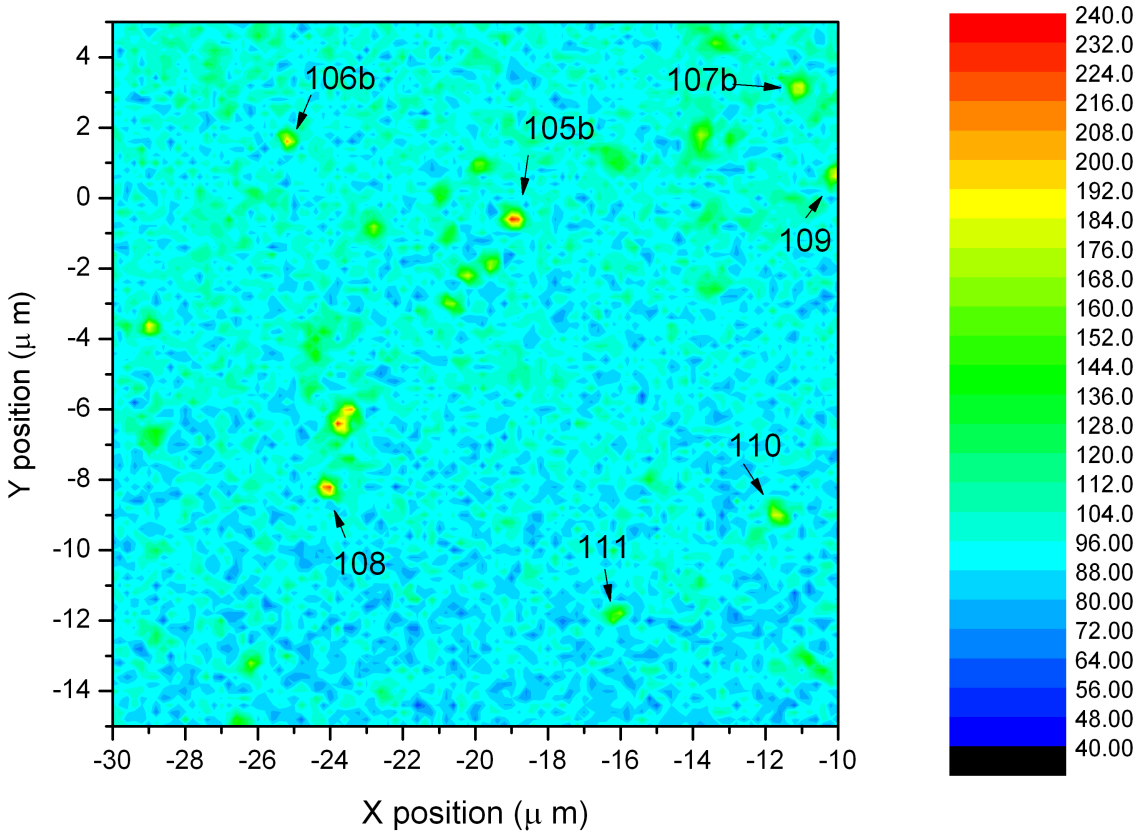

Figure A.3: confocal image for region 3, where 105bis, 106bis, 107bis, 108, 109, 110 and 111

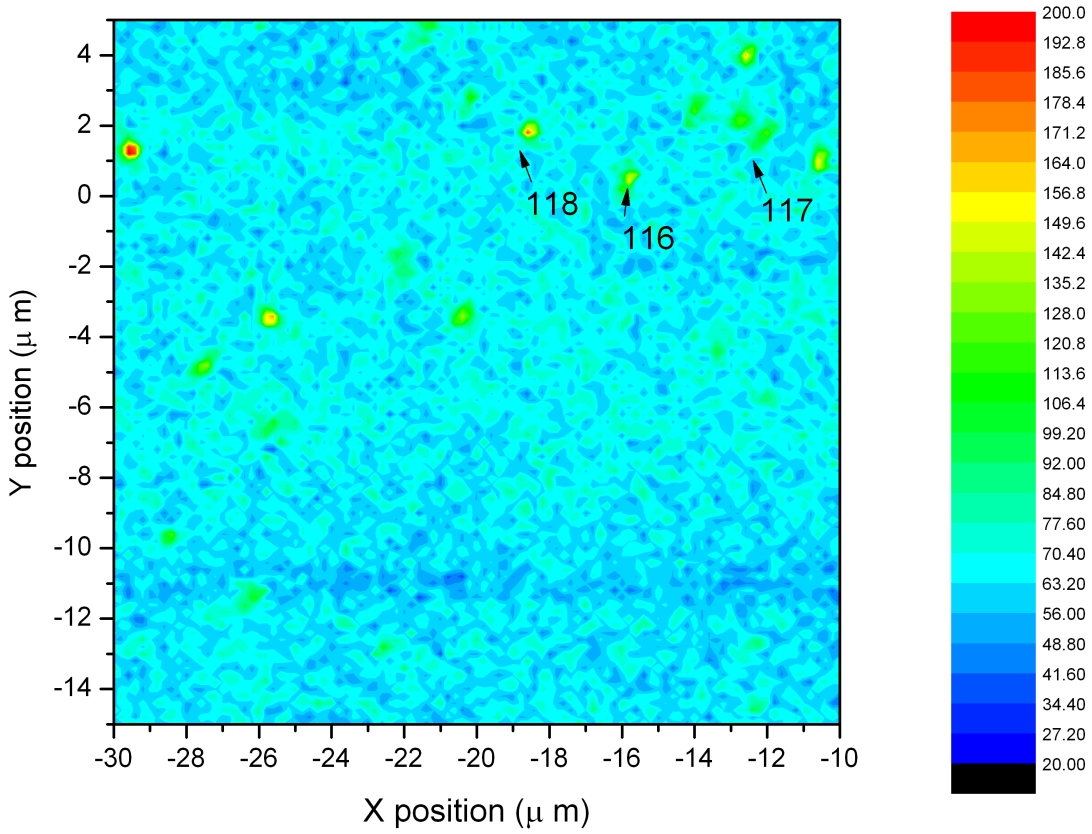

Figure A.4: confocal image for region 4, where NV 112, 113, 114, 115, 116, 117 and 118 are

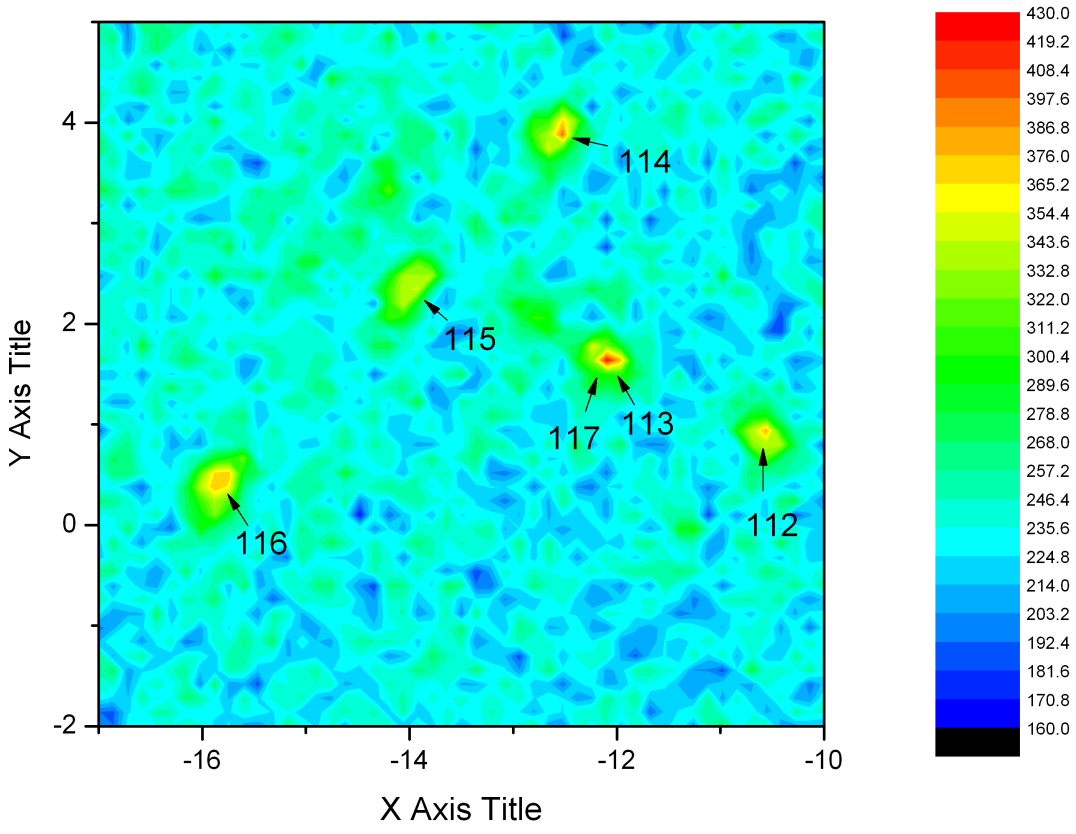

Figure A.5: confocal image of a close up of region 4, where NV 112, 113, 114, 115, 116, 117 and 118 are

A.2 Modulation plots

In this section we report the plots of the modulation of the intensity of the two peaks, with respect to the angular position of the polarizer. We have a plot for each NV, the angular coordinate is the one referred to the instrument's gauge. In the graphs is reported as a green line the angular position that has

been afterwards found to be the one parallel to sample's edge, as described in section **??**.

In each graph has been also reported, as a blue double arrow, the angular position of the maximal intensity of the modulation of the total emission, as calculated in section **??**.

The position of the total emission maximum (blue arrow) gives the information about the alignment of the NV axis.

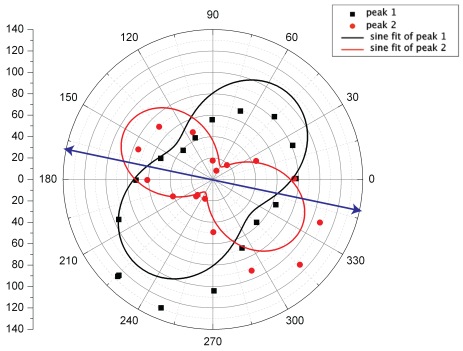

(a) NV76 (direction $\|\rightarrow (a-c)$)

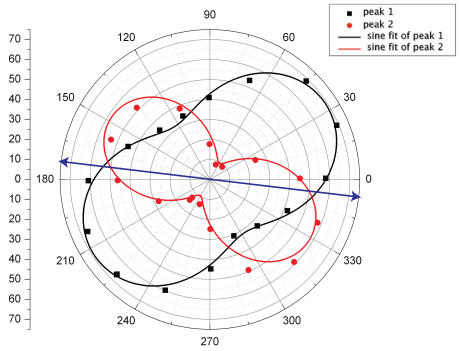

(b) NV82 (direction $\|\rightarrow (a-c)$)

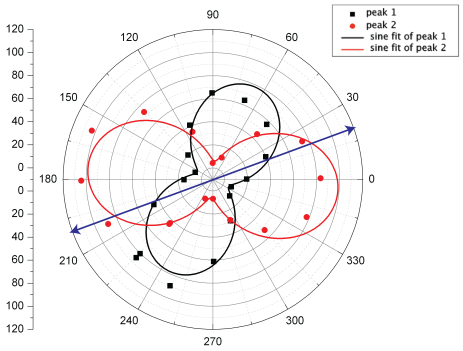

(c) NV83 (direction $\|\rightarrow (a-c)$)

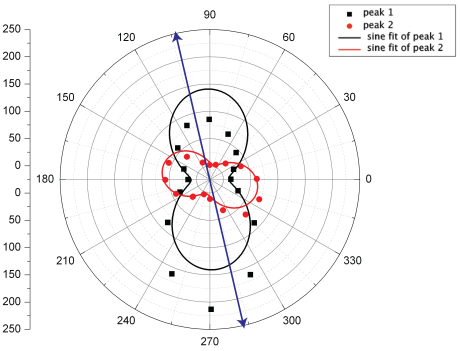

(d) NV85 (direction $\perp\rightarrow (b-d)$)

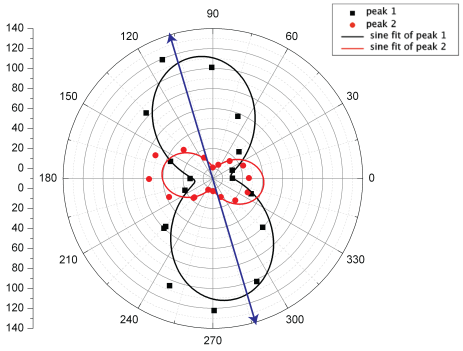

(e) NV88 (direction $\perp\rightarrow (b-d)$)

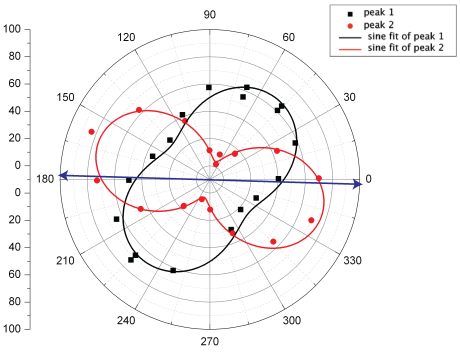

(f) NV93 (direction $\|\rightarrow (a-c)$)

Figure A.6: set #1, with NVs # 76, 82, 83, 85, 88, 93

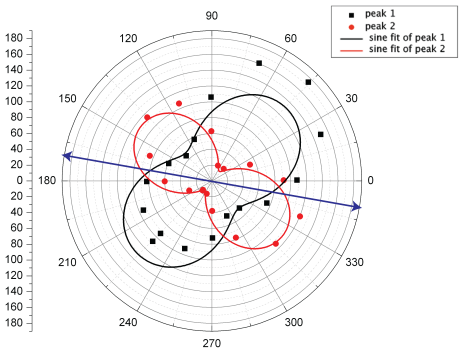

(a) NV95 (direction $\|\rightarrow (a-c)$)

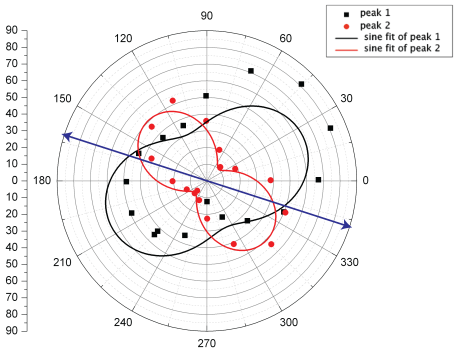

(b) NV96 (direction $\|\rightarrow (a-c)$)

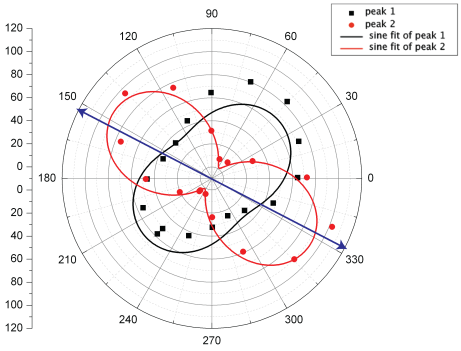

(c) NV98 (direction $\|\rightarrow (a-c)$)

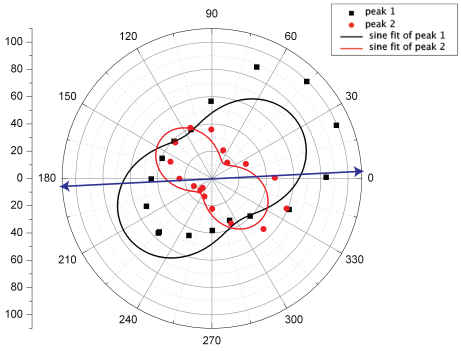

(d) NV99 (direction $\|\rightarrow (a-c)$)

Figure A.7: set #2, with NVs # 95, 96, 98, 99

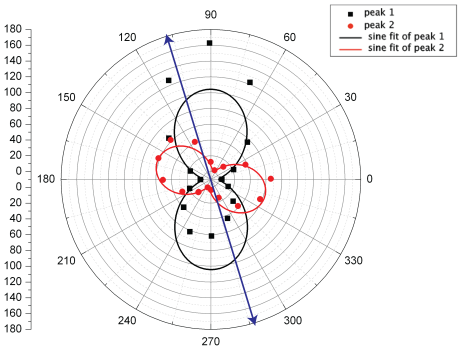

(a) NV100 (direction $\perp\rightarrow (b-d)$)

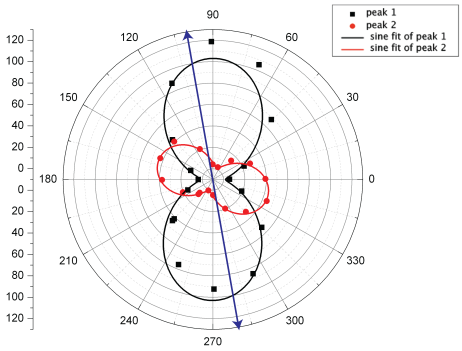

(b) NV101 (direction $\perp\rightarrow (b-d)$)

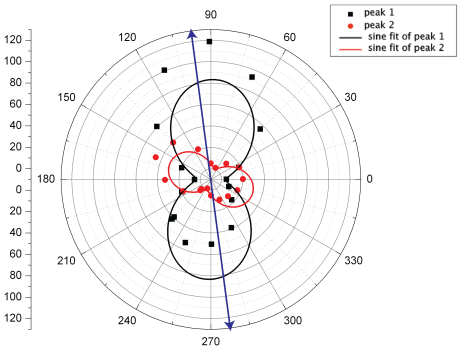

(c) NV103 (direction $\perp\rightarrow (b-d)$)

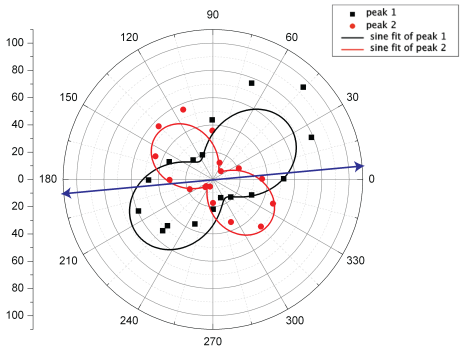

(d) NV104 (direction $\parallel\rightarrow (a-c)$)

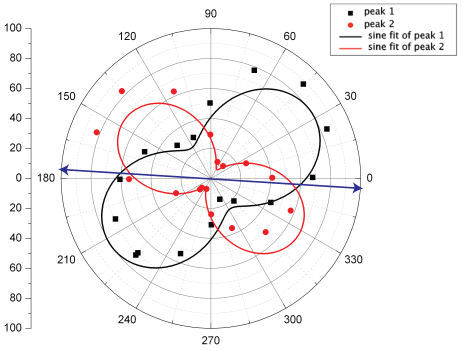

(e) NV107 (direction $\parallel\rightarrow (a-c)$)

Figure A.8: set #3, with NVs # 100, 101, 103, 104, 107

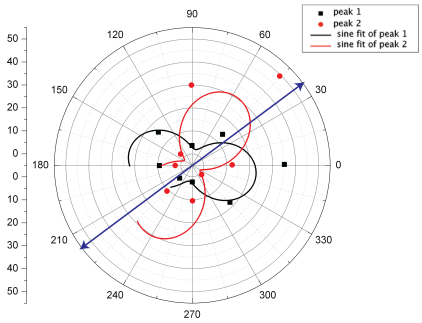

(a) NV105bis (direction $\|\rightarrow (a-c)$)

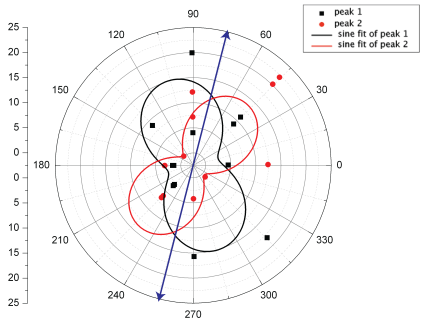

(b) NV106bis (direction $\perp\rightarrow (b-d)$)

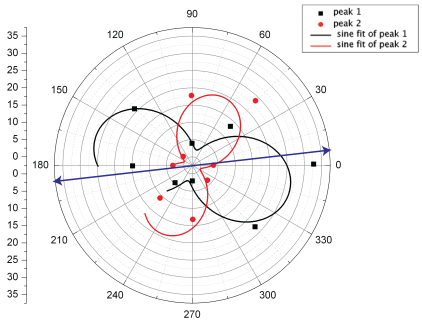

(c) NV107bis (direction $\|\rightarrow (a-c)$)

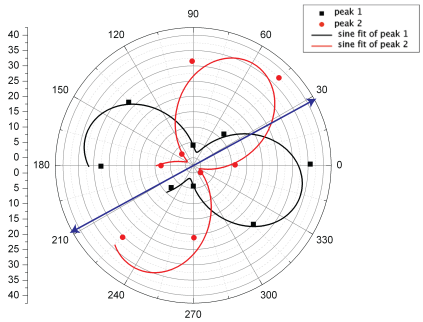

(d) NV108 (direction $\|\rightarrow (a-c)$)

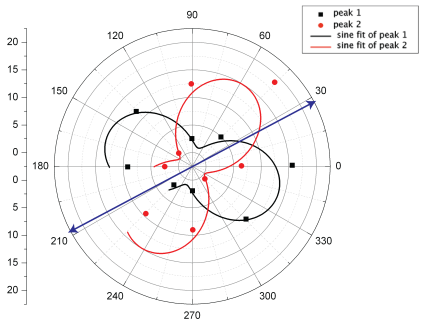

(e) NV109 (direction $\|\rightarrow (a-c)$)

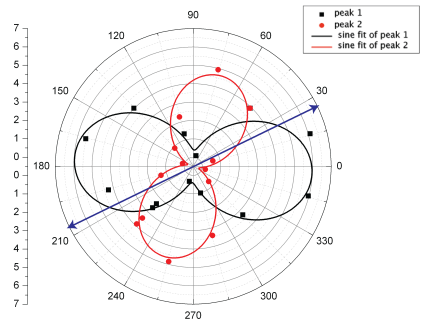

(f) NV110 (direction $\|\rightarrow (a-c)$)

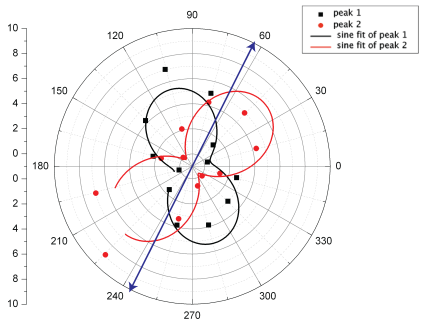

(g) NV111 (direction $\perp\rightarrow (b-d)$)

Figure A.9: set #4, with NVs # 105b, 106b, 107b, 108, 109, 110, 111

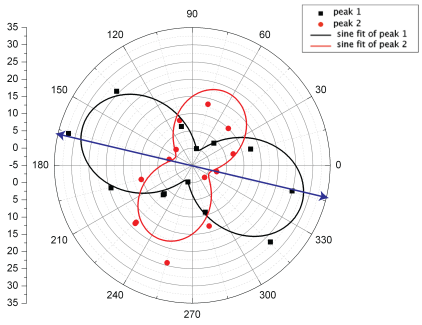

(a) NV112 (direction $\|\rightarrow (a-c)$)

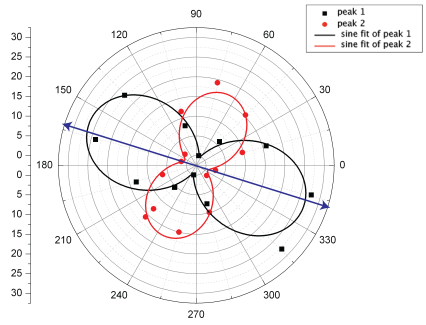

(b) NV113 (direction $\|\rightarrow (a-c)$)

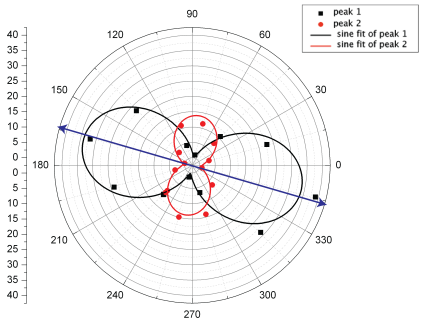

(c) NV114 (direction $\|\rightarrow (a-c)$)

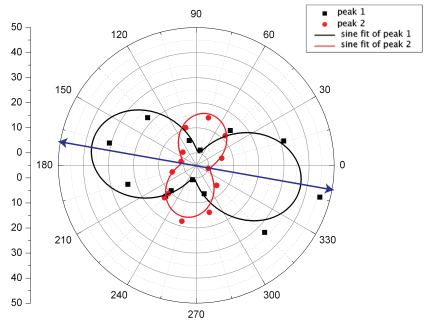

(d) NV115 (direction $\|\rightarrow (a-c)$)

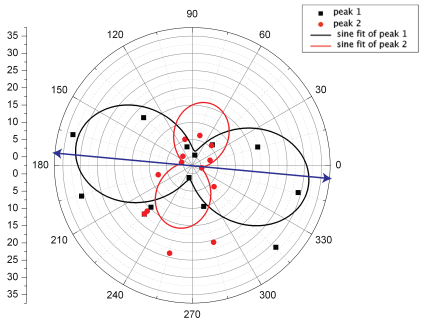

(e) NV116 (direction $\|\rightarrow (a-c)$)

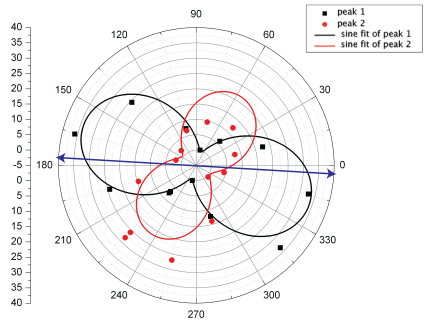

(f) NV117 (direction $\|\rightarrow (a-c)$)

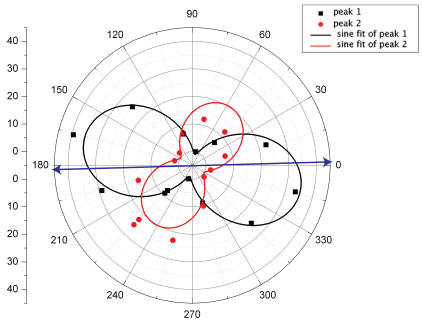

(g) NV118 (direction $\|\rightarrow (a-c)$)

Figure A.10: set #5, with NVs # 112, 113, 114, 115, 116, 117, 118

A.2.1 Summary plots

In this section we report a collective plot, for each group of NVs belonging to the same region, where we show the direction of the total emission maximal intensity. As we will show in the following section 4.6.4, this direction is almost aligned with the (perpendicular) direction of the projection on the NV axis on the observation plane, and so it gives information about the defect's alignment. In the following plots the angles are referred to the samples' edge direction. We can notice a nice alignement of the total intensity direction either parallel or perpendicular to the sample's edge. We can see that not in all the groups there are both the two possible directions, and this will be an important detail, relevant for the following data analysis.

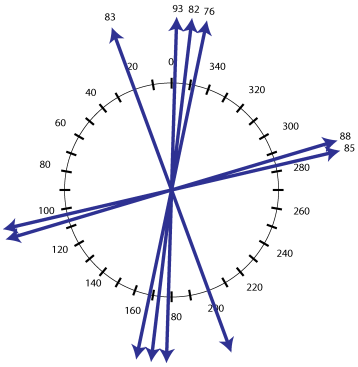

(a) plot of set #1, with NVs 76, 82, 83, 85, 88 and 93

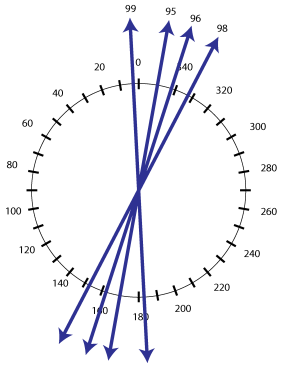

(b) plot of set #2, with NVs 95, 96, 98 and 99

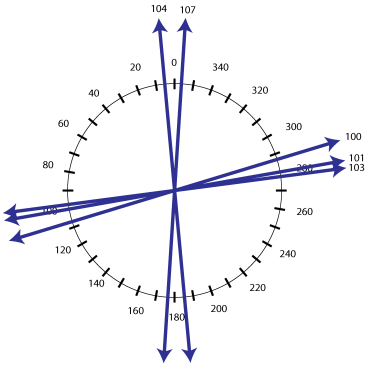

(c) plot of set #3, with NVs 100, 101, 103, 104 and 107

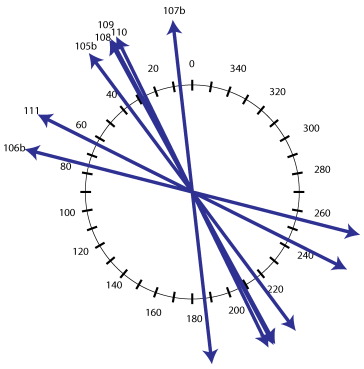

(d) plot of set #4, with NVs 105b, 106b, 107b, 108, 109, 110 and 111

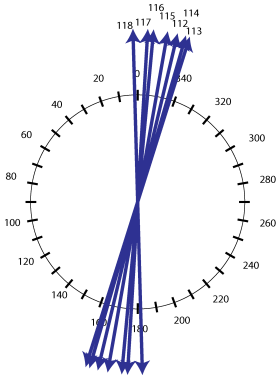

(e) plot of set #5, with NVs 112, 113, 114, 115, 116, 117 and 118

Figure A.11: plots of the total emission polarization directions, grouped following the spatial grouping of the NVs

Appendix B

Details on calculations

B.1 Calculations on the projection of the ${}^3E_x$ and ${}^3E_y$ orbitals axes on the observation plane

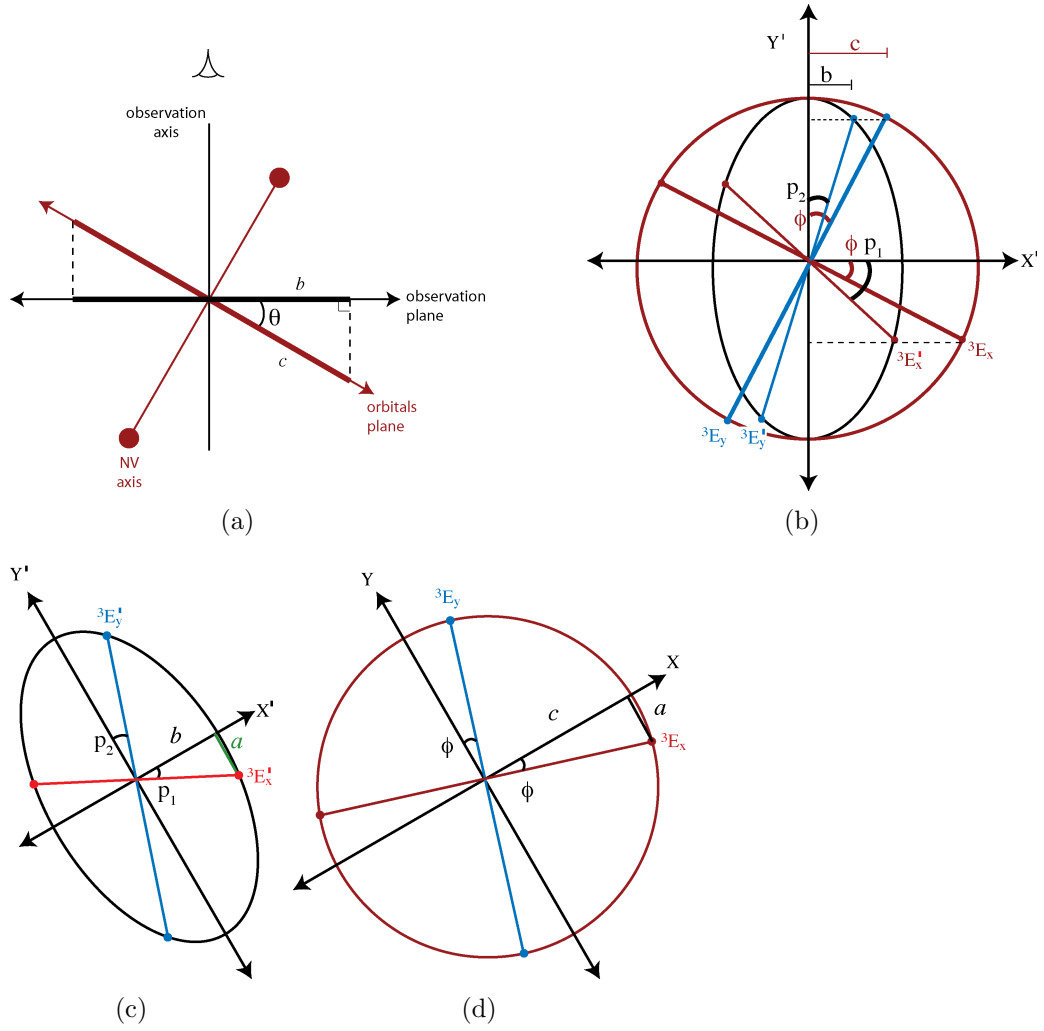

Figure B.1: (a) a sketch of the orbitals plane and the observation plane projected on the (X', Z') plane, i.e observed along Y'. (b) a sketch of the orbitals plane, as seen along the NV axis, and the orbitals ellipse, i.e. the projection of the orbitals plane on the observation plane. (c) The orbitals ellipse alone. (d) The orbitals plane as seen along the NV axis.

In the following we will refer to the vectors described in figure B.1, copied at the beginning of this appendix in figure B.1(d) for reader's convenience.

The angle ϕ is the angle by which the orbitals directions X and Y have to rotate in the orbitals plane in order to coincide to Y' and the projection of X' on the orbitals plane respectively. The angle p_1 is the projection of ϕ on the observation plane. To calculate their relationship we note that $\tan\phi = \frac{a}{c}$, $\tan p_1 = \frac{a}{b}$ (cfr. B.1(b)) and $c = b\sin\theta$ (cfr. B.1(a))

B.2 Addition of sinusoidal funcions

To estimate of the *total intensity emitted from both the orbitals*, we want to calculate the sum of the two sinusoidal fitting functions.

If we have

$$\begin{cases} f_1 = y_{01} + A_1 \sin\left[\frac{2\pi}{w}(x - x_{01})\right] \\ f_2 = y_{02} + A_2 \sin\left[\frac{2\pi}{w}(x - x_{02})\right] \end{cases}$$

$$\begin{cases} f_1 = y_{01} + A_1 \sin\left(\frac{2\pi}{w}x + \varphi_1\right) \\ f_2 = y_{02} + A_2 \sin\left(\frac{2\pi}{w}x + \varphi_2\right) \end{cases}$$

where we have set

$$\varphi_1 \equiv -\frac{2\pi x_{01}}{w} \tag{B.1}$$

$$\varphi_2 \equiv -\frac{2\pi x_{02}}{w} \tag{B.2}$$

as the two fitting functions, with $w = 180$ as period for both. Then we can write:

$$\begin{aligned}
f_{tot} &= f_1 + f_2 \\
&= y_{01} + y_{02} + A_1 \sin\left(\frac{2\pi}{w}x + \varphi_1\right) + A_2 \sin\left(\frac{2\pi}{w}x + \varphi_2\right) \\
&= y_{01} + y_{02} + \\
&\quad + A_1\left[\sin\left(\frac{2\pi}{w}x\right)\cos\varphi_1 + \cos\left(\frac{2\pi}{w}x\right)\sin\varphi_1\right] + \\
&\quad + A_2\left[\sin\left(\frac{2\pi}{w}x\right)\cos\varphi_2 + \cos\left(\frac{2\pi}{w}x\right)\sin\varphi_2\right] \\
&= y_{01} + y_{02} + \\
&\quad + A_1 \sin\left(\frac{2\pi}{w}x\right)\cos\varphi_1 + A_1 \cos\left(\frac{2\pi}{w}x\right)\sin\varphi_1 + \\
&\quad + A_2 \sin\left(\frac{2\pi}{w}x\right)\cos\varphi_2 + A_2 \cos\left(\frac{2\pi}{w}x\right)\sin\varphi_2 \\
&= y_{01} + y_{02} + \\
&\quad + \left[A_1\cos\varphi_1 + A_2\cos\varphi_2\right]\sin\left(\frac{2\pi}{w}x\right) + \\
&\quad + \left[A_1\sin\varphi_1 + A_2\sin\varphi_2\right]\cos\left(\frac{2\pi}{w}x\right)
\end{aligned}$$

where we have used the trigonometric addition identity

$$\sin(\alpha+\beta) = \sin\alpha\cos\beta + \sin\beta\cos\alpha. \tag{B.3}$$

Now we introduce three new quantities y_0,A and φ such that

$$A\cos\varphi \equiv A_1\cos\varphi_1 + A_2\cos\varphi_2 \tag{B.4}$$

$$A\sin\varphi \equiv A_1\sin\varphi_1 + A_2\sin\varphi_2 \tag{B.5}$$

$$y_0 \equiv y_{01} + y_{02} \tag{B.6}$$

$$\begin{aligned} f_{tot} &= y_0 + A\cos\varphi\sin\left(\frac{2\pi}{w}x\right) + A\sin\varphi\cos\left(\frac{2\pi}{w}x\right) \\ &= y_0 + A\sin\left(\frac{2\pi}{w}x + \varphi\right) \end{aligned} \tag{B.7}$$

where we have again applied the addition relations B.3.

To express A and φ in terms of the parameters of the single functions A_i and φ_i we first square and add B.4 and B.5:

$$
\begin{aligned}
A^2\cos^2\varphi + A^2\sin^2\varphi &= (A_1\cos\varphi_1 + A_2\cos\varphi_2)^2 + (A_1\sin\varphi_1 + A_2\sin\varphi_2)^2 \\
A^2 &= A_1^2\cos^2\varphi_1 + 2A_1A_2\cos\varphi_1\cos\varphi_2 + A_2^2\cos^2\varphi_2 + \\
&\quad + A_1^2\sin^2\varphi_1 + 2A_1A_2\sin\varphi_1\sin\varphi_2 + A_2^2\sin^2\varphi_2 \\
&= A_1^2 + A_2^2 + 2A_1A_2\cos\varphi_1\cos\varphi_2 + 2A_1A_2\sin\varphi_1\sin\varphi_2 \\
&= A_1^2 + A_2^2 + 2A_1A_2(\cos\varphi_1\cos\varphi_2 + \sin\varphi_1\sin\varphi_2) \\
&= A_1^2 + A_2^2 + 2A_1A_2\cos(\varphi_1 - \varphi_2)
\end{aligned}
$$

where we have used the other trigonometric addition identity:

$$\cos(\alpha - \beta) = \cos\alpha\cos\beta + \sin\alpha\sin\beta. \tag{B.8}$$

Then we divide B.5 by B.4:

$$
\begin{aligned}
\frac{A\sin\varphi}{A\cos\varphi} &= \frac{A_1\sin\varphi_1 + A_2\sin\varphi_2}{A_1\cos\varphi_1 + A_2\cos\varphi_2} \\
\tan\varphi &= \frac{A_1\sin\varphi_1 + A_2\sin\varphi_2}{A_1\cos\varphi_1 + A_2\cos\varphi_2}.
\end{aligned}
$$

Summarizing, the sum of the two sinusoidal fitting function $f_{tot} = f_1 + f_2$

is :

$$f_{tot} = y_0 + A \sin\left(\frac{2\pi}{w}x + \varphi\right) \tag{B.9}$$

where

$$\varphi_i = -\frac{2\pi\, x_{0i}}{w} \tag{B.10}$$

$$y_0 = y_{01} + y_{02} \tag{B.11}$$

$$A = \sqrt{A_1^2 + A_2^2 + 2A_1A_2\cos(\varphi_1 - \varphi_2)} \tag{B.12}$$

$$\varphi = \arctan\left[\frac{A_1\sin\varphi_1 + A_2\sin\varphi_2}{A_1\cos\varphi_1 + A_2\cos\varphi_2}\right] \tag{B.13}$$

$$x_{0tot} = -\frac{\varphi\, w}{2\pi}. \tag{B.14}$$

Attention must be paid in applying formulae B.10, B.13 and B.14 when the values of x_{01} and x_{02} are negative or less than 90°.

Bibliography

[AvK85] C A J Ammerlaan and R van Kemp. Magnetic resonance spectroscopy in semiconducting diamond. *Journal of Physics C: Solid State Physics*, 18(13):2623, 1985.

[BAC+10] F. Bonfigli, S. Almaviva, A. Cedola, I. Franzini, S. Lagomarsino, D. Pelliccia, and R.M. Montereali. Visible emitting color centers in lithium fluoride for x-ray imaging applications. *Radiation Measurements*, 45(3-6):599 – 601, 2010. Proceedings of the 7th European Conference on Luminescent Detectors and Transformers of Ionizing Radiation (LUMDETR 2009).

[BB84] Charles H. Bennett and G. Brassard. Quantum cryptography: Public key distribution and coin tossing. In *Proceedings of the IEEE International Conference on Computers, Systems, and Signal Processing, Bangalore*, page 175, Bangalore, 1984. IEEE International Conference on Computers, Systems, and Signal Processing.

[BBB+92] Charles H. Bennett, François Bessette, Gilles Brassard, Louis Salvail, and John Smolin. Experimental quantum cryptography. *Journal of Cryptology*, 5:3–28, 1992.

[BBC+09] R S Balmer, J R Brandon, S L Clewes, H K Dhillon, J M Dodson, I Friel, P N Inglis, T D Madgwick, M L Markham, T P Mollart, N Perkins, G A Scarsbrook, D J Twitchen, A J Whitehead, J J Wilman, and S M Woollard. Chemical vapour deposition synthetic diamond: materials, technology and applications. *Journal of Physics: Condensed Matter*, 21(36):364221, 2009.

[BD06] T. P. Bodiya and L.-M. Duan. Scalable generation of graph-state entanglement through realistic linear optics. *Physical Review Letters*, 97(14):143601, Oct 2006.

[Ben62] W. R. Bennett. Hole burning effects in a he-ne optical maser. *Physical Review*, 126(2):580–593, Apr 1962.

[Ber98] B. Berzina. Formation of self-trapped excitons through stimulated recombination of radiation-induced primary defects in alkali halides. *Journal of Luminescence*, 76-77:389 – 391, 1998. Proceedings of the Eleventh International Conference on Dynamical Processes in Excited States of Solids.

[BI51] B. Bleaney and D. J. E. Ingram. Paramagnetic resonance and hyperfine structure in four cobalt salts. *Proceedings of the Royal Society of London. Series A, Mathematical and Physical Sciences*, 208(1093):pp. 143–158, 1951.

[BIS+09] P. Baranov, I. Il'in, A. Soltamova, A. Vul', S. Kidalov, F. Shakhov, G. Mamin, S. Orlinskii, and M. Salakhov. Electron spin resonance detection and identification of nitrogen centers in nanodiamonds. *JETP Letters*, 89:409–413, 2009.

[BK05] SD Barrett and P Kok. Efficient high-fidelity quantum computation using matter qubits and linear optics. *Physical Review A*, 71(6), June 2005.

[BKB+02] A. Beveratos, S. Kühn, R. Brouri, T. Gacoin, J.-P. Poizat, and P. Grangier. Room temperature stable single-photon source. *The European Physical Journal D - Atomic, Molecular, Optical and Plasma Physics*, 18:191–196, 2002. 10.1140/epjd/e20020023.

[Ble51] B. Bleaney. Hyperfine structure in paramagnetic resonance. *Physica*, 17(3-4):175 – 190, 1951.

[BLMS00] Gilles Brassard, Norbert Lütkenhaus, Tal Mor, and Barry C. Sanders. Limitations on practical quantum cryptography. *Physical Review Letters*, 85(6):1330–1333, Aug 2000.

[BN95] J. Baker and M. Newton. Nitrogen in diamond studied by magnetic resonance. *Applied Magnetic Resonance*, 8:207–228, 1995. 10.1007/BF03162787.

[BN09] B. R. Boruah and M. A. A. Neil. Laser scanning confocal microscope with programmable amplitude, phase, and polarization of the illumination beam. *Review of Scientific Instruments*, 80:013705, 2009.

[BNT+09] Gopalakrishnan Balasubramanian, Philipp Neumann, Daniel Twitchen, Matthew Markham, Roman Kolesov, Norikazu Mizuochi, Junichi Isoya, Jocelyn Achard, Johannes Beck, Julia Tissler, Vincent Jacques, Philip R. Hemmer, Fedor Jelezko, and Jorg Wrachtrup. Ultralong spin coherence time in isotopically engineered diamond. *Nature Matererials*, 8(5):383–387, 05 2009.

[BR01] Hans J. Briegel and Robert Raussendorf. Persistent entanglement in arrays of interacting particles. *Physical Review Letters*, 86(5):910–913, Jan 2001.

[BZG+08] A. Batalov, C. Zierl, T. Gaebel, P. Neumann, I.-Y. Chan, G. Balasubramanian, P. R. Hemmer, F. Jelezko, and J. Wrachtrup. Temporal coherence of photons emitted by single nitrogen-vacancy defect centers in diamond using optical rabi-oscillations. *Physical Review Letters*, 100(7):077401, Feb 2008.

[CC78] C. Cremer and T. Cremer. Considerations on a laser-scanning-microscope with high resolution and depth of field. *Microscopica Acta*, 81(1):31—44, September 1978.

[CLK+00] D. Cory, R. Laflamme, E. Knill, L. Viola, T. Havel, N. Boulant, G. Boutis, E. Fortunato, S. Lloyd, R. Martinez, C. Negrevergne, M. Pravia, Y. Sharf, G. Teklemariam, Y. Weinstein, and W. Zurek. Nmr based quantum information processing: Achievements and prospects. *Fortschritte der Physik*, 48(9-11):875–907, 2000.

[CN71] C D Clark and C A Norris. Photoluminescence associated with the 1.673, 1.944 and 2.498 ev centres in diamond. *Journal of Physics C: Solid State Physics*, 4(14):2223–2229, 1971.

[Cou09] Thomas Coudreau. Recent experiments in quantum information with trapped ions. *Journal of Physics B: Atomic, Molecular and Optical Physics*, 42(15):154011, 2009.

[CTJ83] A T Collins, M F Thomaz, and M I B Jorge. Luminescence decay time of the 1.945 ev centre in type ib diamond. *Journal of Physics C: Solid State Physics*, 16(11):2177, 1983.

[Dav74] G Davies. Vibronic spectra in diamond. *Journal of Physics C: Solid State Physics*, 7(20):3797–3809, 1974.

[Dav81] G Davies. The jahn-teller effect and vibronic coupling at deep levels in diamond. *Reports on Progress in Physics*, 44(7):787, 1981.

[Dav94] G. Davies. Properties and growth of diamond. In *EMIS Data Review Series No. 9*. INSPEC, The Institution of Electrical Engineers, London, 1994.

[DdP65] H. B. Dyer and L. du Preez. Irradiation damage in type i diamond. *The Journal of Chemical Physics*, 42(6):1898–1906, 1965.

[Deu85] D Deutsch. Quantum-theory, the church-turing principle and the universal quantum computer. *Proceedings of the Royal Society of London Series A-Mathematical Physical and Engineering Sciences*, 400(1818):97–117, 1985.

[DFT+99] A. Dräbenstedt, L. Fleury, C. Tietz, F. Jelezko, S. Kilin, A. Nizovtzev, and J. Wrachtrup. Low-temperature microscopy and spectroscopy on single defect centers in diamond. *Physical Review B*, 60(16):11503–11508, Oct 1999.

[DH76] G. Davies and M. F. Hamer. Optical Studies of the 1.945 eV Vibronic Band in Diamond. *Proceedings of the Royal Society of London. A. Mathematical and Physical Sciences*, 348(1653):285–298, 1976.

[DiV95] David P. DiVincenzo. Quantum computation. *Science*, 270(5234):255–261, October 1995.

[DL92] G. Davies and S. C. Lawson. Vacancy-related centres in diamond. *Physical Review B*, 46(20):13157 – 13170, 1992.

[dP65] L du Preez. *PhD Thesis*. PhD thesis, University of the Witwatersrand, 1965.

[DTJ+99] A. Dräbenstedt, C. Tietz, F. Jelezko, J. Wrachtrup, S. Kilin, and A. Nizovtzev. Fluorescence correlation and low temperature linewidth of single defect centers in diamond. *Acta Physica Polonica A*, 96:664, 1999.

[FEN+09] S. Felton, A. M. Edmonds, M. E. Newton, P. M. Martineau, D. Fisher, D. J. Twitchen, and J. M. Baker. Hyperfine interaction in the ground state of the negatively charged nitrogen vacancy center in diamond. *Physical Review B*, 79(7):075203, Feb 2009.

[Fey82] RP Feynman. Simulating physics with computers. *International Journal of Theoretical Physics*, 21(6-7):467–488, 1982.

[Fuc02] Christopher A. Fuchs. Quantum mechanics as quantum information (and only a little more). arXiv:quant-ph/0205039v1, May 2002.

[GDT+97] A. Gruber, A. Drabenstedt, C. Tietz, L. Fleury, J. Wrachtrup, and C. von Borczyskowski. Scanning confocal optical microscopy and magnetic resonance on single defect centers. *Science*, 276(5321):2012–2014, 1997.

[GFK08] Adam Gali, Maria Fyta, and Efthimios Kaxiras. Ab initio supercell calculations on nitrogen-vacancy center in diamond: Electronic structure and hyperfine tensors. *Physical Review B*, 77(15):155206, Apr 2008.

[GHS92] Kenneth P. Ghiggino, Martin R. Harris, and Paul G. Spizzirri. Fluorescence lifetime measurements using a novel fiber-optic laser scanning confocal microscope. *Review of Scientific Instruments*, 63:2999, 1992.

[GJB+96] J. P. Goss, R. Jones, S. J. Breuer, P. R. Briddon, and S. Öberg. The twelve-line 1.682 ev luminescence center in diamond and the vacancy-silicon complex. *Phys. Rev. Lett.*, 77(14):3041–3044, Sep 1996.

[Gök94] Mathias Göken. Scanning tunneling microscopy in uhv with an x,y,z micropositioner. *Review of Scientific Instruments*, 65(7):2252–2254, 1994.

[Gro96] L.K. Grover. A fast quantum mechanical algorithm for database search. In *Proceedings, 28th Annual ACM Symposium on the Theory of Computing*, page 212, May 1996.

[GvO91] Max Glasbeek and Eric van Oort. Coherent transients of the n-v center in diamond. *Radiation Effects and Defects in Solids: Incorporating Plasma Science and Plasma Technology*, 119(1):301–306, 1991.

[HB80] Daniel C. Harris and Michael D. Bertolucci. *Symmetry and Spectroscopy: Introduction to Vibrational and Electronic Spectroscopy.* Oxford University Press, September 1980.

[HDWH08] Faruque M. Hossain, Marcus W. Doherty, Hugh F. Wilson, and Lloyd C. L. Hollenberg. Ab initio electronic and optical properties of the $n - v^-$ center in diamond. *Physical Review Letters*, 101(22):226403, Nov 2008.

[Her57] Herbert N. Hersh. Color centers in x-rayed potassium iodide. *Phys. Rev.*, 105(4):1158–1167, Feb 1957.

[HGA06] R. Hanson, O. Gywat, and D. D. Awschalom. Room-temperature manipulation and decoherence of a single spin in diamond. *Physical Review B*, 74(16):161203, Oct 2006.

[HHM84] R T Harley, M J Henderson, and R M Macfarlane. Persistent spectral hole burning of colour centres in diamond. *Journal of Physics C: Solid State Physics*, 17(8):L233, 1984.

[HHR+05] H. Haffner, W. Hansel, C. F. Roos, J. Benhelm, D. Chek-al kar, M. Chwalla, T. Korber, U. D. Rapol, M. Riebe, P. O. Schmidt, C. Becher, O. Guhne, W. Dur, and R. Blatt. Scalable multiparticle entanglement of trapped ions. *Nature*, 438(7068):643–646, 12 2005.

[Hir90] Masamitsu Hirai. Formation of color centers in anion-doped crystals. *Journal of Physics and Chemistry of Solids*, 51(7):737 – 745, 1990.

[HMEA06] R. Hanson, F. M. Mendoza, R. J. Epstein, and D. D. Awschalom. Polarization and readout of coupled single spins in diamond. *Physical Review Letters*, 97(8):087601, Aug 2006.

[HMF93a] Xing-Fei He, Neil B. Manson, and Peter T. H. Fisk. Paramagnetic resonance of photoexcited n-v defects in diamond. i. level anticrossing in the ^{3}a ground state. *Physical Review B*, 47(14):8809–8815, Apr 1993.

[HMF93b] Xing-Fei He, Neil B. Manson, and Peter T. H. Fisk. Paramagnetic resonance of photoexcited n-v defects in diamond. ii. hyperfine interaction with the ^{14}n nucleus. *Physical Review B*, 47(14):8816–8822, Apr 1993.

[HR67] A. E. Hughes and W. A. Runciman. Uniaxial stress splitting of doubly degenerate states of tetragonal and trigonal centres in cubic crystals. *Proceedings of the Physical Society*, 90(3):827, Mar 1967.

[HSK+08] Alexander Högele, Stefan Seidl, Martin Kroner, Khaled Karrai, Christian Schulhauser, Omar Sqalli, Jan Scrimgeour, and Richard J. Warburton. Fiber-based confocal microscope for cryogenic spectroscopy. *Review of Scientific Instruments*, 79(2):023709, 2008.

[HvBV+05] R. Hanson, L. H. Willems van Beveren, I. T. Vink, J. M. Elzerman, W. J. M. Naber, F. H. L. Koppens, L. P. Kouwenhoven, and L. M. K. Vandersypen. Single-shot readout of electron spin states in a quantum dot using spin-dependent tunnel rates. *Physical Review Letters*, 94(19):196802, May 2005.

[HWW+97] Scott A. Holmstrom, Changjiang Wei, Andrew S. M. Windsor, Neil B. Manson, John P. D. Martin, and Max Glasbeek. Spin echo at the rabi frequency in solids. *Physical Review Letters*, 78(2):302–305, Jan 1997.

[IKU+92] J. Isoya, H. Kanda, Y. Uchida, S. C. Lawson, S. Yamasaki, H. Itoh, and Y. Morita. Epr identification of the negatively charged vacancy in diamond. *Physical Review B*, 45(3):1436–1439, Jan 1992.

[JSLP93] H. Jia, J. Shinar, D. P. Lang, and M. Pruski. Nature of the native-defect esr and hydrogen-dangling-bond centers in thin diamond films. *Physical Review B*, 48(23):17595–17598, Dec 1993.

[JW04] F Jelezko and J Wrachtrup. Read-out of single spins by optical spectroscopy. *Journal of Physics: Condensed Matter*, 16(30):R1089–R1104, 2004.

[JW06] F. Jelezko and J. Wrachtrup. Single defect centres in diamond: A review. *physica status solidi (a)*, 203(13):1862–6319, 2006.

[Kan00] B. Kane. Silicon-based quantum computation. *Fortschritte der Physik*, 48(9-11):1023–1041, 2000.

[Kap64a] A. A. Kaplyanskii. Calculation of deformation splitting of spectral transitions in cubic crystals. *Optics and Spectroscopy*, 16:557, 1964.

[Kap64b] A. A. Kaplyanskii. Non cubic centres in cubic crystals and their piezospectroscopic investigation. *Optics and Spectroscopy*, 16:329, 1964.

[KFE+05] F. H. L. Koppens, J. A. Folk, J. M. Elzerman, R. Hanson, L. H. Willems van Beveren, I. T. Vink, H. P. Tranitz, W. Wegscheider, L. P. Kouwenhoven, and L. M. K. Vandersypen. Control and Detection of Singlet-Triplet Mixing in a Random Nuclear Field. *Science*, 309(5739):1346–1350, 2005.

[KH66] John D. Konitzer and Herbert N. Hersh. Color centers in x-rayed or ultraviolet-irradiated potassium iodide. *Journal of Physics and Chemistry of Solids*, 27(4):771 – 781, 1966.

[KLBS09] Avinash Kolli, Brendon W. Lovett, Simon C. Benjamin, and Thomas M. Stace. Measurement-based approach to entanglement generation in coupled quantum dots. *Physical Review B*, 79(3):035315, Jan 2009.

[KMZW00] Christian Kurtsiefer, Sonja Mayer, Patrick Zarda, and Harald Weinfurter. Stable solid-state source of single photons. *Physical Review Letters*, 85(2):290–293, Jul 2000.

[LBB+06] Yuan Liang Lim, Sean D. Barrett, Almut Beige, Pieter Kok, and Leong Chuan Kwek. Repeat-until-success quantum computing using stationary and flying qubits. *Physical Review A*, 73(1):012304, Jan 2006.

[LD08] J. A. Larsson and P. Delaney. Electronic structure of the nitrogen-vacancy center in diamond from first-principles theory. *Physical Review B*, 77(16):165201, Apr 2008.

[LO05] Brahim Lounis and Michel Orrit. Single-photon sources. *Reports on Progress in Physics*, 68(5):1129, 2005.

[LR96] A Lenef and SC Rand. Electronic structure of the n-v center in diamond: Theory. *Physical Review B*, 53(20):13441–13455, May 1996.

[LvW77] J HN Loubser and J A van Wyk. *Diamond Research*, 11:4, 1977.

[LvW78] J H N Loubser and J A van Wyk. Electron spin resonance in the study of diamond. *Reports on Progress in Physics*, 41(8):1201–1248, 1978.

[LWS+03] Xiaoqin Li, Yanwen Wu, Duncan Steel, D. Gammon, T. H. Stievater, D. S. Katzer, D. Park, C. Piermarocchi, and L. J. Sham. An All-Optical Quantum Gate in a Semiconductor Quantum Dot. *Science*, 301(5634):809–811, 2003.

[MGG+09] P M Martineau, M P Gaukroger, K B Guy, S C Lawson, D J Twitchen, I Friel, J O Hansen, G C Summerton, T P G Addison, and R Burns. High crystalline quality single crystal chemical vapour deposition diamond. *Journal of Physics: Condensed Matter*, 21(36):364205, 2009.

[MHS06] N. B. Manson, J. P. Harrison, and M. J. Sellars. Nitrogen-vacancy center in diamond: Model of the electronic structure and associated dynamics. *Physical Review B*, 74(10), Sep 2006.

[Min61] M. Minsky. Microscopy apparatus. US Patent 3013467 (A), 12 1961.

[MSLK05] Christine Meyer, Omar Sqalli, Heribert Lorenz, and Khaled Karrai. Slip-stick step-scanner for scanning probe microscopy. *Review of Scientific Instruments*, 76:063706, 2005.

[MWM96] Neil B. Manson, Changjiang Wei, and John P. D. Martin. Response of a two-level system driven by two strong fields. *Physical Review Letters*, 76(21):3943–3946, May 1996.

[NC00] M. A. Nielsen and I. L. Chuang. *Quantum Computation and Quantum Information*. Cambridge University Press, 2000.

[NKJ+09] P. Neumann, R. Kolesov, V. Jacques, J. Beck, J. Tisler, A. Batalov, L. Rogers, N. B. Manson, G. Balasubramanian, F. Jelezko, and J. Wrachtrup. Excited-state spectroscopy of single nv defects in diamond using optically detected magnetic resonance. *New Journal of Physics*, 11(1):013017, 2009.

[NKN+10] A. Nizovtsev, S. Kilin, P. Neumann, F. Jelezko, and J. Wrachtrup. Quantum registers based on single nv + $n^{13}c$ centers in diamond: Ii. spin characteristics of registers and spectra of optically detected magnetic resonance. *Optics and Spectroscopy*, 108:239–246, 2010. 10.1134/S0030400X1002013X.

[NPT99] Y. Nakamura, Yu. A. Pashkin, and J. S. Tsai. Coherent control of macroscopic quantum states in a single-cooper-pair box. *Nature*, 398(6730):786–788, 04 1999.

[OG90] Eric van Oort and Max Glasbeek. Electric-field-induced modulation of spin echoes of n-v centers in diamond. *Chemical Physics Letters*, 168(6):529 – 532, 1990.

[OPS96] A. Osvet, V. Palm, and I. Sildos. Spectral hole burning and uniaxial stress study of radiation-induced defects in diamond. *Journal of Applied Physics*, 79(11):8290–8293, 1996.

[PC04] D. Porras and J. I. Cirac. Bose-einstein condensation and strong-correlation behavior of phonons in ion traps. *Physical Review Letters*, 93(26):263602, Dec 2004.

[PDK10] Carlos A. Pérez-Delgado and Pieter Kok. What is a quantum computer, and how do we build one? arXiv-0906.4344, may 2010.

[Pen55] R. Penrose. A generalized inverse for matrices. *Mathematical Proceedings of the Cambridge Philosophical Society*, 51(03):406–413, 1955.

[PJT+05] J. R. Petta, A. C. Johnson, J. M. Taylor, E. A. Laird, A. Yacoby, M. D. Lukin, C. M. Marcus, M. P. Hanson, and A. C. Gossard. Coherent Manipulation of Coupled Electron Spins in Semiconductor Quantum Dots. *Science*, 309(5744):2180–2184, 2005.

[PM03] K. Pahlke and W. Mathis. Tolerant-gate implementation for the trapped-ion quantum-information processor. *Physical Review A*, 67(6):062305, Jun 2003.

[Poh87] D. W. Pohl. Dynamic piezoelectric translation devices. *Review of Scientific Instruments*, 58(1):54–57, 1987.

[PT56] R. Penrose and J. A. Todd. On best approximate solutions of linear matrix equations. *Mathematical Proceedings of the Cambridge Philosophical Society*, 52(01):17–19, 1956.

[RB01] Robert Raussendorf and Hans J. Briegel. A one-way quantum computer. *Physical Review Letters*, 86(22):5188–5191, May 2001.

[RBB03] Robert Raussendorf, Daniel E. Browne, and Hans J. Briegel. Measurement-based quantum computation on cluster states. *Physical Review A*, 68(2):022312, Aug 2003.

[RBSR91] D. A. Redman, S. Brown, R. H. Sands, and S. C. Rand. Spin dynamics and electronic states of n-v centers in diamond by epr and four-wave-mixing spectroscopy. *Physical Review Letters*, 67(24):3420–3423, Dec 1991.

[RLB94] S.C. Rand, A. Lenef, and S.W. Brown. Zeeman coherence and quantum beats in ultrafast photon echoes of n-v centers in diamond. *Journal of Luminescence*, 60-61:739 – 741, 1994. International Conference on Luminescence.

[RMK87] N. R. S. Reddy, N. B. Manson, and E. R. Krausz. Two-laser spectral hole burning in a colour centre in diamond. *Journal of Luminescence*, 38(1-6):46 – 47, 1987.

[RSLR92] D. Redman, Q. Shu, A. Lenef, and S. C. Rand. Two-beam coupling by nitrogen-vacancy centers in diamond. *Optics Letters*, 17(3):175–177, 1992.

[SBS98] D. Stevens, J. Brochard, and A. M. Steane. Simple experimental methods for trapped-ion quantum processors. *Physical Review A*, 58(4):2750–2759, Oct 1998.

[Sho94] P. W. Shor. Algorithms for quantum computation: Discrete logarithms and factoring. In IEEE Computer Society Press, editor, *Proceedings of the 35th Annual Symposium on Foundations of Computer Science*, pages 124–134, Los Alamitos, CA, 1994.

[SRX+10] Fazhan Shi, Xing Rong, Nanyang Xu, Ya Wang, Jie Wu, Bo Chong, Xinhua Peng, Juliane Kniepert, Rolf-Simon Schoenfeld, Wolfgang Harneit, Mang Feng, and Jiangfeng Du. Room-temperature implementation of the deutsch-jozsa algorithm with a single electronic spin in diamond. *Physical Review Letters*, 105(4):040504, Jul 2010.

[Ste97] A. Steane. The ion trap quantum information processor. *Applied Physics B: Lasers and Optics*, 64:623–643, 1997.

[TGR+06] Ph. Tamarat, T. Gaebel, J. R. Rabeau, M. Khan, A. D. Greentree, H. Wilson, L. C. L. Hollenberg, S. Prawer, P. Hemmer, F. Jelezko, and J. Wrachtrup. Stark shift control of single optical centers in diamond. *Physical Review Letters*, 97(8):083002, Aug 2006.

[TMH+08] Ph Tamarat, N B Manson, J P Harrison, R L McMurtrie, A Nizovtsev, C Santori, R G Beausoleil, P Neumann, T Gaebel, F Jelezko, P Hemmer, and J Wrachtrup. Spin-flip and spin-conserving optical transitions of the nitrogen-vacancy centre in diamond. *New Journal of Physics*, 10(4):045004 (9pp), 2008.

[vOG89] Eric van Oort and Max Glasbeek. Cross-relaxation dynamics of optically excited n-v centers in diamond. *Physical Review B*, 40(10):6509–6517, Oct 1989.

[vOMG88] E van Oort, N B Manson, and M Glasbeek. Optically detected spin coherence of the diamond n-v centre in its triplet ground state. *Journal of Physics C: Solid State Physics*, 21(23):4385, 1988.

[Wal79] J Walker. Optical absorption and luminescence in diamond. *Reports on Progress in Physics*, 42(10):1605, 1979.

[Wat65] G D Watkins. In P Baruch, editor, *Proc. 7th Int. Conf. on Physics of Semiconductors*, pages 97–, Paris: Dunod, 1965.

[WG59] E.P. Wigner and JJ Griffin. *Group theory and its application to the quantum mechanics of atomic spectra*. Academic Press, New York, 1959.

[WNB01] G. A. Watt, M. E. Newton, and J. M. Baker. Epr and optical imaging of the growth-sector dependence of radiation-damage defect production in synthetic diamond. *Diamond and Related Materials*, 10(9-10):1681 – 1683, 2001.

[WRP09] M. Wenin, R. Roloff, and W. Potz. Robust control of josephson charge qubits. *Journal of Applied Physics*, 105(8):084504, 2009.

[WWH+98] Andrew S. M. Windsor, Changjiang Wei, Scott A. Holmstrom, John P. D. Martin, and Neil B. Manson. Experimental studies of a strongly driven rabi transition. *Physical Review Letters*, 80(14):3045–3048, Apr 1998.

[ZAV46] E. ZAVOISKY. Paramagnetic absorption in some salts in perpendicular magnetic fields. *Zhurnal Eksperimentalnoi i Teoreticheskoi Fiziki*, 16(7):603–606, 1946.

[ZFF+04] Lianshui Zhang, Xiaomin Feng, Guangsheng Fu, Xiaowei Li, Li Han, Neil B. Manson, and Changjiang Wei. Coherent transient in dressed-state and transient spectra of autler-townes doublet. *Physical Review A*, 70(6):063404, Dec 2004.

[ZWG07] Jijun Zhao, J. M. Winey, and Y. M. Gupta. First-principles calculations of second- and third-order elastic constants for single crystals of arbitrary symmetry. *Physical Review B*, 75(9):094105, Mar 2007.